Modeling X-Y Beam Distributions via Crossing of Coupled Resonances in an Accelerator Complex

THIS IS A TEMPORARY TITLE PAGE
It will be replaced for the final print by a version
provided by the service academique.

Thèse n. 0000 2024
à présenter le 10 Octobre 2024
à la Faculté de Physique
LPAP
programme doctoral en Physique
École Polytechnique Fédérale de Lausanne

pour l'obtention du grade de Docteur ès Sciences
par

Elleanor Rose Lamb

Jury:

Prof Paolo De Los Rios, président du jury
Prof Mike Seidel, directeur de thèse
Dr Guido Sterbini, co-directeur de thèse
Dr Wolfram Fischer, rapporteur
Dr Frank Tecker, rapporteur
Prof Lesya Schutska, rapporteur

Lausanne, EPFL, 2024

Acknowledgements

The work in this these was made possible by the dedication of my supervisor, Guido Sterbini. I would like to thank him for all the time and ideas he has shared. I would like to thank those who have helped generously in this work, without whose expertise the results would not be present. Mike Seidel, Foteini Asvesta, Hannes Bartosik, Tirsi Prebibaj, Kostas Paraschou, Andrea Fornara, Witold Kozanecki, Giuliano Franchetti, Philippe Belanger, Joanna Wanczyk, Sofia Kostoglou, Tatiana Pieloni, Simon Albright, David Stickland, Ingrid Mases Sole, Elena de la Fuente Garcia, and the OP teams at PSB, PS, SPS and LHC. I would like to thank my reviewers Frank Tecker and Wolfram Fischer for their valuable input.
I would like to thank my amazing friends and family for their encouragement and support.

Abstract

(English/Français/Deutsch)

Key words: luminosity, van der Meer, non-factorization, resonance, calibration, losses
In high-energy colliders, discoveries are made possible by improving precision and accuracy of the measured rare events. Precision is maximized by increasing the collider integrated luminosity, whereas accuracy is addressed by minimizing the systematic errors via ad-hoc luminosity calibrations of the detectors.
This thesis contributes to improving the present understanding of the role and the impact of non-factorizable beam distributions on the aforementioned precision and accuracy reach. Starting from a theoretical approach, the concept of the non-factorizable distribution is introduced, originally showing that even Gaussian profiles of distributions matched to linear uncoupled lattices can be non-factorizable. Starting from this observation, the consequences of the losses in a synchrotron and the luminosity in a collider are developed and presented.
A measurement protocol to quantify the non-factorization is devised and, furthermore, it is demonstrated, numerically and experimentally, how non-factorization can be introduced in factorizable distributions via x-y coupling resonances in the presence of space charge. It is then shown experimentally that non-factorization can be transported along the full CERN accelerator chain, confirming that this is an inherent property of the beam distribution and not of the machine lattice.
This work directly contributes to the efforts devoted to improve the quality of the luminosity calibration in the HL-LHC era.

Zusammenfassung

Stichwörter: Leuchtkraft, van der Meer, Nicht-Faktorisierung, Resonanz, Kalibrierung, Verluste
Bei Hochenergiebeschleunigern werden Entdeckungen durch die Verbesserung der Präzision und Genauigkeit der gemessenen seltenen Ereignisse ermöglicht. Die Präzision wird durch die Erhöhung der integrierten Luminosität des Colliders maximiert, während die Genauigkeit durch die Minimierung der systematischen Fehler mittels Ad-hoc-Luminositätskalibrierungen der Detektoren angegangen wird.
Diese Arbeit trägt dazu bei, das derzeitige Verständnis der Rolle und des Einflusses nicht faktorisierbarer Strahlverteilungen auf die vorgenannten Präzisions- und Genauigkeitsziele zu verbessern. Ausgehend von einem theoretischen Ansatz wird das Konzept der nicht faktorisierbaren Verteilung erzeugt, wobei ursprünglich gezeigt wurde, dass sogar Gaußprofile von Verteilungen, die an lineare ungekoppelte Strahloptiken angepasst sind, nicht faktorisierbar sein können. Ausgehend von dieser Beobachtung werden die Konsequenzen für die Verluste in einem Synchrotron und die Luminosität in einem Collider entwickelt und dargestellt.
Es wird ein Messprotokoll zur Quantifizierung der Nicht-Faktorisierung entwickelt und darüber hinaus numerisch und experimentell demonstriert, wie Nicht-Faktorisierung in faktorisierbaren Verteilungen über x-y-Kopplungsresonanzen in Gegenwart von Raumladung eingeführt werden kann. Anschließend wird experimentell gezeigt, dass Nicht-Faktorisierung entlang der gesamten CERN-Beschleunigerkette transportiert werden kann, was bestätigt, dass dies eine inhärente Eigenschaft der Strahlverteilung und nicht des Maschinenoptik ist.
Diese Arbeit trägt direkt zu den Bemühungen bei, die Qualität der Luminositätskalibrierung in der HL-LHC-Ära zu verbessern.

Résumé

Mots clefs : luminosité, van der Meer, non-factorisation, résonance, étalonnage, pertes
Dans les collisionneurs de haute énergie, les découvertes sont rendues possibles par l'amélioration de la précision et de l'exactitude des événements rares mesurés. La précision est maximisée en augmentant la luminosité intégrée du collisionneur, tandis que l'exactitude est abordée en minimisant les erreurs systématiques via des calibrations ad-hoc de la luminosité des détecteurs.
Cette thèse contribue à améliorer la compréhension actuelle du rôle et de l'impact des distributions de faisceaux non factorisables sur la précision et l'exactitude susmentionnées. En partant d'une approche théorique, le concept de distribution non factorisable est introduit, montrant initialement que même les profils gaussiens de distributions apparié à des optiques linéaires non couplés peuvent être non factorisables. À partir de cette observation, les conséquences des pertes dans un synchrotron et de la luminosité dans un collisionneur sont développées et présentées.
Un protocole de mesure pour quantifier la non-factorisation est conçu et, de plus, il est démontré, numériquement et expérimentalement, comment la non-factorisation peut être introduite dans des distributions factorisables via des résonances de couplage x-y en présence d'une charge d'espace. Il est ensuite démontré expérimentalement que la non-factorisation peut être transportée tout au long de la chaîne d'accélérateurs du CERN, confirmant qu'il s'agit d'une propriété inhérente à la distribution du faisceau et non à l'optique de la machine.
Ce travail contribue directement aux efforts déployés pour améliorer la qualité de l'étalonnage de la luminosité à l'ère du HL-LHC.

Contents

List of Figures

List of Tables

1 Introduction

This thesis explores the performance of particle colliders, focusing on luminosity and precision measurement. It aims to provide new insights into modeling the dynamics of the machine, specifically concerning the properties of the beam distribution that are independent of the lattice structure. Namely, the non-factorization. Analytical models are developed alongside experimental and simulation evidence to demonstrate how the dynamics within the $x-y$ plane can evolve. The structure of the thesis is described briefly as the following.

Chapter 3 derives analytical equations for 4D transverse beam distributions based on observations of the beam profile in a single plane. The chapter explores the implications of free constraints, demonstrating how these constraints lead to a non-unique distribution. Non-factorizable distributions are introduced. It is shown how the property of non-factorization in beam distributions can impact the beam losses and luminosity. Additionally, a method is proposed for measuring the transverse beam distribution using collimation and profile measurements.

Chapter 4 illustrates how starting from a factorizable distribution, non-factorization can be introduced into the beam by periodically crossing coupled resonances in the Proton Synchrotron Booster in the presence of space charge.

Chapter 5 validates these findings through symplectic tracking simulations, employing single-particle tracking to understand the underlying dynamics and multi-particle tracking to benchmark the experimental results.

Chapter 6 provides experimental evidence showing that the non-factorization introduced in this manner is preserved throughout the accelerator chain. This preservation has important implications for precision luminosity measurements, particularly in the context of van der Meer scans, for which the largest uncertainty is the non-factorization of the transverse beam distribution.

2 Relevant contextual and theoretical concepts

The following chapter gives relevant concepts to guide the reader through the contributions in the thesis. It is a short summary, thus for more details on accelerator physics as a whole, see the very complete and valuable texts such as [1], [2].

2.1 The CERN accelerator complex

The research presented in this thesis is conducted within the framework of the European Organization for Nuclear Research's (CERN) proton accelerator complex. While the focus is on this specific facility, the findings are broadly applicable to proton synchrotrons and colliders worldwide.

CERN, located in Geneva, Switzerland, is home to some of the most significant physics experiments on the planet. This is made possible by its extensive accelerator complex, which accelerates protons to energies as high as 6.8 TeV.

The acceleration process begins at the LINAC4, a linear accelerator, and continues through the Proton Synchrotron Booster (PSB), the Proton Synchrotron (PS), and the Super Proton Synchrotron (SPS). Finally, the protons are injected into the Large Hadron Collider (LHC), where counter-rotating beams collide at interaction points (IP1-8). Four of the interaction points are the locations of high-energy physics experiments: CMS, LHCb, ATLAS, and ALICE, Fig. 2.1.

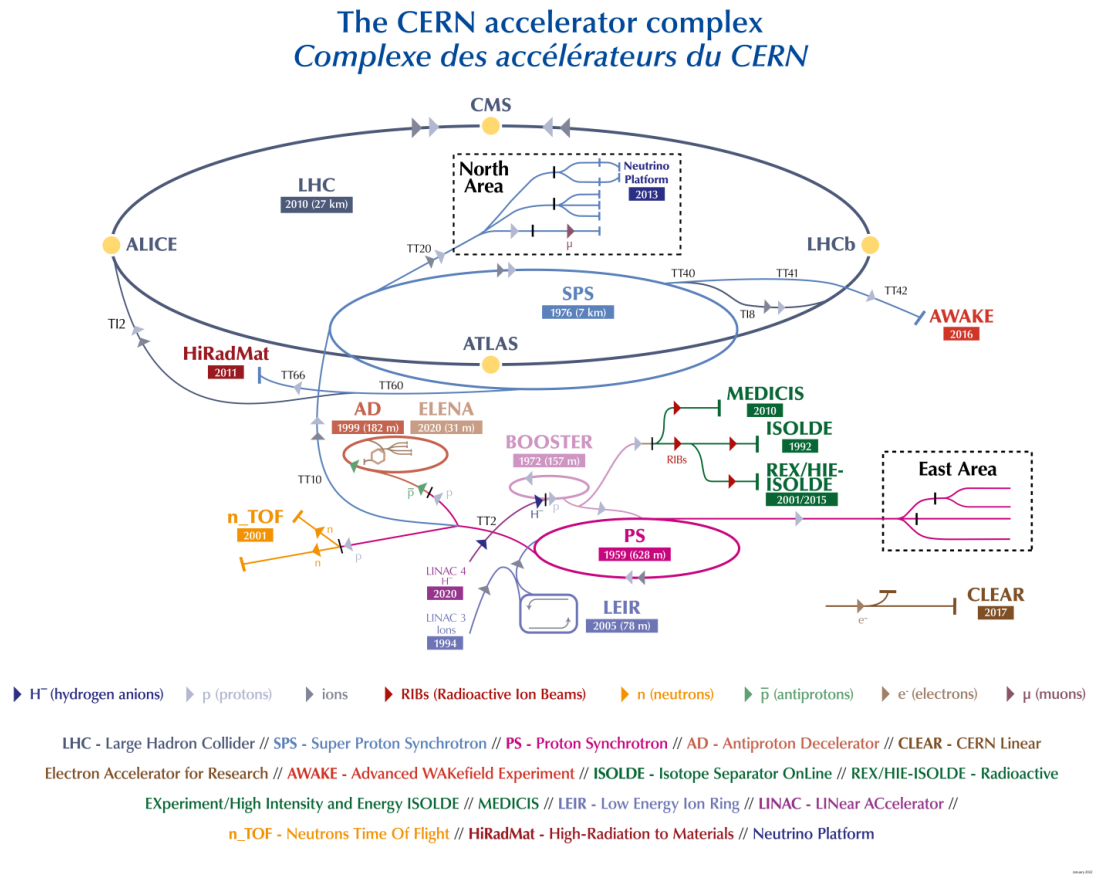

Figure 2.1: The CERN accelerator complex (not to scale). The path of the protons from the LINAC4 to the LHC is shown with grey arrows. The locations of the high energy physics experiments are shown on the LHC ring. Taken from [3].

2.2 Beam dynamics

Particle motion in an accelerator is governed by the electric and magnetic fields of the elements in the lattice, used to steer, accelerate and focus the beam [1]. The force on a particle is given by the Lorentz equation,

$$\overrightarrow{F} = \frac{d\overrightarrow{p}}{dt} = q\left(\overrightarrow{E} + \overrightarrow{v} \times \overrightarrow{B}\right). \tag{2.1}$$

$\overrightarrow{F}$ is the force on a particle, $\overrightarrow{p}$ is the particle momentum, $\overrightarrow{v}$ is the particle velocity, $\overrightarrow{E}$ is the electric field and $\overrightarrow{B}$ is the magnetic field. Multipole magnets control the 'optics' in a synchrotron. The multipole expansion solving Maxwell's equations is given by ($n = 1$ is a dipolar, $n = 2$ is a quadrupolar),

$$B_y + iB_x = \sum_{n=1}^{\infty} C^n (x + iy)^{n-1}. \tag{2.2}$$

It can be expressed in polar form,

$$B_\theta + iB_r = \sum_{n=1}^{\infty} C^n (r)^{n-1} e^{in\theta}. \tag{2.3}$$

The complex constant C_n can be expressed,

$$|C_n| e^{\varphi_n} \tag{2.4}$$

Note: A 'normal' multipole has a $\varphi_n = 0$ (phase), and a skew multipole is rotated by π/n, so a phase of π/n.

2.2.1 Coordinates

The choice of coordinate system which describes the motion is important in order to simplify the equations. The Frenet-Serret coordinate system is used. The transformation from the Cartesian coordinates (and canonical momenta) are given by [4],

$$X = (x+\rho)\cos\left(\frac{s}{\rho}\right) - \rho \tag{2.5}$$

$$Y = y \tag{2.6}$$

$$Z = (x+\rho)\sin\left(\frac{s}{\rho}\right) \tag{2.7}$$

$$p_x = P_X\cos\left(\frac{s}{\rho}\right) + P_Z\sin\left(\frac{s}{\rho}\right) \tag{2.8}$$

$$p_y = P_Y \tag{2.9}$$

$$p_s = P_Z\left(1+\frac{x}{\rho}\right)\cos\left(\frac{s}{\rho}\right) - P_X\left(1+\frac{x}{\rho}\right)\sin\left(\frac{s}{\rho}\right). \tag{2.10}$$

The dynamics under an approximation of transport from one position s_0, to s_1 in the ring can be described by symplectic maps (matrices in the linear case). This is a result of Liouville theorem, that closed (constant energy) systems are phase space density preserving [5]. A necessary condition for symplecticity of a matrix W is that,

$$W^T \Omega W = \Omega, \tag{2.11}$$

given that,

$$\Omega = \begin{bmatrix} 0 & I_n \\ -I_n & 0 \end{bmatrix}, \tag{2.12}$$

where I_n is the n dimensional identity matrix.

Linear dynamics is when the Hamiltonian of the system has terms up to quadratic order in the canonical momenta. For the linear case,

$$\begin{pmatrix} x \\ p_x \end{pmatrix}_{s_1} = \underbrace{M_N \circ M_{N-1} \circ \cdots \circ M_1}_{M(s_0,s_1)} \circ \begin{pmatrix} x \\ p_x \end{pmatrix}_{s_0}. \tag{2.13}$$

The linear transport matrix can be written in terms of the Courant-Snyder parameters,

$$\beta(s), \quad \alpha(s), \quad \gamma(s), \tag{2.14}$$

which are shown in relation to the physical phase space ellipse, Fig. 2.2.

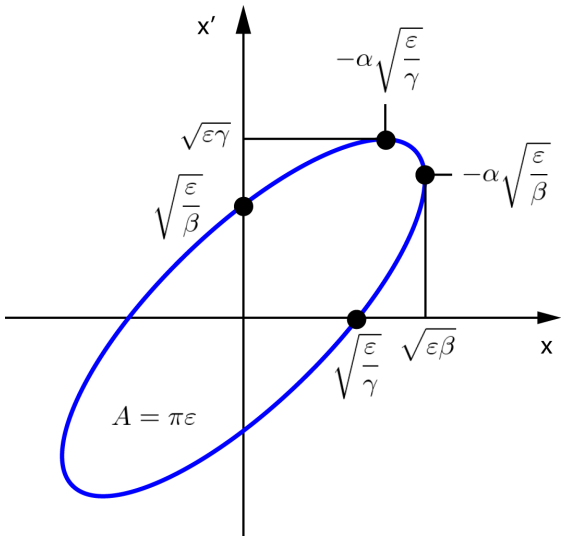

Figure 2.2: The phase space ellipse and Courant-Snyder parameters, taken from [6]

The transport matrix for one turn M_{OTM} can be given in terms of the Courant-Snyder parameters,

$$M_{OTM} = \begin{pmatrix} \cos(\mu_x) + \alpha_x \sin(\mu_x) & \beta_x \sin(\mu_x) \\ -\gamma_x \sin(\mu_x) & \cos(\mu_x) - \alpha_x \sin(\mu_x), \end{pmatrix} \tag{2.15}$$

where μ_x is the phase advance, $2\pi Q_x$ where Q_x is the tune. M_{OTM} can be composed into,

$$M_{OTM} = A^{-1} R A. \tag{2.16}$$

The normalisation matrix A transforms the coordinates, and the M_{OTM} into a pure rotation. A can be written in terms of the Courant-Snyder parameters,

$$A = \begin{pmatrix} \sqrt{\beta_x} & 0 \\ -\frac{\alpha_x}{\sqrt{\beta_x}} & \frac{1}{\sqrt{\beta_x}} \end{pmatrix}. \tag{2.17}$$

A direct consequence of the symplecticity is that there is a preserved constant, the emittance, given in the $x - p_x$ plane, ϵ_x,

$$\epsilon_x = \gamma_x(s) x(s)^2 + 2\alpha_x(s) x(s) p_x(s) + \beta_x(s) p_x(s)^2. \tag{2.18}$$

It relates to the area of the ellipse, in Fig. 2.2 by,

$$\text{Area} = 2\pi\epsilon_x. \tag{2.19}$$

The transformation matrix transforms the physical coordinates to the normalised coordinates, given in one plane,

$$\begin{pmatrix} \hat{x} \\ \hat{p}_x \end{pmatrix} = A^{-1} \cdot \begin{pmatrix} x \\ p_x \end{pmatrix}. \tag{2.20}$$

The normalisation via the generalised matrix for linear coupling, A, $(2n \times 2n)$, where n is the planes of motion, to a pure rotation R, is the equivalent to a transformation of coordinates to action-angle variables. The following is taken from Wolski, [1] and Goldstein [7].

Relating a vector of the action $\overrightarrow{J}$, to the physical coordinates and their normal form, and following the derivation in [1],

$$\overrightarrow{J} = \begin{pmatrix} \hat{x}_1 \\ \hat{p}_1 \\ \vdots \\ \hat{x_n} \\ \hat{p_n} \end{pmatrix} = A^{-1}\overrightarrow{x}.$$

The new action-angle variables are defined,

$$J_k = \frac{1}{2}\left(\hat{x}_k^2 + \hat{p}_k^2\right),$$

$$\tan\phi_k = -\frac{\hat{p}_k}{\hat{x}_k}.$$

The Hamiltonian in one dimension is,

$$\hat{H}_k = Q_k J_k, \tag{2.21}$$

where Q_k is the tune and J_k the action. The evolution of the system with respect to the new action-angle variables is given by Hamilton's equations,

$$\dot{q}_i = \frac{\partial H}{\partial p_i}, \tag{2.22}$$

$$\dot{p}_i = -\frac{\partial H}{\partial q_i}, \tag{2.23}$$

and so,

$$\frac{\partial \phi_k}{\partial t} = \frac{\partial \hat{H}_k}{\partial J_k} = Q_k, \tag{2.24}$$

$$\frac{\partial J_k}{\partial t} = -\frac{\partial \hat{H}_k}{\partial \phi_k} = 0. \tag{2.25}$$

This means that the evolution in time of ϕ_k proceeds with the tune, while J_k remains constant [7], thus a rotation of the system results in,

$$J_k \mapsto J_k,$$

$$\phi_k \mapsto \phi_k + \mu_k,$$

where μ_k is the phase advance. The motion in any degree of freedom, k, is independent to the other degrees of freedom, even for the case of non-zero linear coupling. An example of the normalisation and the evolution of motion in the physical and normalised coordinates is shown in 2.3.
We can define the action in terms of the physical coordinates and the Courant-Snyder parameters, which is conserved, given in the x plane,

$$2J_x = \gamma_x x^2 + 2\alpha_x x p_x + \beta_x p_x^2. \tag{2.26}$$

Thus, related to the single particle emittance,

$$2J_x = \epsilon_x. \tag{2.27}$$

The Hamiltonian for nonlinear beam dynamics can be expressed in terms of action-angle variables via a normal form. This holds true only in certain circumstances, for example, in the KAM (Kolmogorov-Arnold-Moser theory [8]–[10]) region [4]. Unlike the linear case, the tune (rate of rotation of the angle) depends on the action. However, the transformation allows the surface of Poincaré sections to be a pure rotation.

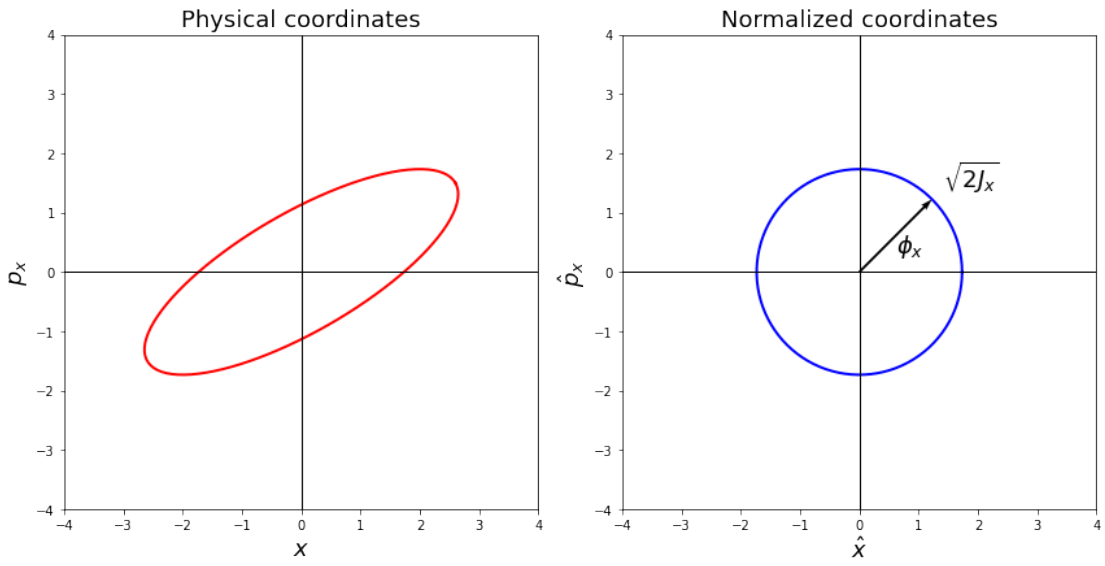

Figure 2.3: Physical to (linearly) normalised coordinates. The motion is a pure rotation.

2.2.2 Beam Distribution in a Linear machine

For a 6D particle ensemble, the Σ matrix of the second order moments can be defined (in the physical coordinates).

For the beam to be 'matched', or stationary, the Σ matrix must be unchanged through one periodic cell, that is [1],

$$M_{\mathrm{OTM}} \Sigma M_{\mathrm{OTM}}^{T} = \Sigma. \tag{2.28}$$

It can be shown the second order moments of the distribution in the normalised coordinates is a diagonal matrix (the covariance of cross terms is 0 due to symmetry of a circle in phase space). The A matrix in 6D transforms to uncoupled dynamics (if the coupling is linear).

The eigenvalues of $\Sigma\Omega$ give the statistical emittances [1],

$$\mathrm{eigenvalues}(\Sigma\Omega) = \pm i\epsilon_k. \tag{2.29}$$

2.2.3 Resonances

Higher order multipoles are common in modern accelerators. In general, solutions to the equations of motion are not in closed form. Therefore, approximations to the motion are used to describe the dynamics (e.g. perturbation theory). For a complete explanation of the relevant theory, see [1], [2]. The given resonances (n_x, n_y coefficients) that are driven by a particular element can be calculated from the Hamiltonian [11] via Resonance Driving Terms (RDTs). A skew and normal multipole will drive different resonances.

The resonance condition, defined for the single particle tune Q_x, Q_y, with the integer coefficients n_x, n_y, is given by

$$n_x Q_x + n_y Q_y = C, \tag{2.30}$$

where C is also an integer. Due to the set tunes, the particle receives a kick that adds coherently [1]. The source of the kick can be a magnet imperfection, or from a potential that is induced by the beam itself (e.g. space charge, beam-beam interactions).

The order of a resonance is given by,

$$|n_x| + |n_y|. \tag{2.31}$$

The set-tune, any amplitude dependence of the tune, and the interaction with resonances

can be visualised in terms of a resonance diagram, which can be plotted up to any resonance order, Fig. 2.4.

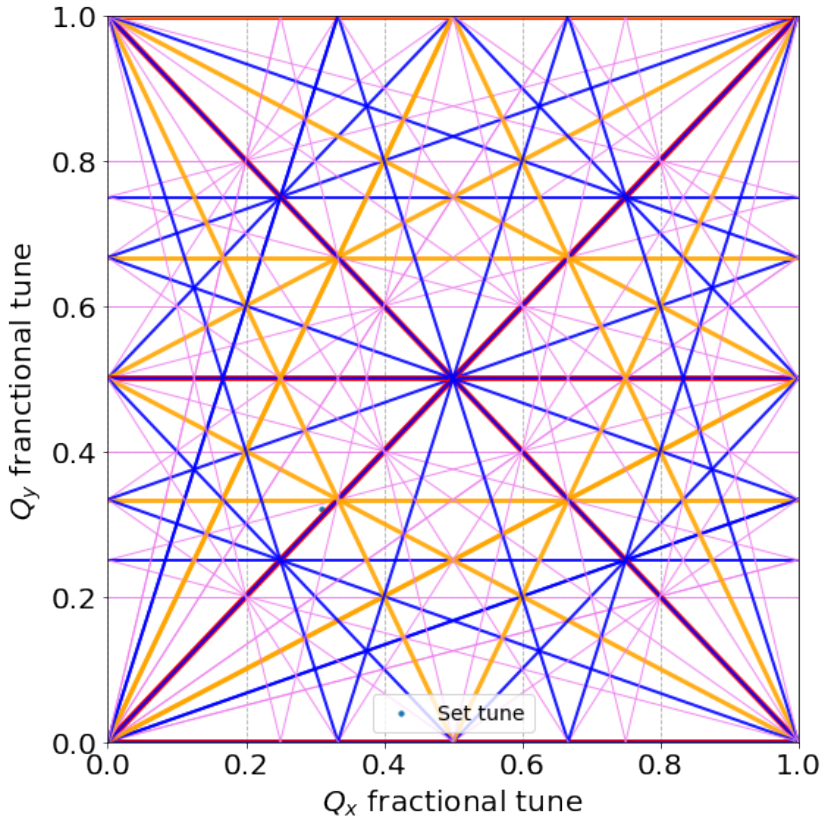

Figure 2.4: Resonance diagram plotted up to 5th order. The lower order resonances are thicker lines. An example working point (set tune) is shown.

2.2.4 Space Charge

Charged particles act on each other with their self-fields, 'space charge'. Space charge is most prominent in low energy, high-brightness (small emittance and high intensity) machines [12]. This nonlinear field results in amplitude dependent detuning, (negative defocusing), from the set tune. The maximum detuning is given by equation 2.32, [12], in the approximation of a transverse bi-Gaussian distribution.

$$\delta Q_{x,y}^{SC} = -\frac{r_0 \lambda}{2\pi e \beta_r^2 \gamma_r^3} \oint \frac{\beta_{x,y}}{\sigma_{x,y}(s)\left[\sigma_x(s) + \sigma_y(s)\right]}, \tag{2.32}$$

r_0 denotes the classical proton radius, while λ represents the longitudinal charge density. The elementary charge is symbolized by e. The relativistic parameters are indicated by β_r and γ_r. The optics beta function represented by β_y, and the beam sizes in the horizontal and vertical planes are given by $\sigma_{x,y}$.

The amplitude dependent detuning looks like a 'tune spread' in the Q_x, Q_y plane, shown in Fig. 2.5. The tune spread, larger at low energies, leads to the distribution being more susceptible to resonances. In the case of bunched beams, the position in longitudinal phase space affects the tune-spread, as the line density changes the space charge force. This causes the tune-spread to evolve periodically with the longitudinal motion. If the longitudinal distribution is sliced, the maximum extent of the tune spread will differ for each slice.

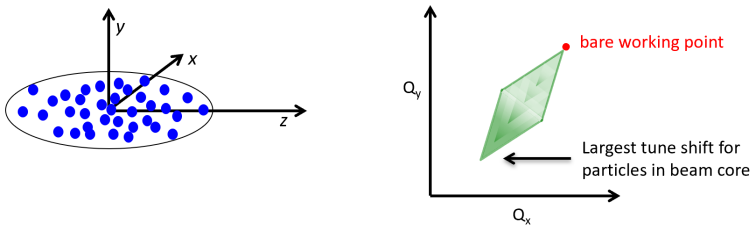

Figure 2.5: Tune spread from space charge is amplitude dependent in the distribution [13].

The driving terms from the space charge potential can also excite resonances. These are difficult to compensate for, as opposed to resonances driven by machine imperfections. The resonances driven can be calculated with perturbation theory [14], [15].

2.2.5 Resonances in Two-Dimensions

The dynamics near one dimensional (only one of n_x, n_y is non-zero) resonances are well described and studied, some examples are given by [16], [17]. The dynamics can be seen through surfaces of Poincaré section [18]. Since the motion is nonlinear, and the linear action-angle variables no longer hold, the phase space will not be circular and may contain fixed

points, islands, or separatrices [19]. For example, a third order resonance in one plane, under certain conditions, will produce islands in the phase space, like those seen in part a) of Fig.2.6.

In the non-resonant plane, p_2, q_2, the phase space is elliptical and the linear action angle variables are still good approximations. When looking at the cross planes, q_1, q_2, and p_1, p_2 the motion is rectangular and doesn't have a particular structure (or correlation).

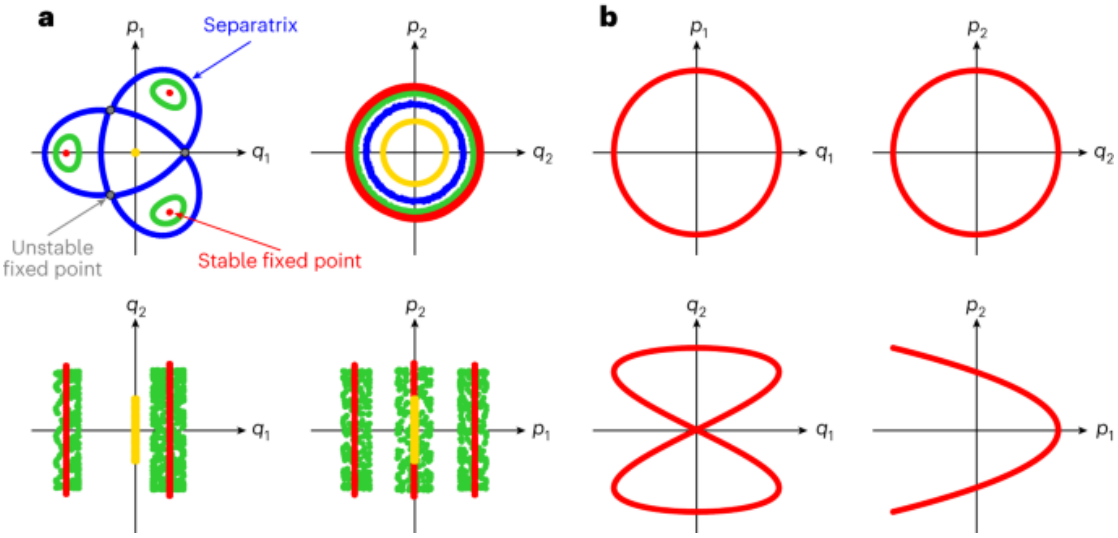

Figure 2.6: The motion under a 1D resonance is shown on the top left in the canonical variables. The motion in the other canonical plane is circular in the phase space. In the cross planes, there is no dependence (rectangular), a). For 2D resonances, there is a structure in the cross planes, b), and there is no visible structure in the 1D planes. Taken from [19].

For '2D' resonances, meaning that both the coefficients n_x, n_y, of equation 2.30 are non-zero, the trapped particles follow 4D structures in phase space, which look linear in the 1D planes, p_1, q_1 and p_2, q_2. The structure, a so called 'fixed-line' depends on the order of the 2D resonance. There have been recent analytical, simulation and experimental investigations to prove the existence and describe how the fixed lines affect the particle dynamics [19], [20]. An experiment to characterize the fixed lines in 2017 in the CERN Proton Synchrotron (PS) observed the creation of asymmetric halos, due to particles becoming resonant due to a third order resonance, $Q_x + 2Q_y = 19$ and scattered to higher amplitudes by the fixed-line trajectories [21].

The important result for this thesis is that the structures give a higher-order dependence between the amplitudes in the cross planes. This recent experimental and analytical work inspired the experimental campaign in the Proton Synchrotron Booster in Chapter 4, on whether this type of dynamics can introduce non-factorization into the beam distribution. **Non-factorization is when a density function cannot be factorized into functions of the individual variables**, like,

$$\rho(x, y, z) = \rho_x(x)\rho_y(y)\rho_z(z). \tag{2.33}$$

2.3 Luminosity

The figure of merit for a collider, is the luminosity. The luminosity of colliding beams is the convolution of a 3D particle distribution [22], given in terms of the Frenet-Serret coordinates, [23], [24].

$$\mathscr{L} \propto K \cdot \iiiint_{-\infty}^{\infty} \rho_1(x,y,s,-s_0)\rho_2(x,y,s,s_0)\,dx\,dy\,ds\,ds_0. \tag{2.34}$$

Where ρ are the particle densities and K is the kinematic constant defined,

$$K = \sqrt{(\vec{v}_1 - \vec{v}_2)^2 - (\vec{v}_1 \times \vec{v}_2)^2/c^2}. \tag{2.35}$$

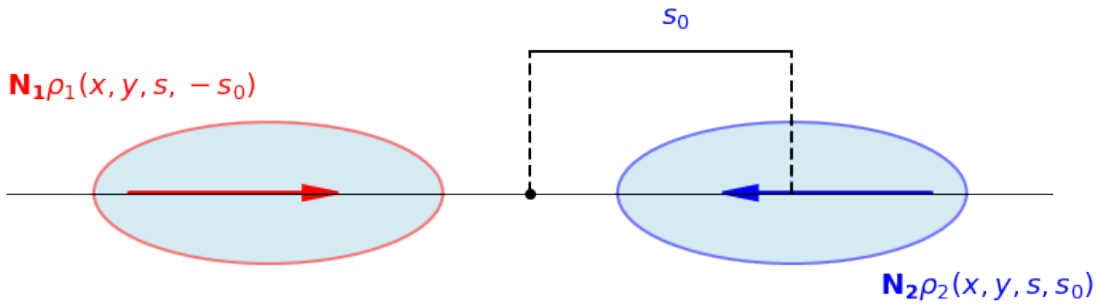

Figure 2.7: Two counter-rotating bunches colliding head-on.

If the particle distributions are factorizable and the collision is head-on, then the formula can be simplified,

$$\mathscr{L} = 2N_1N_2\nu_r N_b \iiiint_{-\infty}^{+\infty} \rho_{1x}(x)\rho_{1y}(y)\rho_{1s}(s-s_0)\rho_{2x}(x)\rho_{2y}(y)\rho_{2s}(s+s_0)\,dx\,dy\,ds\,ds_0. \tag{2.36}$$

A high integrated luminosity is desirable for particle physics experiments, given by equation 2.37, integrated between two time periods, (t_1, t_2). The quality of data depends on the statistical precision, increased by more events (more luminosity), and their ability to measure the luminosity and cross-sections, which will be discussed further in this chapter. The integrated luminosity is dependent not only on the beam distribution, but the machine availability. Machine availability can be linked to the beam dynamics, as large, concentrated losses in parts of the machine will lead to a machine 'dump', i.e. removal of the beam from the machine and a re-filling of proton bunches.

The integrated luminosity is given by,

$$\mathscr{L}_{\text{int}} = \int_{t_1}^{t_2} \mathscr{L}\, dt, \tag{2.37}$$

and the number of events is proportional to the integrated luminosity and the cross-section of an interaction,

$$N_{\text{events}} = \mathscr{L}_{\text{int}}\sigma. \tag{2.38}$$

2.4 van der Meer scans and Non-Factorization

Whilst the integrated luminosity is a performance indicator, and a high integrated luminosity is desired by the experiments to produce many events, it is also important to accurately measure the luminosity in order to measure cross-sections. The calibration of the luminosity measurement improves the precision of the cross-section measurement [25]. The systematic uncertainty from the instantaneous luminosity measurement can be a large source of error to cross-section measurements [26]–[28].

The following is taken from [29]. Interactions between protons are seen as observables in the luminosity detector. The average number of observables over many measurements is given by,

$$\begin{aligned}\langle N_{\text{observables}}\rangle &= \langle N_{\text{observables/interaction}}\rangle\langle N_{\text{interactions}}\rangle \\ &\equiv \langle N_{\text{observables/interaction}}\rangle\mu,\end{aligned}$$

Where μ is the average number of interactions per bunch crossing. μ is proportional to the single-bunch crossing instantaneous luminosity, $\mathscr{L}_b$, via the frequency of revolution of the bunches, ν_r (LHC revolution frequency), and the interaction cross-section, σ,

$$\mu = \frac{\sigma\mathscr{L}_b}{\nu_r}. \tag{2.39}$$

To measure the luminosity, the rate of observation is scaled to the luminosity with a calibration constant, σ_{vis},

$$\mathscr{L}_b = \frac{\langle N_{\text{observables}}\rangle}{\langle N_{\text{observables/interaction}}\rangle}\frac{\nu_r}{\sigma} \equiv \langle N_{\text{observables}}\rangle\frac{\nu_r}{\sigma_{\text{vis}}}. \tag{2.40}$$

To calibrate the luminosity measurement, the van der Meer method is used [30], [31]. The two beams are transversely separated and scanned over each other to measure the σ_{vis}, which

relates the luminosity to the measured rate, μ.

If the luminosity can be expressed as

$$\mathscr{L}_b = \frac{\nu_r n_1 n_2}{A_{\text{eff}}}, \tag{2.41}$$

A_{eff} is the effective overlap between two bunches. As defined above in terms of the bunch densities,

$$\mathscr{L}_b = \nu_r n_1 n_2 \iint \rho_1(x,y)\rho_2(x,y)\,dx\,dy. \tag{2.42}$$

Then, if **the assumption is made the beam densities are factorizable** in x and y.

$$\frac{1}{A_{\text{eff}}} = \int f_1(x) f_2(x)\,dx \int g_1(y) g_2(y)\,dy \equiv \frac{1}{W_{\text{eff}}}\frac{1}{H_{\text{eff}}}. \tag{2.43}$$

W_{eff} and H_{eff} are the effective width and height of the 'luminous region'.

When the beams are displaced in the vertical (h) and the horizontal direction (w), then the luminosity varies. By scanning in the x and y directions with transverse offset (van der Meer scan, Fig.2.8), the W_{eff} and H_{eff} can be determined as,

$$W_{\text{eff}} = \frac{\iint f_1(x) f_2(x-w)\,dx\,dw}{\int f_1(x) f_2(x)\,dx} = \frac{\int \mathscr{L}_b(w,0)\,dw}{\mathscr{L}_b(0,0)}, \tag{2.44}$$

$$H_{\text{eff}} = \frac{\iint g_1(y) g_2(y-h)\,dy\,dh}{\int g_1(y) g_2(y)\,dy} = \frac{\int \mathscr{L}_b(0,h)\,dh}{\mathscr{L}_b(0,0)}. \tag{2.45}$$

For Gaussian beams, this simplifies to,

$$\Sigma_x = W_{\text{eff}} = \sqrt{2\sigma_x} \quad \text{and} \quad \Sigma_y = H_{\text{eff}} = \sqrt{2\sigma_y}, \tag{2.46}$$

and thus,

$$\sigma_{\text{vis}} = \mu_{\text{vis}} \frac{2\pi \Sigma_x \Sigma_y}{n_1 n_2}. \tag{2.47}$$

Where μ_{vis} is the visible rate. An example scheme of transverse beam separations can be seen in Fig. 2.9.

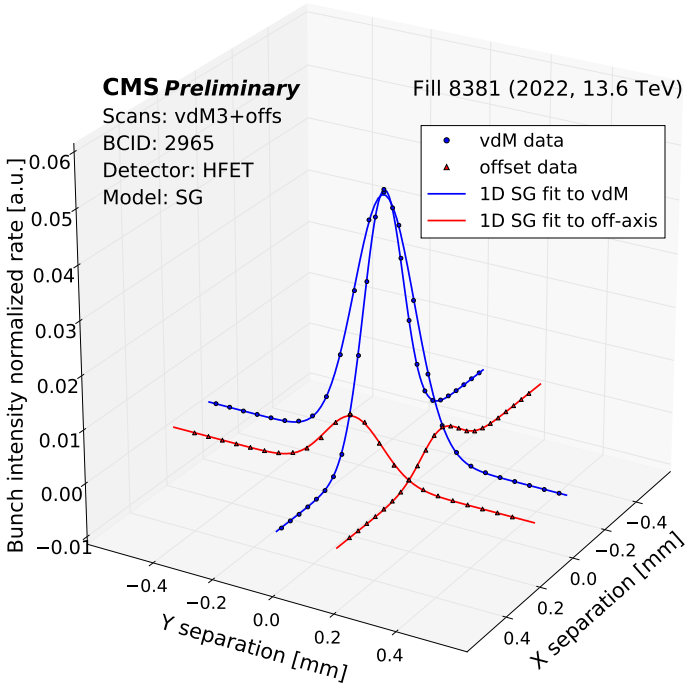

Figure 2.8: Measured rate reconstructed with offset van der Meer scans, from CMS van der Meer run 2022 [25].

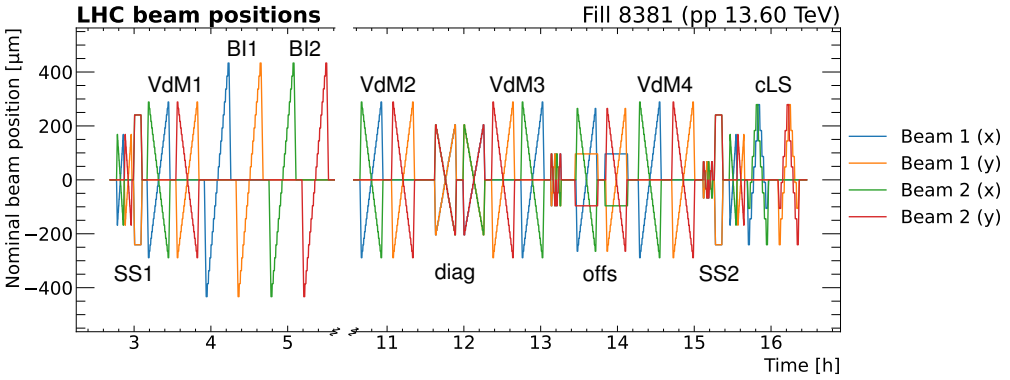

Figure 2.9: LHC beam positions during the different van der Meer scans of 2022, from [25]. Offs is an offset scan whilst diag is a diagonal scan (x-y varied).

There are various uncertainties associated with this measurement. The analysis of this measurement and the calculation of the uncertainties are independent for each experiment. **In 2022 for CMS, the largest bias was the uncertainty due to the non-factorization of the transverse beam distributions**, as seen in Table 2.1, from [32].

Source	**Uncertainty (%)**
Calibration	
Beam current	0.20
Ghosts & satellites	0.10
Orbit drift	0.02
Residual beam positions	0.16
Beam-beam effects	0.34
Length scale	0.20
Factorization bias	0.67
Scan-to-scan variation	0.28
Bunch-to-bunch variation	0.06
Cross-detector consistency	0.16
Integration	
Cross-detector stability	0.71
Cross-detector linearity	0.59
Calibration	0.89
Integration	0.92
Total	**1.28**

Table 2.1: Uncertainty sources and their corresponding percentages in the 2022 p-p van der Meer run of CMS, from [32].

The non-factorization correction to σ_{vis} is found by applying a fit to the $x-y$ distribution which describes the non-factorization seen. Depending on the fit function used, the size of the correction differs. Results from the 2022 run of CMS showed there was a dependence of the non-factorization correction to σ_{vis} on the bunch ID (bunch position in the filling scheme), shown in Fig. 2.10. Every 4th bunch had a lower non-factorization correction. This suggested a contribution to the difference in non-factorization bias which could have come from the different rings in the Proton Synchrotron Booster (a four ring machine, which are stacked on top of each other, with different magnet imperfections). The filling scheme is such that every 4th bunch comes from the same ring.

In 2023, ATLAS quoted that the preliminary uncertainty due to the non-factorization uncertainty was 1.39% [34], for a total uncertainty on the measurement of 2.04%. In 2022, the preliminary non-factorization uncertainty was 1.07%, for a total uncertainty on the measurement of 2.19% [35].

In the next chapter we will introduce non-factorization in terms of the observables seen by accelerator physicists and the beam dynamics.

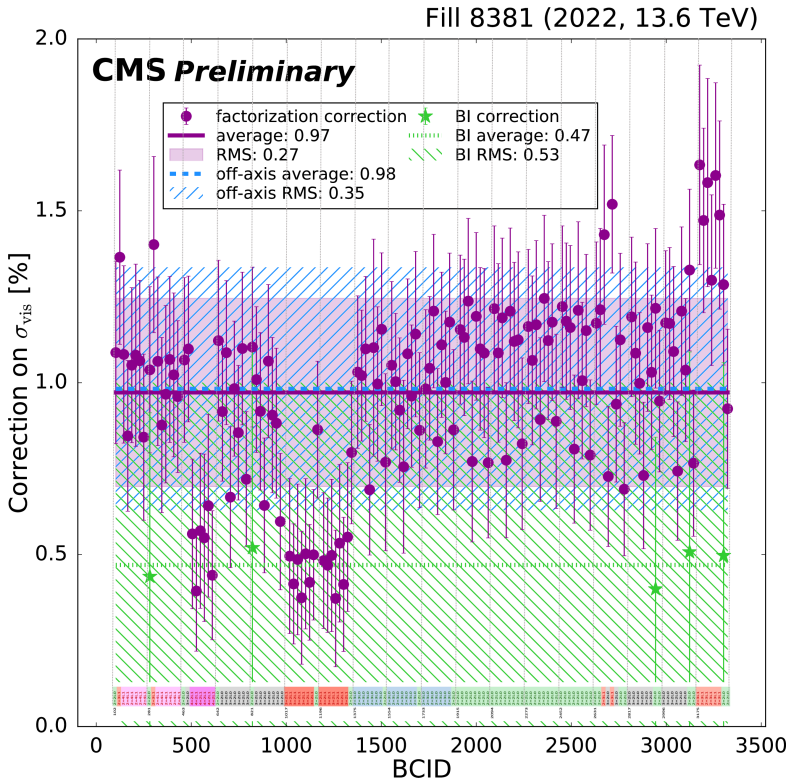

Figure 2.10: BCID (bunch ID) pattern in the LHC showing how the non-factorization correction for CMS varied bunch to bunch in the 2022 van der Meer scans. Every 4th bunch has a systematic lower correction [25], [33].

3 Reconstruction of Beam Distributions

During the operation of accelerators, it is important to control the beam profile, for example to minimize beam losses or optimise the luminosity of colliders. The beam profile is a projection of the total distribution onto one plane. In this chapter, we demonstrate that the beam profile alone is insufficient to characterize beam performance. We derive equations for different beam distributions from the observation of a profile (1D), to the full transverse distribution (4D), and show how the choice of constraints on the full distribution alter the luminosity and losses observed. We will show that the full distribution (4D), given a profile (1D), is not unique, even in the case of Gaussian beam profiles.

3.1 Definition of a Matched Distribution from the Hamiltonian

If the distribution is 'matched', then the distribution is stationary (i.e., invariant in time). Mathematically, a distribution (of a beam inside a system) is stationary if it is a function of the Hamiltonian of the system only [36].

We define the normalised transverse Hamiltonian in action-angle coordinates [7] in the two planes (can be a linear action-angle or the nonlinear action-angle),

$$\hat{H}_x = Q_x J_x \tag{3.1}$$

$$\hat{H}_y = Q_y J_y. \tag{3.2}$$

Where $Q_{x,y}$ are the transverse tunes (in the nonlinear case, the tunes depend on the action), and,

$$J_x = \frac{\hat{x}^2 + \hat{p_x}^2}{2} \tag{3.3}$$

$$J_y = \frac{\hat{y}^2 + \hat{p_y}^2}{2}. \tag{3.4}$$

Given the transverse planes are uncoupled, the full Hamiltonian is given by,

$$\hat{H} = \hat{H}_x + \hat{H}_y. \tag{3.5}$$

If the distribution function is a function of the Hamiltonian only,

$$f = f(\hat{H}(J_x, J_y)). \tag{3.6}$$

Then $f(\hat{H})$ is a constant of the motion if, and only if,

$$\frac{df}{dt} = 0. \tag{3.7}$$

Using the chain rule,

$$\frac{df}{dt} = \frac{df(\hat{H})}{d\hat{H}} \frac{d\hat{H}}{dt}, \tag{3.8}$$

and given that,

$$\frac{d\cdot}{dt} = \{\cdot, \hat{H}\} + \frac{\partial\cdot}{\partial t}. \tag{3.9}$$

Then,

$$\frac{d\hat{H}}{dt} = \{\hat{H}, \hat{H}\} + \frac{\partial\hat{H}}{\partial t}. \tag{3.10}$$

By definition [36],

$$\{\hat{H}, \hat{H}\} = 0. \tag{3.11}$$

Then, if the Hamiltonian does not depend explicitly on time,

$$\frac{\partial\hat{H}}{\partial t} = 0. \tag{3.12}$$

Thus,

$$\frac{df(\hat{H})}{dt} = 0. \tag{3.13}$$

Meaning, that the distribution is stationary, or 'matched', if it is a function of the Hamiltonian only, given the condition that the Hamiltonian does not depend on time [37]. Therefore, a 4D particle distribution in the normalised coordinates must be a function, of $f(\hat{x}^2 + \hat{p}_x^2, \hat{y}^2 + \hat{p}_y^2)$. As a direct consequence, this means that the (statistical) phase space in the canonical planes forms concentric circles. As we will see, given a particular beam profile, this gives only one solution for a 2D distribution, $f_{2D}(\hat{x}^2 + \hat{p}_x^2)$. However, the full 4D beam distribution is ambiguous as there is not a constraint on the way that the two planes are combined in order to satisfy the matching. **For convenience, for the rest of this chapter, we will re-label $\hat{x} \rightarrow x$ and similar for the other variables**. We will always assume to be in the normalised phase space.

3.2 Reconstruction of a 4D Distribution from a Beam Profile

Operationally, a wire scanner can measure the beam profile in the horizontal or the vertical plane. Mathematically, this is equivalent to performing the integral of the beam distribution over the other variables of the phase space.

Assuming a 4D phase space distribution $f_{4D}(x, p_x, y, p_y)$, the profile in the horizontal plane is obtained as,

$$f_{1D}(x) = \int_{-\infty}^{\infty}\int_{-\infty}^{\infty}\int_{-\infty}^{\infty} f_{4D}(x, p_x, y, p_y)\, dp_x\, dy\, dp_y. \tag{3.14}$$

If only the profile $f_{1D}(x)$ is known, and we want to invert the problem to find the 4D phase space distribution (in order to accurately model the physics), the solution is not unique. The constraints are that the projection of $f_{4D}(x, p_x, y, p_y)$ must match the observed $f_{1D}(x)$. In addition, the distribution $f_{2D}(x, px)$ and $f_{2D}(y, py)$ need to be circularly symmetric in the canonical planes $x - p_x$ and $y - p_y$, in order for the distribution to be matched to the Hamiltonian of the system.

From an observed beam profile, we can get the radial distribution of the canonical phase space variables using the Abel transform [38], [39], that is, $f_{2D}(x, px)$. The 4D beam distribution yielding the given 1D profile has infinite solutions, given no further constraints. To find two examples of the beam distribution in a higher dimension, we could impose one of the following additional constraints,

- Case 1) circular symmetry (i.e. round distributions in x-y, and all 2D sub-planes of the 4D distribution).
- Case 2) forcing the transverse planes to be factorizable.

Some equations are given without proof in [40] for circular symmetric distributions in 4D (case 1). We will demonstrate how to find any circular symmetric distribution from a given beam profile by using the Abel transform.

Interlude: The Abel Transform

3.2.1 The Abel Transform

To find the circular symmetric beam distributions in higher dimensions, as functions, we use the Abel transform. The Abel transform, originally proposed by Niels Henrik Abel [38], is an integral transform relationship between two functions. **Interpreted geometrically, the Abel transform allows the transformation between 2D circularly symmetric distributions and their projections in 1D**. We use the form from Bracewell, with $\alpha = 1/2$ [39], where the 'forward' transform is given by,

$$g(x) = \mathscr{A}[f(r)] = 2\int_x^\infty \frac{f(r)\,r\,dr}{\sqrt{r^2 - x^2}}. \tag{3.15}$$

Where $g(x)$ is the projection of a 2D circularly symmetric function which can be expressed as a function of a radius, r, and angle, θ, except it is uniform in θ, thus can be described by $f(r)$. $\mathscr{A}$ represents a shorthand for the forward Abel transform.
The inverse transform, $\mathscr{A}^{-1}$, verified with an ansatz [38], is given by,

$$f(r) = \mathscr{A}^{-1}[g(x)] = -\frac{1}{\pi}\int_r^\infty \frac{dg}{dx}\frac{dx}{\sqrt{x^2 - r^2}}. \tag{3.16}$$

It can be extended to higher dimensions, such as axial spherical symmetry (3D) [38], where a function $f(r)$ with $r = \sqrt{x^2 + y^2 + z^2}$ exists,

$$l(w) = 2\int_w^\infty \frac{f(r)\,r\,dr}{\sqrt{r^2 - w^2}}. \tag{3.17}$$

Here, the projection onto the yz plane is expressed as $l(w)$, where $w = \sqrt{y^2 + z^2}$.
The transform can be used in higher dimensions, so 4D for our use case (4D hyper-circular symmetry). Furthermore, the inverse Abel transform can be used as a test of physicality of a profile, as $f(r)$, given an $f(x)$ must be defined positive, detailed in Appendix B.

3.2.2 Defining Variables

For case 1, imposing circular symmetry in the $x-y$ planes, and thus hyper-circular symmetry in 4D, we define the following variables, or radii, from the canonical variables,

$$r_x = \sqrt{x^2 + p_x^2}, \tag{3.18}$$

$$r_y = \sqrt{y^2 + p_y^2}, \tag{3.19}$$

$$s = \sqrt{x^2 + p_x^2 + y^2}, \tag{3.20}$$

and a 4D 'super-radius',

$$m = \sqrt{r_x^2 + r_y^2} = \sqrt{x^2 + p_x^2 + y^2 + p_y^2}. \tag{3.21}$$

Given that $r_x = \sqrt{x^2 + p_x^2}$, and the phase space in 2D for canonical variables is circular, to find $f_{2D}(r_x)$, the inverse Abel transform is applied once on a profile $f_{1D}(x)$. To find $f_{4D}(m)$, the inverse Abel transform is applied three times to $f_{1D}(x)$ in accordance with the property of extension to higher dimensions. Thus, any 4D circular symmetric distribution can be found.

Using the previous defined variables, starting from a projection in 1D, e.g. in x, $f_{1D}(x)$, we obtain,

$$f_{2D}(r_x) = -\frac{1}{\pi}\int_r^\infty \frac{df_{1D}(x)}{dx}\frac{dx}{\sqrt{x^2 - r_x^2}}, \tag{3.22}$$

$$f_{3D}(s) = -\frac{1}{\pi}\int_s^\infty \frac{df_{2D}(r_x)}{dr_x}\frac{dr_x}{\sqrt{r_x^2 - s^2}}, \tag{3.23}$$

$$f_{4D}(m) = -\frac{1}{\pi}\int_m^\infty \frac{df_{3D}(s)}{ds}\frac{ds}{\sqrt{s^2 - m^2}}, \tag{3.24}$$

This is equivalent to

$$f_{4D}(m) = \mathscr{A}^{-1}[\mathscr{A}^{-1}[\mathscr{A}^{-1}[f_{1D}(x)]]]. \tag{3.25}$$

Conversely, we can compute the 1D distribution from a given 4D with forward Abel transforms, equivalent to a Cartesian integration in dp_x, dy, dp_y,

$$\begin{aligned} f_{1D}(x) &= \mathscr{A}[\mathscr{A}[\mathscr{A}[f_{4D}(m)]]] \\ &= \int_{-\infty}^{\infty}\int_{-\infty}^{\infty}\int_{-\infty}^{\infty} f_{4D}(m)\,dp_x\,dy\,dp_y. \end{aligned} \tag{3.26}$$

Given $f_{4D}(m)$, particles can be sampled from the distribution using an inverse sampling method, adapted from [40], detailed in Appendix A.

3.2.3 Example: Waterbag Distribution

The use of the Abel transform to find circular-symmetric distributions can be validated on the Waterbag and Parabolic distributions (which are defined in 2D), matching the 4D density functions given in [40].

Defining the 2D distribution $f_{2D}(r_x)$ as Waterbag yields,

$$f_{2D}(r_x) = \frac{2(1-\frac{r_x^2}{m_0^2})}{\pi m_0^2}, \tag{3.27}$$

$$f_{3D}(s) = \mathscr{A}^{-1}[f_{2D}(r_x)] = \frac{4\sqrt{m_0^2 - s^2}}{\pi^2 m_0^4}, \tag{3.28}$$

$$f_{4D}(m) = \mathscr{A}^{-1}[f_{3D}(s)] = \frac{2}{\pi^2 m_0^4}. \tag{3.29}$$

where $m < m_0$ defines the region where the distribution is non-zero.

3.2.4 Example: Parabolic Distribution

The case of a Parabolic 2D $f_{2D}(r_x)$ distribution yields,

$$f_{2D}(r_x) = \frac{1}{\pi m_0^2} 3(1-\frac{r_x^2}{m_0^2})^2, \tag{3.30}$$

$$f_{3D}(s) = \mathscr{A}^{-1}[f_{2D}(r_x)] = \frac{8(m_0^2 - s^2)^{3/2}}{\pi^2 m_0^6}, \tag{3.31}$$

$$f_{4D}(m) = \mathscr{A}^{-1}[f_{3D}(s)] = \frac{6(m_0^2 - m^2)}{\pi^2 m_0^6}. \tag{3.32}$$

It can be shown that these results are in agreement with the distributions in [40].

3.2.5 Example: q-Gaussian Distribution

We often observe beam distributions that are well-fitted by q-Gaussian distributions, such as those exhibiting heavy tails in the transverse planes [41], [42] in the CERN accelerator complex. The q-Gaussian can effectively describe these distributions and offers a unique solution, unlike the combination of two Gaussian distributions with different weights and σ. We can find the q-Gaussian distribution function for the hyper-circularly symmetric, case 1) distribution, starting from the 1D q-Gaussian [43],

$$f_{1D}(x) = \frac{\sqrt{\beta_q}}{C_q} e_q(-\beta_q x^2), \tag{3.33}$$

where e_q is defined as the q-exponential (defined positive),

$$e_q(x) = [1 + (1-q)x]_+^{\frac{1}{1-q}}. \tag{3.34}$$

The normalisation factor C_q is defined,

$$C_q = \begin{cases} \frac{2\sqrt{\pi}\Gamma\left(\frac{1}{1-q}\right)}{(3-q)\sqrt{1-q}\Gamma\left(\frac{3-q}{2(1-q)}\right)}, & \text{for } -\infty < q < 1 \\ \sqrt{\pi}, & \text{for } q = 1 \\ \frac{\sqrt{\pi}\Gamma\left(\frac{3-q}{2(q-1)}\right)}{\sqrt{q-1}\Gamma\left(\frac{1}{q-1}\right)}, & \text{for } 1 < q < 3. \end{cases} \tag{3.35}$$

Γ is the Gamma function. The distribution arises from the maximisation of the Tsallis entropy [44]. The q can be interpreted as how light or heavy tailed a distribution is compared to the Gaussian, ($q = 1$), and the β_q scales the distribution along x. For $q = 2$ it becomes the Cauchy distribution.

The variance of the distribution is given by,

$$\text{variance} = \begin{cases} \frac{1}{\beta_q(5-3q)}, & \text{for } q < \frac{5}{3} \\ \infty, & \text{for } \frac{5}{3} \leq q < 2 \end{cases} \tag{3.36}$$

The 1D profile is transformed to a 2D density via the inverse Abel transform,

$$\begin{aligned} f_{2D}(r_x) = &-\frac{\beta_q^{3/2}(q-3)\sqrt{q-1}r_x}{2\pi} \\ &\times \left(\frac{1}{\beta_q(q-1)r_x^2}+1\right)^{\frac{q+1}{2-2q}} \left(\beta_q(q-1)r_x^2\right)^{\frac{q}{1-q}}, \end{aligned} \tag{3.37}$$

Assuming a density in the form $f_{4D}(m)$, the equation for the 4D density function is obtained via two further inverse Abel transforms,

$$\begin{aligned} f_{4D}(m) = &-\frac{\beta_q(q-3)(q+1)\left(\frac{1}{\beta_q(q-1)}\right)^{\frac{1}{1-q}}}{4\pi^2 m^3 \Gamma\left(\frac{1}{q-1}\right)} \\ &\times (\beta_q(q-1))^{\frac{q+1}{2-2q}} \Gamma\left(\frac{q}{q-1}\right) \\ &\times \left(\frac{1}{\beta_q m^2(q-1)}+1\right)^{\frac{1}{1-q}-\frac{3}{2}} (\beta_q m^2(q-1))^{\frac{1}{1-q}}, \end{aligned} \tag{3.38}$$

which simplifies to,

$$f_{4\mathrm{D}}(m,q,\beta_q) = \left(-\frac{\beta_q^2(q-3)(q^2-1)}{4\pi^2}\right) \times \frac{\Gamma\left(\frac{q}{q-1}\right)}{\Gamma\left(\frac{1}{q-1}\right)} \times \left(1+\beta_q(q-1)m\right)^{\frac{1}{1-q}-\frac{3}{2}}. \tag{3.39}$$

This is valid for the specific case of q-values of $1 < q < 3$, calculated using Mathematica [45]. (In the CERN accelerator complex, typical q observed are 1-1.4).

To generate a particle distribution for factorizable distributions in $x-y$ (case 2), the 4D density function is a product of two 2D density functions, one in $x-p_x$ and one $y-p_y$, which are in themselves functions of only r_x and r_y. They can be found via one inverse Abel transform for each plane,

$$f_{4D}(r_x, r_y) = f_{2D}(r_x) \times f_{2D}(r_y). \tag{3.40}$$

The $x-p_x$ and $y-p_x$ distributions are then sampled via two separate Box-Müller type random sampling methods [46].

The population of the phase space with a q-Gaussian of $q = 1.4$ for case 1 yields the x-y projection shown in Fig. 3.1. The projection on the x or y planes (1D) is shown with the fit of a q-Gaussian with $q = 1.4$.

Figure 3.2 shows the projection of the density function made from the multiplication of two 2D distributions (case 2). As in case 1, the projection in x and y fits the q-Gaussian distribution with $q = 1.4$.

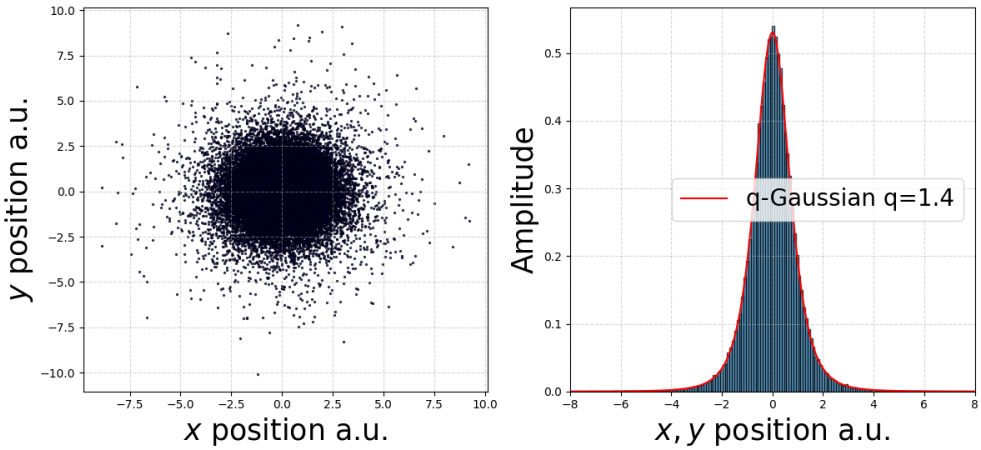

Figure 3.1: Projection in the $x-y$-plane (left) and the x-plane and y-plane (right) for a distribution with circular symmetry in all planes (case 1).

3.3 Losses

Taking the two (sampled) distributions of case 1 and 2, which give the same 1D profile, we can observe the behaviour under a loss process. Projecting on the $y-p_y$ plane, and making a collimation (or beam scraping) at 3 σ in both cases, the $y-p_y$ planes are identical, Fig 3.3.

Depending on if the distribution is case 1 or case 2, the behaviour under a loss process changes

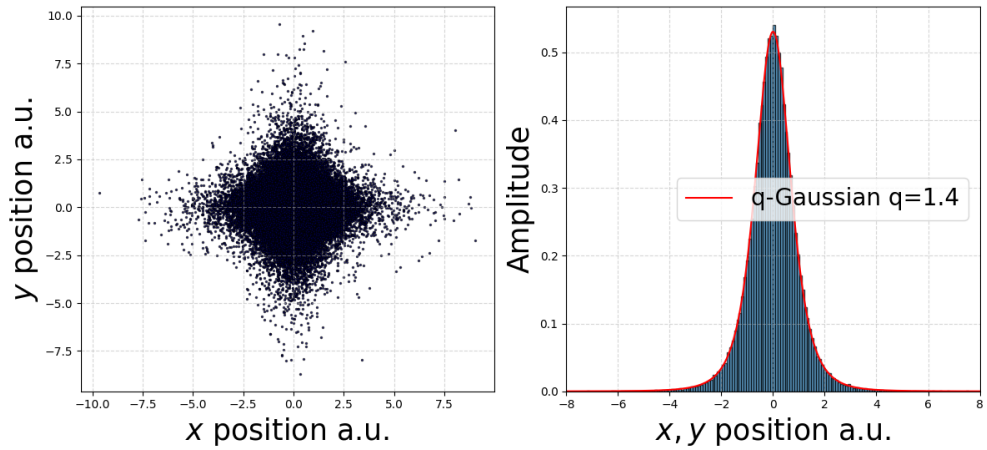

Figure 3.2: Projection in the $x-y$-plane (left) and the x-plane and y-plane (right) for a factorizable distribution (case 2).

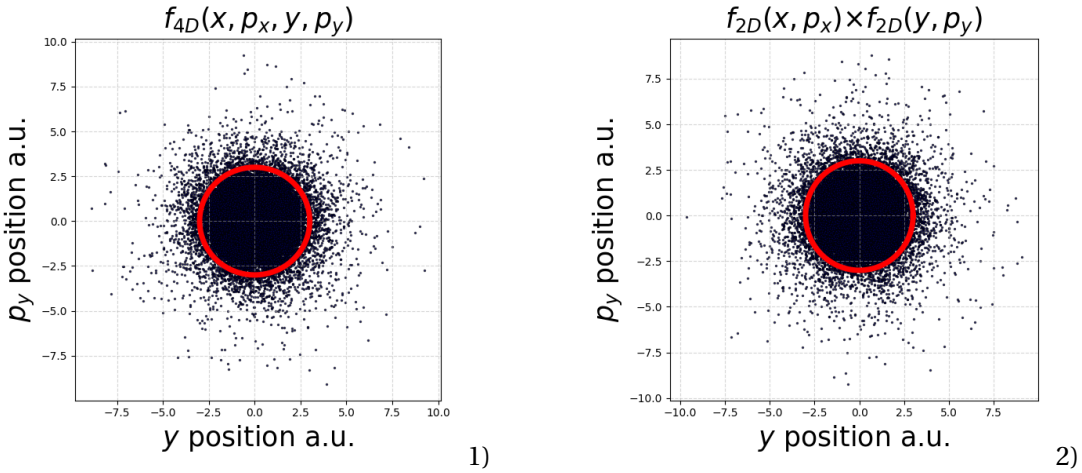

1) 2)

Figure 3.3: Collimation at 3 σ in the y plane is the circular cut in the $y-p_y$ plane, identical for both case 1) and case 2) distributions.

on the x plane in addition to the scraping plane, y. This can be seen by the probability density of the removed particles by the y aperture seen in Fig. 3.4. The $x^2+p_x^2$ of the removed particles by a y aperture have a different distribution to the original $x^2+p_x^2$ distribution. This is a consequence on the non-factorization of the function.

3.4 Non-Factorization

We have shown that the 4D distribution is not unique, given the same f_{1D}. This is a consequence of the free parameters, as the distribution only requires circular symmetry in the canonical planes, and this condition is identical to the matching condition, $f(\hat{H})$. For the circular symmetric case (for the non-Gaussian cases), the distribution is non-factorizable, and

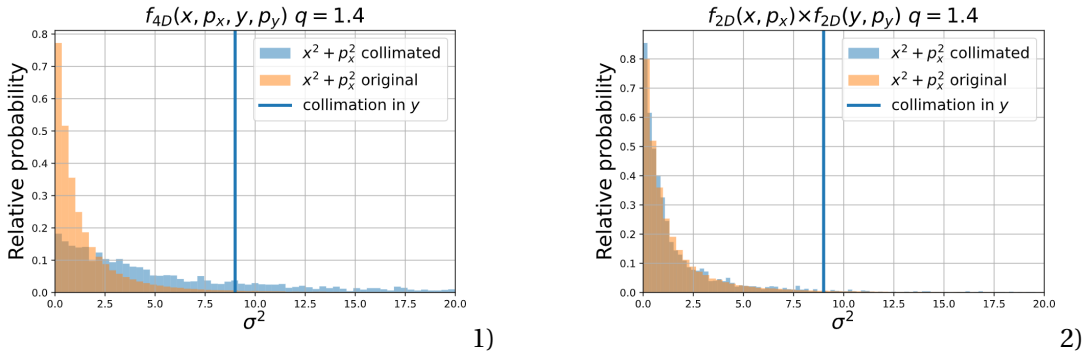

Figure 3.4: The x distribution x of the removed particles due to the cut in y, has a different result for the case 1) and case 2) distribution.

as a consequence we saw the difference in loss behaviour. Non-factorizable means,

$$f_{4D}(x, p_x, y, p_y) \neq f_{2D}(x, p_x) f_{2D}(y, p_y). \tag{3.41}$$

To show that the non-factorizable distribution is matched, we can plot the Σ matrix, the case 1) f_{4D} derived above, with a $q = 1.4$, shown in Fig. 3.5. The Σ matrix is diagonal beyond numerical noise due to the sampling, thus there is no linear coupling in the distribution, (a matched distribution in linear normalised phase space is uncoupled, i.e. the Σ matrix is diagonal). The non-factorization cannot be observed by second order moments, as it does not depend on phase but on amplitude.

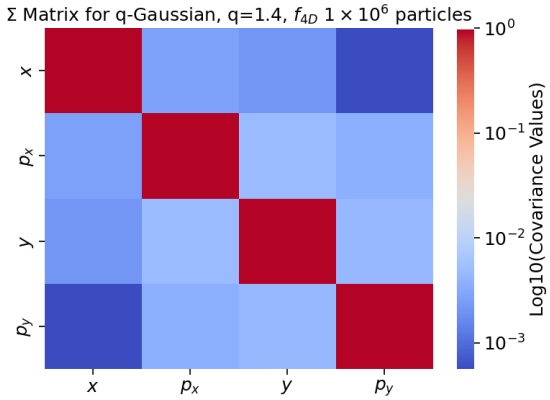

Figure 3.5: The Σ beam matrix for a circular symmetric q-Gaussian distribution with a $q = 1.4$ and 2e6 particles.

3.5 Luminosity

The luminosity of particle colliders depends, among other parameters, on the transverse profiles of the colliding beams. At the LHC at CERN, heavy-tailed transverse beam distributions

are typically observed. The luminosity is usually modeled with the assumption that the x-y planes are factorizable (i.e. statistically uncorrelated particle distributions between the planes) in each beam. Below, we evaluate the relative luminosity difference for q-Gaussian profiles with different 4D distributions. We calculate the luminosity for the circularly-symmetric distributions as,

$$\mathscr{L} \propto \int_{-\infty}^{\infty}\int_{-\infty}^{\infty} f_1(x,y)\, f_2(x,y)\, dx\, dy. \tag{3.42}$$

The integral is done numerically using Eq. (3.37) for $f_{1,2}(x,y)$, replacing r_x with $\sqrt{x^2+y^2}$.

For factorizable beam distributions, we obtain the luminosity as,

$$\mathscr{L} \propto \int_{-\infty}^{\infty}\int_{-\infty}^{\infty} f_1(x)\, f_1(y)\, f_2(x)\, f_2(y)\, dx\, dy, \tag{3.43}$$

where $f_{1,2}(x)$ and $f_{1,2}(y)$ are the q-Gaussian 1D distributions, and 1,2 denote the two incoming bunches.

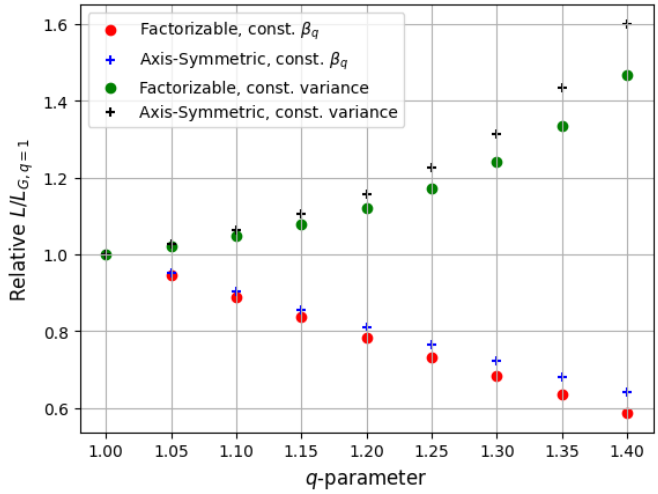

Figure 3.6: Luminosity variation for different q, but the same β_q (red and blue markers), and for constant variance (green and black markers), with hyper circularly-symmetric (crosses) or factorizable (points) distributions in x-y.

Figure 3.6 shows the luminosity for case 1) and case 2), given the constraint of a q-Gaussian profile in the x and y planes, relative to a 4D circular-symmetric Gaussian distribution ($q = 1$). The graph shows, as a function of q, a set of q-Gaussian distributions with constant variance and another set keeping β_q constant. The difference in relative luminosity between non-factorizable, circularly symmetric (case 1) and factorizable (case 2) distributions becomes larger as the q-parameter increases. This shows that it is important to know the properties of the full phase space distribution to accurately calculate the luminosity integrals.

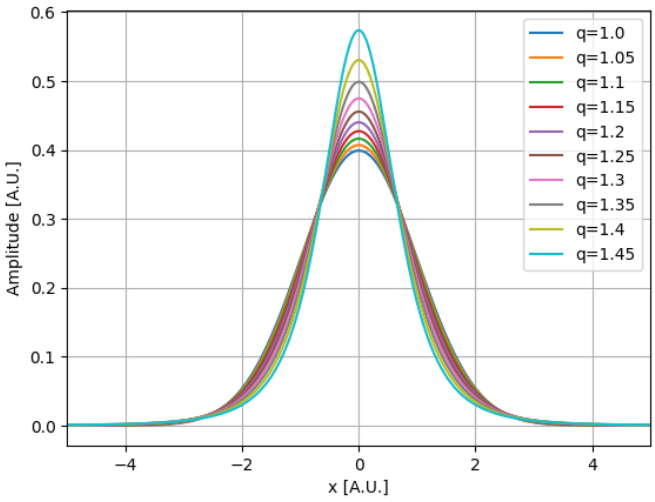

Figure 3.7: The profile for a q-Gaussian with different q-parameters for constant variance.

For completeness, Fig. 3.7 shows the q-Gaussians beam profiles (1D projections of the phase space) corresponding to the same q-parameters as in Fig. 3.6 for the case of constant variance.

Note: Non-factorizable Gaussian beam distributions

3.6 Non-Factorizable Gaussian Beam Distributions

Circularly symmetric, $x-y$ Gaussian distributions are factorizable. However, distributions which have 1D Gaussian projections, do not have to have a factorizable f_{4D}, as demonstrated in a notebook by G. Sterbini, attached in the Appendix E.
Given a 4D distribution for the canonical variables x, p_x, y, p_y in normalised phase space; if the 1D projections are Gaussian, that is,

$$\int_{-\infty}^{+\infty} \rho(x,y)\,dy = \frac{1}{\sqrt{2\pi}} e^{-\left(\frac{x}{\sigma}\right)^2} \quad \text{(Gaussian x-profile)}, \tag{3.44}$$

and

$$\int_{-\infty}^{+\infty} \rho(x,y)\,dx = \frac{1}{\sqrt{2\pi}} e^{-\left(\frac{y}{\sigma}\right)^2} \quad \text{(Gaussian y-profile)}. \tag{3.45}$$

Considering the action-angle variables, J_x, and θ_x where

$$J_x = \frac{x^2 + p_x^2}{2} \tag{3.46}$$

it is shown that, given the constraints that the marginal probability density function (PDF), PDF$(J_y|J_x)$ is a solution of these equations,

$$\int_0^{+\infty} e^{-J_x} \text{PDF}(J_y|J_x) dJ_x = e^{-J_y} \tag{3.47}$$

$$\int_0^{+\infty} \text{PDF}(J_y|J_x) dJ_y = 1, \tag{3.48}$$

for all J_x.
There are two possible solutions for PDF$(J_y|J_x)$,

$$\text{A1.PDF}(J_y|J_x) = e^{-J_y}, \tag{3.49}$$

$$\text{A2.PDF}(J_y|J_x) = \delta(J_y - J_x). \tag{3.50}$$

The distributions look like, in x, y, for the A1. case Fig.3.8 and for the A2. case Fig.3.9.

The corresponding Σ matrices for a sample extracted on from these functions, with 1×10^6 particles, in the A1. case, Fig. 3.10 and in the A2. case 3.11. Both matrices are diagonal, and are matched to the lattice, in a normalised linear phase space. However, for the case A2., the x and y distributions are non-factorizable.

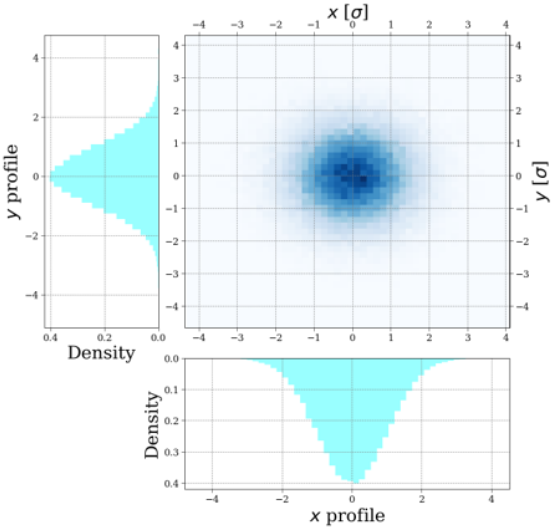

Figure 3.8: The A1. case for a Gaussian distribution plotted in the $x-y$ and x and y planes.

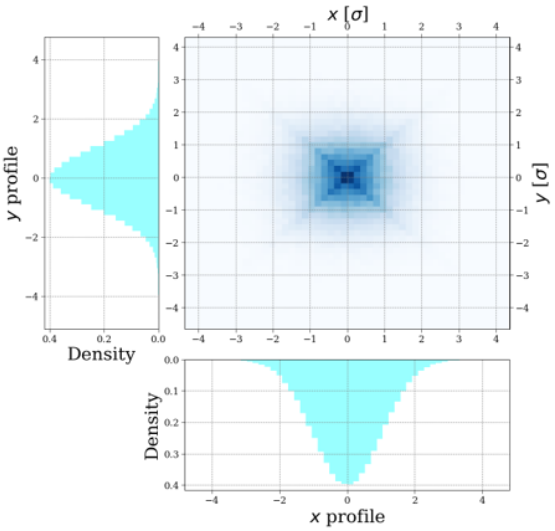

Figure 3.9: The A2. case for a Gaussian distribution plotted in the $x-y$ and x and y planes.

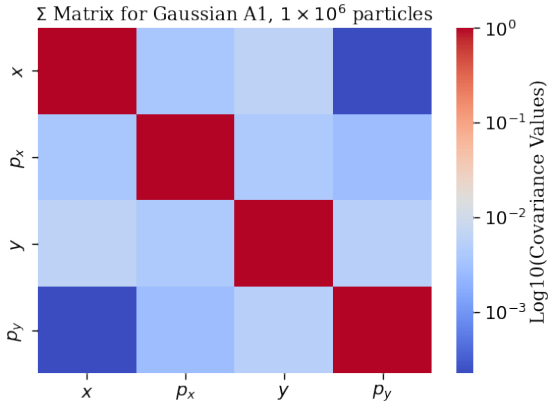

Figure 3.10: The Σ matrix for the distribution (A1.) showing that it is un-coupled.

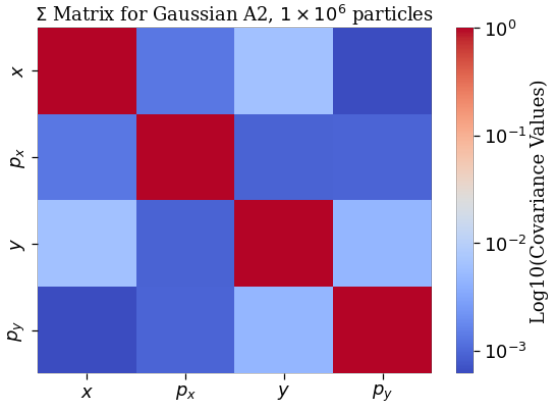

Figure 3.11: The Σ matrix for the distribution (A2.) showing that it is uncoupled as the matrix is diagonal.

3.7 Measuring Non-Factorization

We have shown that it is important to know the full transverse distribution in order to correctly model the luminosity and the losses in a collider. Below, we propose a method for the measuring of the transverse phase space via destructive scraping or collimation, with no manipulation of the machine optics. In addition to luminosity and losses, the non-factorization of the bunch results in an important error on the calibration of the luminosity measurement. An undeveloped version of the following method has been used, in Chapters 4, and 6 to find the relative non-factorization of a beam distribution in order to find optimum configurations for the van der Meer bunches (as factorizable as possible) in terms of the injector machine parameters. In the lower injector machines there are no instruments which measure the full transverse phase space.

In the LHC, the transverse beam distribution can be measured with the BSRT (Synchrotron-Light Telescope) or the Coronagraph (uses the synchrotron light but through a lens to amplify the beam halo), [47]. The BSRT has a noise limit on the beam halo measurement [48], and the coronagraph is not operational as of 2024.

3.7.1 Reconstruction of PDF(J_x, J_y) with Beam Scraping

A beam scraper (also referred to as a collimator), is an aperture which is controlled during operation to remove higher amplitude particles in the distribution. Their main purpose is for machine protection, in order to prevent damage to equipment. Beam scraping has been used for diagnostics in LHC experiments to find the diffusion coefficient, tail population, loss rates, and for the detection of beam oscillations [49], [50]. We can also probe the PDF(J_x, J_y) distribution with scraping measurements.

Going to the distribution in the J_x, J_y plane is advantageous when working with an aperture. For example, in the vertical plane, the y and p_y evolve with the vertical tune, however the J_y is constant, and thus the aperture can be modeled as a cut in the beam distribution above a limit. In Appendix C it is detailed how to calculate the 1D beam profile from an aperture limit with the Abel transform. To determine the 4D distribution we can do the following.

Before any scraping in the y plane, a y profile measurement plus a transformation results in a measurement:

$$\text{PDF}(J_y). \tag{3.51}$$

After a vertical scraping, where the scraper is placed at an aperture, A_i, in the J_y space of $J_y = A_i$, we have the new conditional PDF of the y plane, found with a measurement in the y plane and the Abel transform.

$$\mathrm{PDF}(J_y|J_y < A_i). \tag{3.52}$$

If we make a simultaneous measurement in the x plane of the 1D profile, we have another PDF,

$$\mathrm{PDF}(J_x|J_y < A_i). \tag{3.53}$$

Successive measurements, of the beam profile in both x and y, with different y apertures (decreasing in amplitude), provide us with a series of discrete conditional probability density functions.

The protocol can be represented by a matrix,

	$0 < J_y < A_n$	$0 < J_y < A_{n-1}$	$\cdots$	$0 < J_y < A_1$	$0 < J_y < A_0$
$J_{x,0}$	$a_{n,0}$	$a_{n-1,0}$	$\cdots$	$a_{1,0}$	$a_{0,0}$
$J_{x,1}$	$a_{n,1}$	$a_{n-1,1}$	$\cdots$	$a_{1,1}$	$a_{0,1}$
$\vdots$	$\vdots$	$\vdots$	$\ddots$	$\vdots$	$\vdots$
$J_{x,m-1}$	$a_{n,m-1}$	$a_{n-1,m-1}$	$\cdots$	$a_{1,m-1}$	$a_{0,m-1}$
$J_{x,m}$	$a_{n,m}$	$a_{n-1,m}$	$\cdots$	$a_{1,m}$	$a_{0,m}$

(3.54)

Given that A_i are the scraping amplitudes of the scraping protocol, and A_{i+1} is the next scraping aperture in time, if the collimator starts far from the beam at $J_y = A_0$. To find $\mathrm{PDF}(J_x|A_{i+1} < J_y < A_i)$ from the $\mathrm{PDF}(J_x|0 < J_y < A_i)$, we need to sum for different A_i,

$$\mathrm{PDF}(J_x \mid A_i < J_y < A_{i+1}) = \sum_{j=1}^{i+1} \mathrm{PDF}(J_x \mid 0 < J_y < A_j) - \sum_{j=1}^{i} \mathrm{PDF}(J_x \mid 0 < J_y < A_j), \tag{3.55}$$

yielding the discrete matrix $\mathrm{PDF}(J_x \mid A_i < J_y < A_{i+1})$,

	$0 < J_y < A_n$	$A_n < J_y < A_{n-1}$	$\cdots$	$A_2 < J_y < A_1$	$A_1 < J_y < A_0$
$J_{x,0}$	$a'_{n,0}$	$a'_{n-1,0}$	$\cdots$	$a'_{1,0}$	$a'_{0,0}$
$J_{x,1}$	$a'_{n,1}$	$a'_{n-1,1}$	$\cdots$	$a'_{1,1}$	$a'_{0,1}$
$\vdots$	$\vdots$	$\vdots$	$\ddots$	$\vdots$	$\vdots$
$J_{x,m-1}$	$a'_{n,m-1}$	$a'_{n-1,m-1}$	$\cdots$	$a'_{1,m-1}$	$a'_{0,m-1}$
$J_{x,m}$	$a'_{n,m}$	$a'_{n-1,m}$	$\cdots$	$a'_{1,m}$	$a'_{0,m}$

(3.56)

Making an approximation from discrete to a continuous distribution, to find,

$$\mathrm{PDF}(J_x|J_y = A_y), \tag{3.57}$$

and given Bayes' theorem;

$$\mathrm{PDF}(J_x, J_y) = \mathrm{PDF}(J_x|J_y) \times \mathrm{PDF}(J_y), \tag{3.58}$$

$\mathrm{PDF}(J_x, J_y)$ can be reconstructed. ($\mathrm{PDF}(J_y)$ is the marginal distribution which can be found from a profile measurement in y before scraping).

To find the distribution in x, p_x, y, p_y, a rotation is used,

$$x = \sqrt{2J_x}\cos(\theta_x) \tag{3.59}$$
$$p_x = -\sqrt{2J_x}\sin(\theta_x) \tag{3.60}$$
$$y = \sqrt{2J_y}\cos(\theta_y) \tag{3.61}$$
$$p_y = -\sqrt{2J_y}\sin(\theta_y). \tag{3.62}$$

The angle, $\theta_{x,y}$, is uniformly distributed. A numerical example to find the $\mathrm{PDF}(J_x, J_y)$ for the A1. and A2. Gaussian distributions is given in Appendix D. This method is not well-developed for experiment as of writing, as it depends greatly on the noise of the profile measurement, and the rate of diffusion during the period of the measurement. Scraping and profile measurements in both planes has however been used to determine the **relative** non-factorization between distributions in Chapters 4 and 6.

3.8 Summary

It has been shown that given a beam profile, the transverse distribution is not unique. The losses and luminosity depend on the full transverse distribution. We have seen that non-factorizable distributions (not coupled) can be stationary (in linear and nonlinear machines, for integrable motion). It has also been shown that even distributions giving Gaussian profiles can be non-factorizable.

To increase the non-factorization in a distribution it requires a mechanism that gives energy, or takes away energy from a particle's x and y position simultaneously. In the next few chapters, we will show experimentally (Chapter 4), and with simulation (Chapter 5), how non-factorization can be introduced into the distribution through coupled resonance crossing in the presence of space charge. We will also demonstrate through experiment how the non-factorization is preserved in a synchrotron, and can be passed to higher energy machines (Chapter 6). This will be discussed in reference to the van der Meer measurements and the minimisation of the uncertainty due to the non-factorization.

4 Experiment of Periodic Resonance Crossing in the CERN PSB

4.1 Introduction

As we demonstrated in the Chapter 3, an in depth characterisation of the beam distribution is paramount to anticipate the luminosity performance and how the beam will behave under loss processes, (particularly for high brightness beams, when the losses can cause machine damage). Beam profile measurements are the projection of the 6D phase space distribution onto a single axis (one of the horizontal, vertical and longitudinal planes). Inversions of the profile to a full distribution do not yield unique solutions, and both factorizable and non-factorizable distributions can be matched and fit the measured projections. For non-factorizable distributions, selecting the amplitude of a particle in one plane will condition the amplitude distribution in another plane. This impacts in a macroscopic way the evolution of the particle distributions; losing a particle in one plane affects the (normalised) profile in the other. This can be observed experimentally through scraping of the beam tail, and measurement of the beam profile in the other planes.

Crossing of coupled $x-y$ resonances is one mechanism that could introduce the aforementioned non-factorization. Due to the synchrotron motion in bunched beams, particles change their position within the longitudinal profile. The space charge tune spread depends on the local line charge density, and thus it is changing as the particles move towards the centre of the bucket. Particles which were initially not resonant become resonant as their tune approaches the resonant condition. The motion follows structures in the 4D phase space, resembling Lissajous figures. The particles x, y position is affected simultaneously. When the particles no longer meet the resonant condition, the non-factorization persist as the Courant-Snyder amplitudes in $x-p_x$, $y-p_y$ of a given particle are preserved [51], as will be seen in the next two chapters. The dynamics under coupled-resonances and the structures formed in the 4D phase space, or 'fixed-lines' has been the subject of recent experimental and analytical investigations, [19]–[21], [52].

In 2017, it was shown that periodic resonance crossing of coupled resonances introduces

an asymmetric halo in the transverse planes. The experiment was carried out in the CERN Proton Synchrotron, the machine after the Proton Synchrotron Booster in the CERN proton injector chain. The idea behind the experiment shown in this chapter was to **induce a similar halo in the bunch via periodic resonance crossing of a coupled resonance, and measure the non-factorization between planes using beam scraping and profile measurements after excitation of the resonance had been removed (almost linear machine)**. The results also show how excitation of a 1D resonance does not introduce asymmetric halos and furthermore does not change the non-factorization of the transverse planes.

4.2 Experimental Configuration

The measurement campaign was performed at the CERN Proton Synchrotron Booster (PSB), which is a machine with four superposed rings with a common magnetic yoke, and all experiments were conducted in Ring 1, the bottom ring. The driving terms of the relevant lattice resonances for the chosen working points were corrected for, similarly to as detailed in [53]. This enabled controlled excitation of the selected resonance. Two experimental configurations are presented: the working point $(Q_x, Q_y) = (4.11, 4.36)$ near a third order resonance (1D) $3Q_y = 13$, and $(Q_x, Q_y) = (4.18, 4.44)$ near a coupled third order resonance (2D) $Q_x + 2Q_y = 13$. The tune spreads due to space charge are around $\Delta Q_x = -0.11$, $\Delta Q_y = -0.14$, calculated using [54]. The code calculates resonance driving terms by including the space charge potential of a Gaussian beam in the Hamiltonian. The tune spreads can be seen in fig. 4.2 and fig. 4.1.

Figure 4.3 illustrates the experimental configuration of the cycle. The measurements were performed at the 160 MeV injection plateau, during which a single bunch of $\sim 4 \times 10^{11}$ protons was stored. The lattice resonance compensation was maintained during the whole cycle. Measurements were performed with either no resonance excitation, or with a resonance excitation for a period of 220 ms using a skew or normal sextupole, depending on the selected resonance. Following a period of $\sim$ 30 ms ($\sim 3 \times 10^4$ turns), corresponding to $\sim$20 synchrotron periods after the excitation was removed, high amplitude particles of the vertical profile were scraped away via a controlled vertical closed orbit bump moving the beam onto a dedicated aperture restriction. Profile measurements in the horizontal and vertical plane were taken with the wire scanners after the scraping process, along with tomoscope measurements [55] for the longitudinal plane. The sextupole current and vertical orbit bump were varied to test how the non-factorization changes as function of the particle amplitude for different resonance excitations.

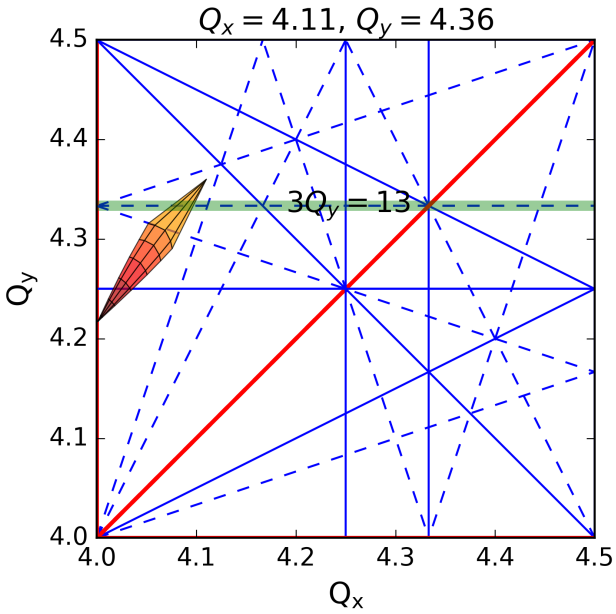

Figure 4.1: The set working point of the $3Q_y = 13$ experiment with the estimated space charge tune-spread assuming a Gaussian beam profile and the measured emittances. The excited resonance is shown in green.

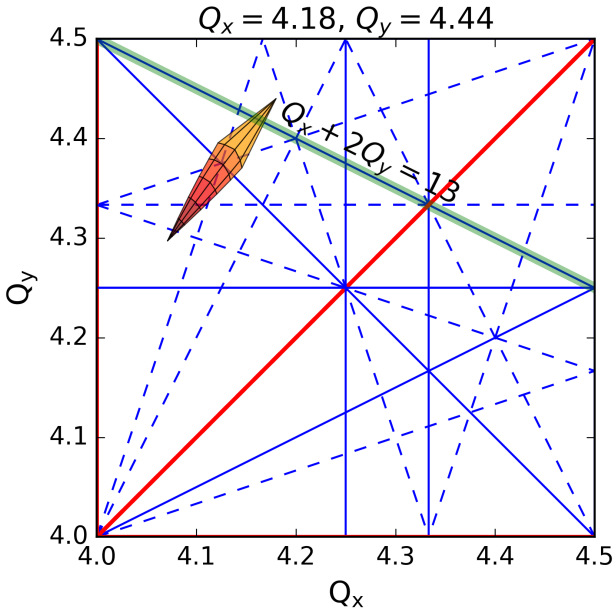

Figure 4.2: The set working point of the $Q_x + 2Q_y = 13$ experiment with the estimated space charge tune-spread assuming a Gaussian beam profile and the measured emittances. The excited resonance is shown in green.

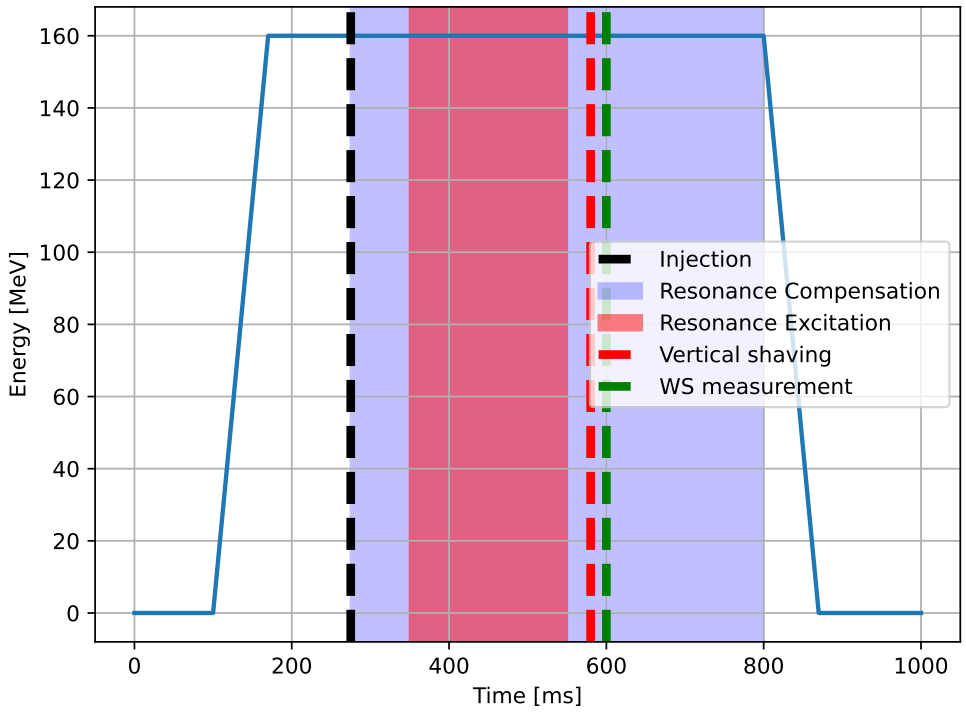

Figure 4.3: The experimental configuration along the 160 MeV injection plateau in the PSB.

4.3 Experimental Results

The initial (after injection, no resonance excitation) profiles in the horizontal, vertical, and longitudinal planes can be seen from screenshots of the PSB logbook Fig. 4.4. The initial normalised emittances were 2.1 μm·rad in H and 1.4 μm·rad in V. The longitudinal bunch profile is parabolic. The longitudinal parameters were optimised to have a small $\frac{\Delta p}{p}_{\text{rms}}$ in order to minimise the effect of dispersion on the beam profile, see Fig. 4.5.

Data taking periods were done with automatic scripting; it was paramount to have the scraping measurements for a single resonance on the same day, and to avoid effects due to hysteresis (which could affect the correction of the RDTs). The automatic scripting helped with the acquisition of numerous measurements for statistics.

Figure 4.6 displays the vertical, horizontal and longitudinal profiles for different scraped intensities (done with the vertical orbit bump), with and without the resonance excitation. When the $3Q_y = 13$ resonance is not excited, the profiles (normalised to intensity) remain constant in the non-scraping planes (apart from the reproducibility of measurements). When the $3Q_y$ resonance is excited, large tails can be observed in the vertical plane, which are clearly removed by the scraping. Furthermore, the vertical scraping also changes the longitudinal profile resulting in reduced bunch length, as particles with large vertical amplitude also have high longitudinal amplitude. The horizontal profile is not changing, as the 1D resonance crossing moves particles to higher amplitudes in the vertical plane only for $3Q_y = 13$.

Figure 4.7 shows the beam profiles in all three planes when measured after the vertical scraping for the resonance $Q_x + 2Q_y = 13$ for different scraped intensities, with and without the excitation during the cycle. As the beam is scraped vertically, for the case with no excitation, the normalised longitudinal and horizontal profile do not change beyond shot to shot variation. For the case with the resonance excited, the non-scraped profile has larger tails in

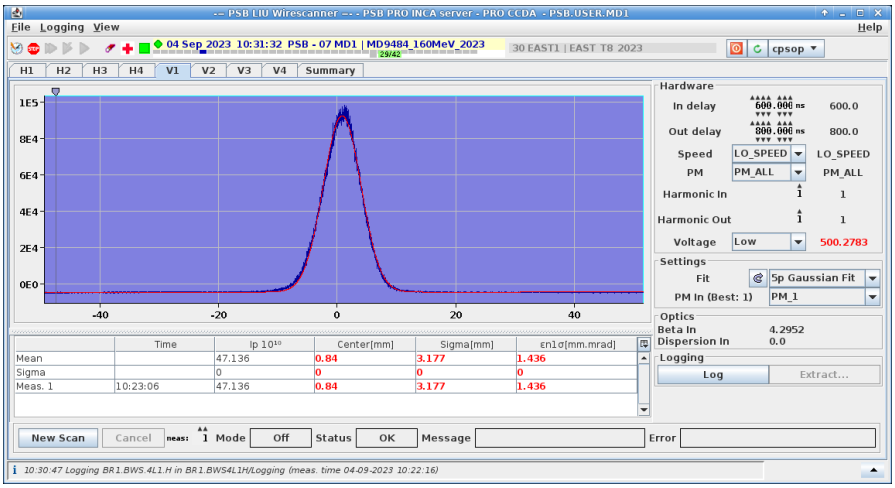

Figure 4.4: The initial vertical beam profile with corrected resonances and no excitation.

both H and V. As the vertical tails are removed by the scraper, both the horizontal and the longitudinal profile change shape. This suggests that particles which have been affected by the resonance have moved to high amplitudes in the vertical and horizontal planes, and a section of the distribution with large longitudinal amplitude is affected by the resonance. This is again compatible with space charge induced resonance crossing.

To see the effect of different levels of resonance excitation, the transverse profiles are fitted with a q-Gaussian distribution [41], [43], where the q-parameter shows how heavy ($q > 1$) or light tailed ($q < 1$) the distribution is compared to a normal Gaussian ($q = 1$). The bunch length is determined from the tomoscope data and represents the full width half maximum (FWHM) length of the bunch. The error given is for the standard deviation of the FWHM during the measurement of the tomoscope (100 profiles for one measurement). Figures 4.8, 4.9, 4.10 show the relative bunch lengths and the q-parameters of the transverse profiles (q_H for the horizontal fit and q_V for the vertical fit) for different sextupole currents exciting the $Q_x + 2Q_y = 13$ resonance, with the error from the covariance matrix of the fitting.

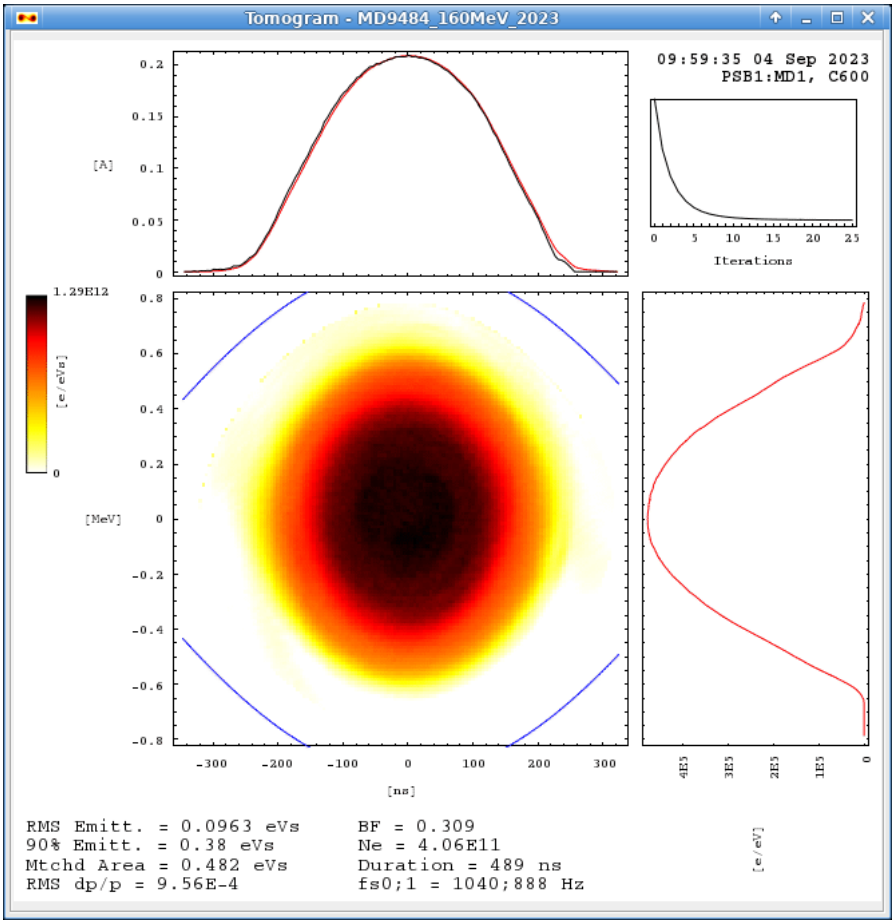

Figure 4.5: Tomographic reconstruction before any resonance excitation to make sure the longitudinal parameters were correct.

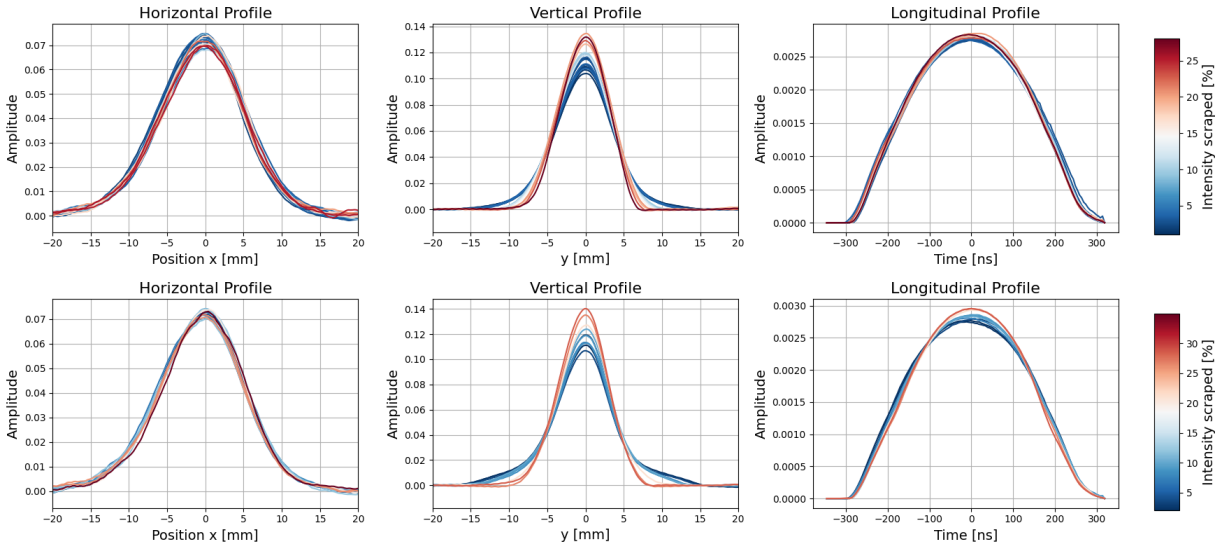

Figure 4.6: Beam profile measurements near the $3Q_y = 13$ vertical resonance. The measurements are after vertical scraping has removed different percentages of the bunch intensity as per the colour scale, without (top $I_{SX} = 0$ A) and with (bottom $I_{SX} = 40$ A) the resonance excited by a strongly powered skew sextupole for some period of the cycle.

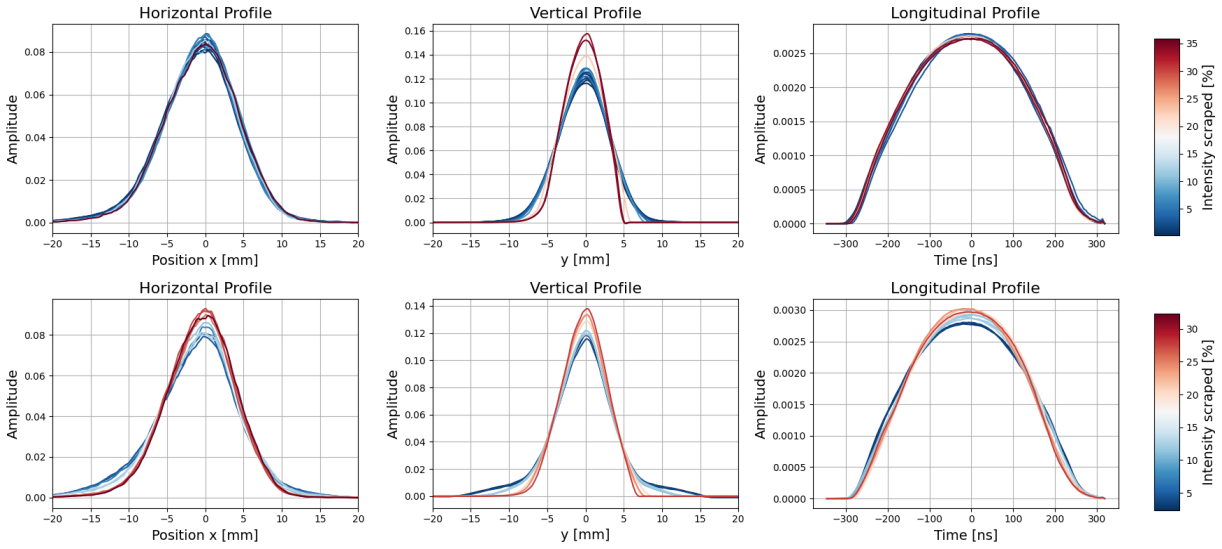

Figure 4.7: Beam profile measurements near the $Q_x + 2Q_y = 13$ coupled resonance. The measurements are after vertical scraping has removed different percentages of the bunch intensity as per the colour scale, without (top $I_{SX} = 0$ A) and with (bottom $I_{SX} = 40$ A) the resonance excited by a strongly powered normal sextupole for some period of the cycle.

In the case of $I_{SX} = 0$ A, it can be seen there is almost no dependence of q_H and bunch length on q_V (as the beam is scraped in the vertical plane), meaning little or no other coupling or resonant effects are present. For $I_{SX} = 20$ A, there are tails created in H and V, and they are correlated up to a scraping of 15%, along with the longitudinal bunch length. For $I_{SX} = 40$ A, the

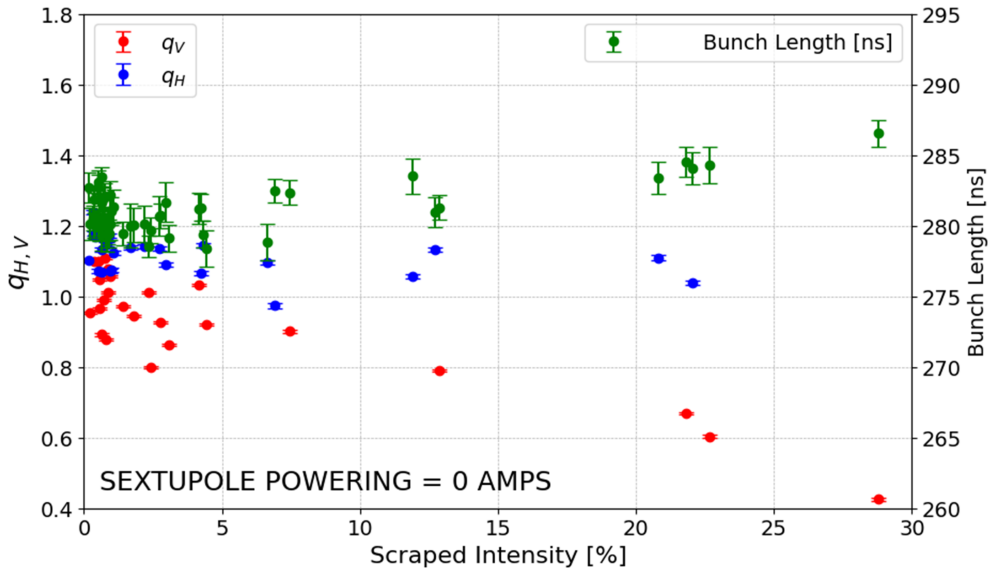

Figure 4.8: Bunch length, q_V and q_H plotted as a function of the scraped intensity for the $Q_x + 2Q_y = 13$ configuration. $I_{SX} = 0$ A.

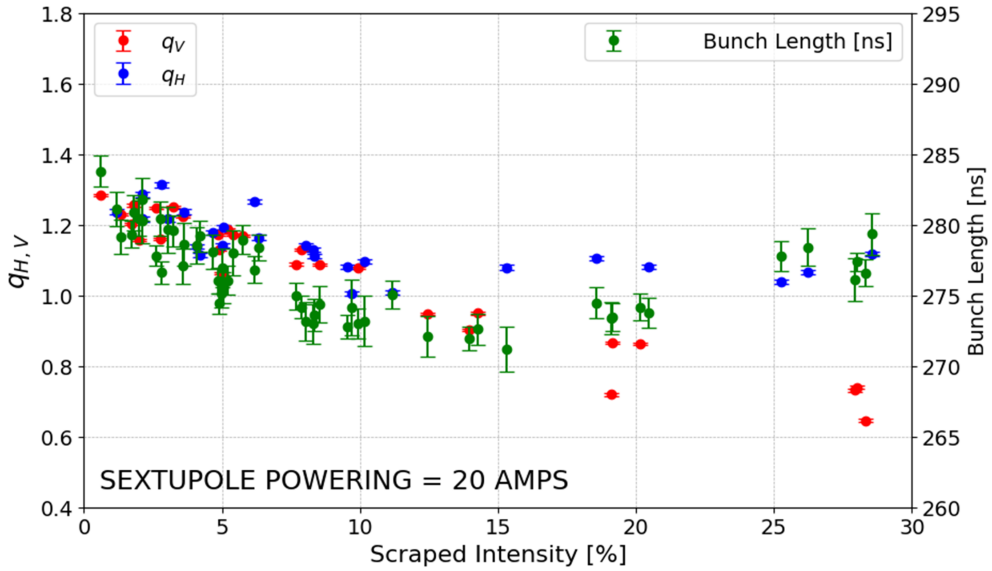

Figure 4.9: Bunch length, q_V and q_H plotted as a function of the scraped intensity for the $Q_x + 2Q_y = 13$ configuration. $I_{SX} = 20$ A.

tails generated by the periodic resonance crossing are even thicker and the three parameters remain correlated until a vertical scraping of 22%. Increasing the sextupole current and thus resonance excitation increases the non-factorization in the 6D phase space distribution.

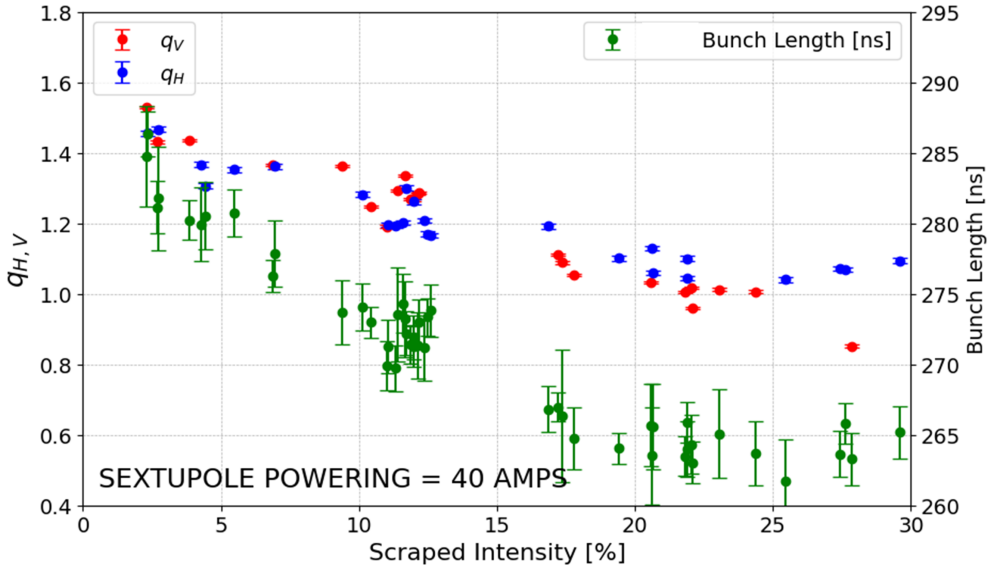

Figure 4.10: Bunch length, q_V and q_H plotted as a function of the scraped intensity for the $Q_x + 2Q_y = 13$ configuration. $I_{SX} = 40$ A.

4.4 Summary

The experimental results presented in this chapter show how periodic resonance crossing of a coupled resonance can build up non-factorization in a distribution which remains after the excitation of the resonance is removed ($I_{SX} = 0$). Depending on the strength of the excitation, the distribution becomes more or less factorizable. The non-factorization is higher for high amplitude particles and the particles in the core seem to still have a factorizable distribution, which is observable by the saturation of the change in the x plane at certain y apertures. In the case of 1D resonances, a transverse non-factorization is not introduced.

Simulations with symplectic tracking codes, described in the next chapter, will benchmark these results and offer more insight into the mechanism of the halo creation and the non-factorization of the amplitudes in the transverse planes.

5 Simulation of Coupled Resonance Crossing in the CERN PSB

5.1 Introduction

The experiment described in the Chapter 4 is simulated for the case of the coupled resonance excitation, namely $Q_x + 2Q_y = 13$, on a 160 MeV constant energy magnetic cycle in the Proton Synchrotron Booster (PSB). Two approaches are used, a shorter simulation to investigate the single particle dynamics, using a frozen space charge model (assumes Gaussian bunch shape). Then, for the collective behaviour, or the distribution evolution, long term tracking simulations are used with many macroparticles to benchmark the experiment. In this second case, a particle-in-cell space charge model (Poisson solver), is used in combination with a symplectic tracking code, both implemented in Xsuite [56], a modular simulation package for accelerator physics developed at CERN.

5.2 Single Particle Tracking

The first step was to simulate a few turns and particles under the so-called 'frozen' space charge hypothesis. The positions of the particles for all turns of the simulation were saved. We can inspect the phase space dynamics and tune diffusion. The short term tracking simulations are based on code from [57]. For the single particle dynamics, the simulation was as close to the experimental parameters as possible, the simulation parameters are given in Table 5.1.

An initial particle distribution of 1200 particles was used, with a polar grid in the $\hat{x}-\hat{y}$ plane and a longitudinal slice, that is, all particles are initiated on a $z = z_{\max}$ and the initial momentum offset $\frac{\Delta p}{p}$ is set to 0. Figure 5.1 shows the initial distribution in (linear) normalised $\hat{x}-\hat{y}$ space. Figure 5.2 shows how z and $\frac{\Delta p}{p}$ vary with synchrotron motion in the longitudinal phase space.

As only a longitudinal slice is used for the 1200 particles, depending on the $z_{\max}$ value the line density and thus the space charge forces vary. Assuming a Gaussian (approximation) profile in the z-direction, the space charge depends on the line density, given by,

Table 5.1: Simulation Parameters

Initial beam parameters	Value
Number of particles per bunch [10^{11} p]	4.06
Normalised RMS emittance [ϵ_x,ϵ_y] μmrad	[2.1, 1.4]
RF voltage [kV]	8
RMS $\frac{\Delta p}{p}$	9.56e-4
RMS bunch length (σ_z)	127 ns
FWHM bunch length	285 ns
Programmed tune*[Q_x, Q_y]	[4.18, 4.44]
Chromaticity **	[-3.7, -6.9]
Kinetic energy	160 MeV
Normal sextupole current I_{SX}	40 A

* The experimental set tunes Q_x and Q_y are varied in simulation to account for possible coherent tune shift due to impedance.

** The chromaticity is defined as the variation of the betatron tune Q momentum deviation $Q' = \frac{dQ}{d\delta}$ [58].

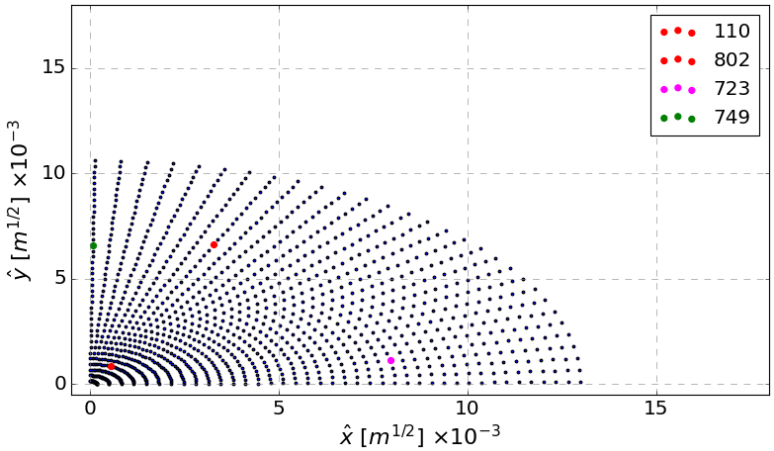

Figure 5.1: Initial $\hat{x} - \hat{y}$ position of 1200 particles for the short term simulation in the linear normalised $\hat{x} - \hat{y}$ space. The particles for which the dynamics is inspected more closely are numbered.

$$\lambda(z) = \frac{N_b}{\sqrt{2\pi\sigma_s^2}} e^{-\frac{z^2}{2\sigma_s^2}}, \tag{5.1}$$

where N_b is the bunch intensity, σ_s the longitudinal beam size, and z the position. The peak line density dependence on $z_{\max}$ can be seen in Fig. 5.3. The line density depends on the position z, which, in the case of $z_{\max} = 0$ m, does not vary with the synchrotron motion. For large $z_{\max}$, the line density and thus space charge varies with the synchrotron motion, and

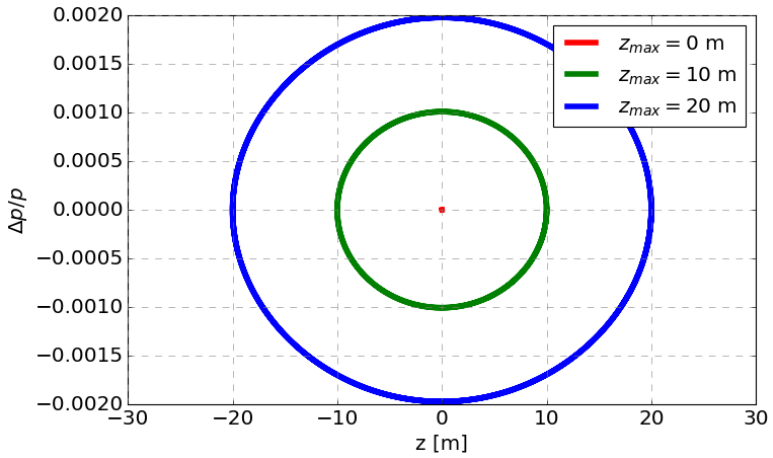

Figure 5.2: Longitudinal slice for short term tracking simulation and how the $\frac{\Delta p}{p}$ varies with z.

thus the detuning varies. This means that particles may periodically cross the resonance condition.

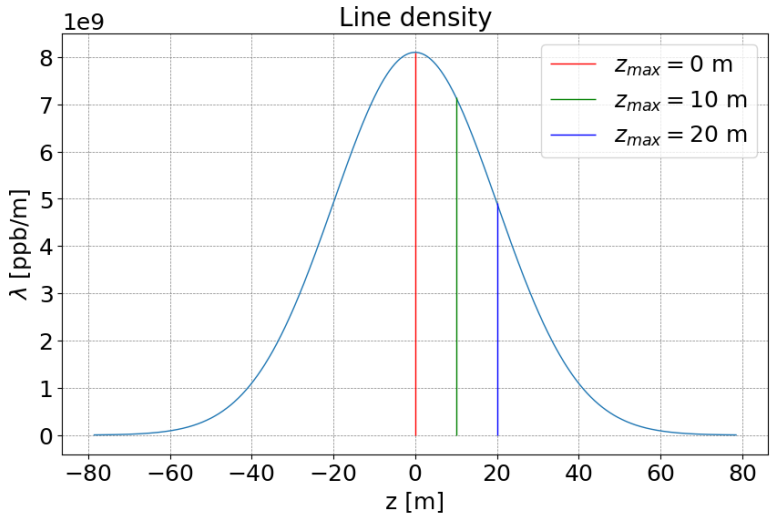

Figure 5.3: Line density λ indicating the slices of longitudinal phase space for different $z_{\max}$.

5.2.1 Tune Diffusion

To determine if the particles are affected by the $Q_x + 2Q_y = 13$ resonance excited by the normal sextupole in the lattice, a short tracking simulation and an analysis of the frequencies can be used in a technique known as frequency map analysis (FMA). Particles are simulated using Xsuite with the frozen space charge model for two synchrotron periods. For different slices of the longitudinal phase space ($z_{\max}$), the synchrotron period differs but can be calculated by observing the periodicity of the z parameter as seen in Fig. 5.4.

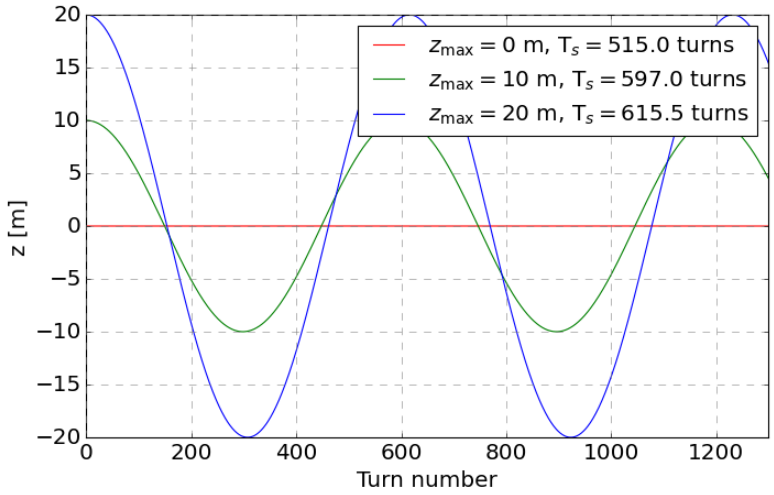

Figure 5.4: The z position for particles with the same initial transverse amplitude but different $z_{\max}$, yielding different synchrotron periods, τ_s.

The individual particle tunes for each synchrotron period are calculated using the NAFF algorithm [59], implemented in the Python module NAFFlib [60]. A tune diffusion 'coefficient' can be calculated using the formula,

$$d = \ln \sqrt{\left(Q_x^{(2)} - Q_x^{(1)}\right)^2 + \left(Q_y^{(2)} - Q_y^{(1)}\right)^2}, \tag{5.2}$$

where $Q_{x,y}^{(1)}$ are the horizontal and vertical tunes over the first synchrotron period, and $Q_{x,y}^{(2)}$ are the tunes over the second synchrotron period. For the calculation of the tune diffusion coefficient d, it is important to have a full synchrotron period when considering non-zero chromaticity, (the chromaticity in the experiment could not be corrected for simultaneously in both the x and y planes). This is not equivalent to defining a constant for diffusion in a diffusion equation, and is merely an observable of how the tune is changing in time.

The diffusion coefficient indicates how much the tune has changed over the two periods. The resonance can lead to a change in tune, due to the distortion in phase space [1]. Irregular or chaotic motion can be predicted with a large tune change in a short period [1].

It is useful to plot the particle's diffusion coefficient against its initial amplitude in the grid on the transverse plane, as shown in Figs. 5.5 and 5.6, for two simulations with different $z_{\max}$. We can observe a band that seems to be affected by the resonance. By plotting the particles tune in the resonance diagram it is possible to observe particles which are affected by the resonance, as they can become 'locked' to the resonance lines, Figs. 5.7 and 5.8.

In the case of the simulation with the longitudinal slice at $z_{\max} = 0$ m, there are fewer particles with large diffusion coefficients. For $z_{\max} = 10$ m, many more particles have large diffusion

coefficients. This is due to the periodic change in longitudinal line density, which allows particles to periodically cross the resonant condition as the space charge detuning changes. This suggests a dependence on whether a particle will reach higher amplitudes in the transverse plane depending on its longitudinal position, as observed in the experiment (see Chapter 4).

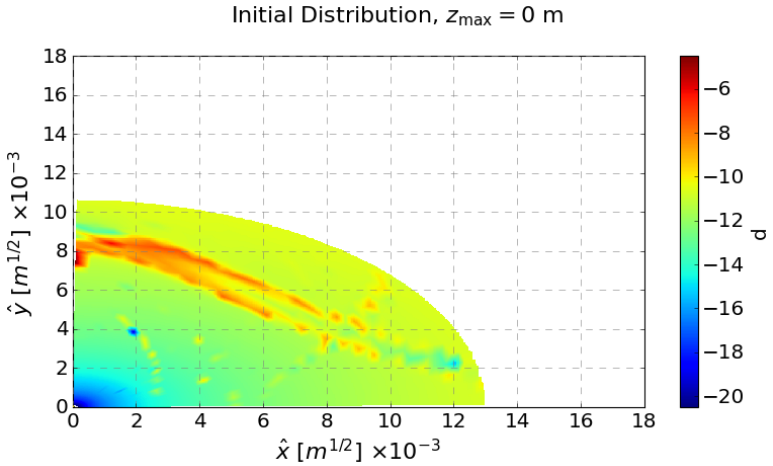

Figure 5.5: Initial distribution for particles on momentum, z_{max} = 0 m, plotted with their diffusion coefficient calculated for 2 successive synchrotron periods.

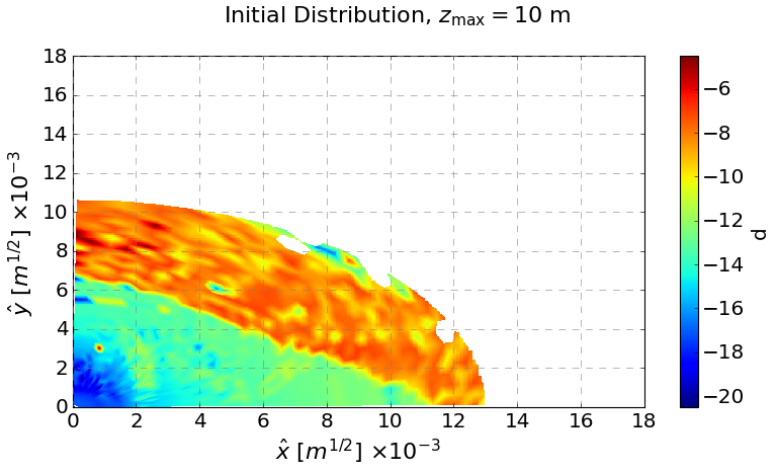

Figure 5.6: Initial distribution for particles off momentum, z_{max} = 10 m, plotted with their diffusion coefficient calculated for 2 successive synchrotron periods.

5.2.2 Single Particle Dynamics

It is possible to analyse the beam dynamics of the particle in the linear normalized space via a transformation. The Courant-Snyder (CS) invariants, J_x and J_y, can be tracked as a function of the turn in the synchrotron. In a symplectic and linear transformation, all linear combination of J_x and J_y are conserved. For the simulated case (non-linear), when the longitudinal slice

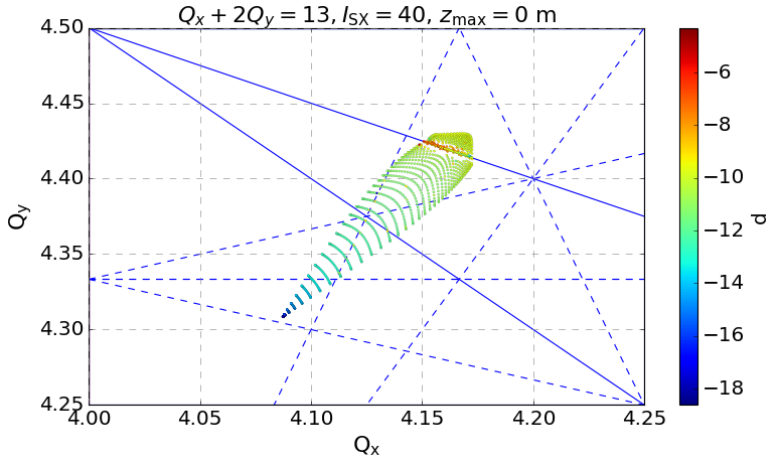

Figure 5.7: FMA for particles on momentum, $z_{max} = 0$ m, plotted in the tune diagram with their initial tune and diffusion coefficient calculated for 2 successive synchrotron periods.

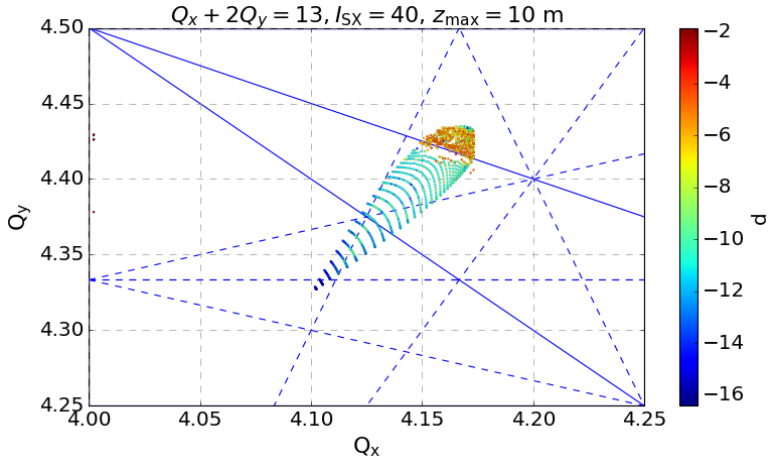

Figure 5.8: FMA for particles off momentum, $z_{max} = 10$ m, plotted in the tune diagram with their initial tune and diffusion coefficient calculated for 2 successive synchrotron periods.

is at $z_{max} = 0$ m, the evolution of $J_x + 2J_y$ ($n_x J_x + n_y J_y$), for a sample of particles, is plotted over 4000 turns in Fig. 5.9. n_x and n_y are the resonance coefficients. The non-linearities are sufficiently small that $J_x + 2J_y$ is almost preserved.

For the case of $z_{max} = 10$ m, the evolution of $J_x + 2J_y$ is plotted over 4000 turns in Fig. 5.10. There is a band of particles that are crossing the resonance condition, which is inferred from the large and irregular variation in $J_x + 2J_y$. The band of particles is seen when the linear combination $n_x J_x + n_y J_y$ is plotted, but not a coherent band for other linear combinations. The particles do not appear to be trapped in the resonance, as their amplitude does not increase indefinitely.

For the nominal RF bucket voltage and with the longitudinal slice at $z_{max} = 10$ m, we inspect

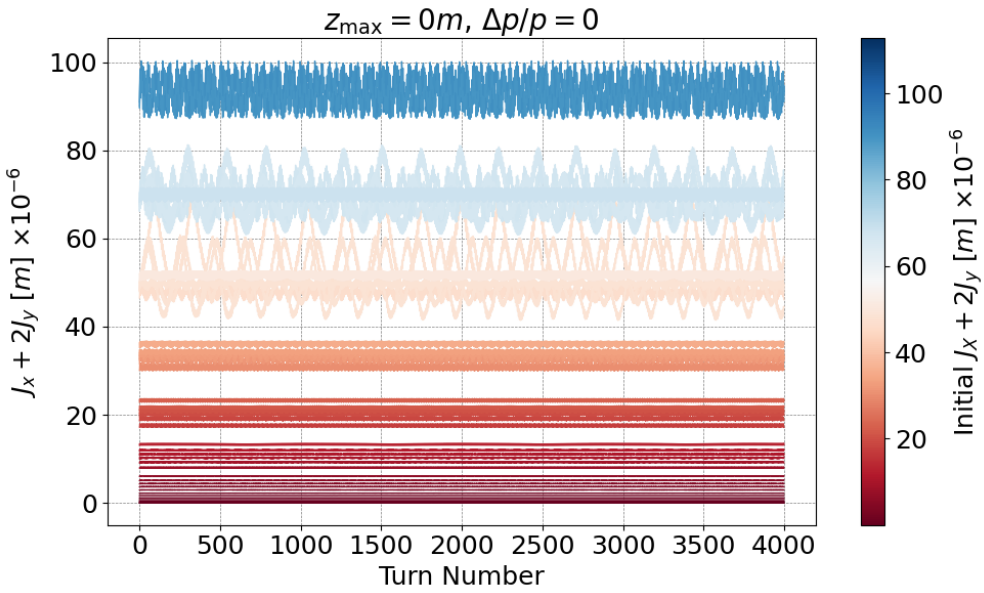

Figure 5.9: Simulation for particles on momentum, $z_{max} = 0$ m, showing over 4000 turns the $J_x + 2J_y$ evolution of a single particle colour-coded by its initial $J_x + 2J_y$.

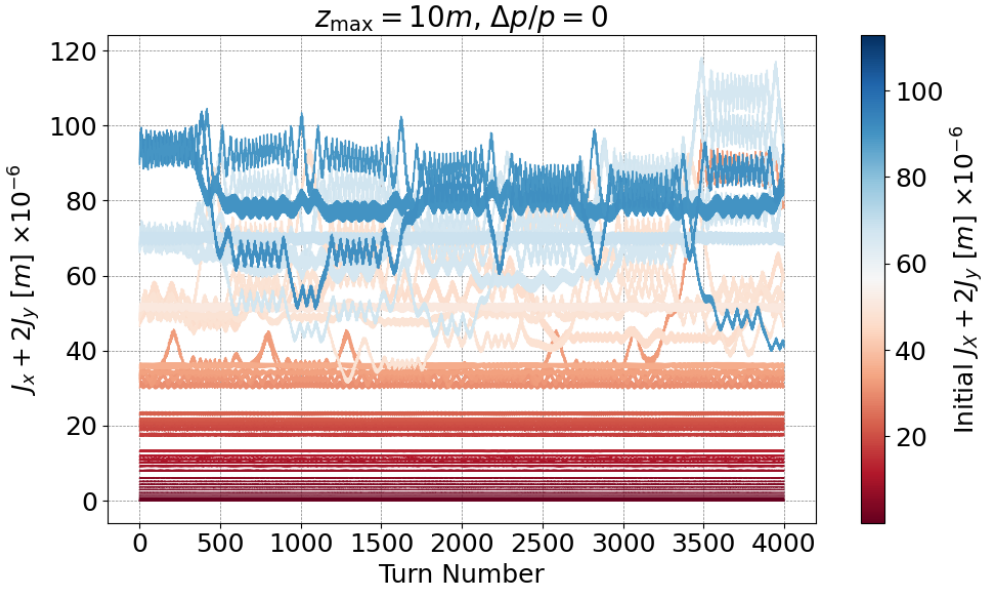

Figure 5.10: Simulation for particles off momentum, $z_{max} = 10$ m, showing over 4000 turns the $J_x + 2J_y$ evolution of the single particle colour coded it's initial $J_x + 2J_y$.

more closely an unaffected and a particle affected by the resonance. Figure 5.11 shows the evolution of the phase space $(\hat{x} - \hat{p_x}, \hat{y} - \hat{p_y})$ and the CS invariants, J_x and J_y, over 4000 turns for a particle that is not resonant (particle 110 in Fig. 5.1). The CS invariants oscillate (right) due to nonlinear elements in the lattice, such as space charge and the strongly powered normal sextupole. The $\hat{x} - \hat{p_x}$ (left) and $\hat{y} - \hat{p_y}$ (middle) projections remain quite constant over 4000

turns. Figure 5.12 shows the $\hat{x} - \hat{y}$ projection for two 100-turn periods. The motion is not correlated in the $\hat{x} - \hat{y}$ planes.

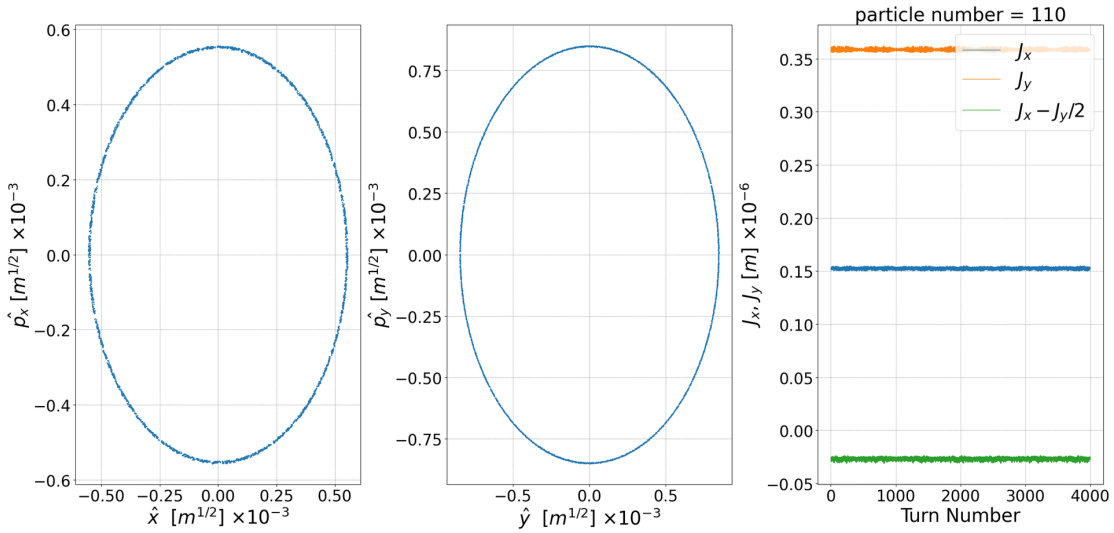

Figure 5.11: A non-resonant particle (110) and the evolution of the CS invariants (right) and the linearly normalised phase space projections $\hat{x} - \hat{p_x}$ (left), and $\hat{y} - \hat{p_y}$ (middle).

Figure 5.13 shows the evolution of J_x, J_y, and the $\hat{x} - \hat{p_x}$ and $\hat{y} - \hat{p_y}$ phase space of a particle that is repeatedly crossing the resonance condition but is not trapped (particle 802 in Fig. 5.1). The J_x and J_y (right) evolve, and the particle either gains or loses energy when the resonance condition is met. The quantity $J_x - J_y/2$ is plotted, corresponding to $J_x/n_x - J_y/n_y$, the 'first invariant of the perturbed motion' from [15] with prior work in [61]. $J_x - J_y/2$ remains constant (beyond oscillations due to the approximation of the linear normal form).

Figure 5.14 shows the same particle's $\hat{x} - \hat{y}$ projections for two different periods (top left and bottom left) at turns 300-400 and 950-1000. The top right shows the same evolution of J_x and J_y, but also the tunes Q_x and Q_y calculated with a moving window of 40 turns. The bottom right plot shows the synchrotron motion and the tunes. The particle follows structures in the $\hat{x} - \hat{y}$ plane rather than regular rectangular motion, as it is scattered to higher J_x and J_y (top right). These are 2D projections of a 6D structure. The change in J_x occurs simultaneously with the change in J_y, at a ratio of 1:2, linking the particle's $\hat{x}$ position to its $\hat{y}$ position. This is only single-particle dynamics, and we cannot yet see how this would change the full distribution and introduce non-factorization.

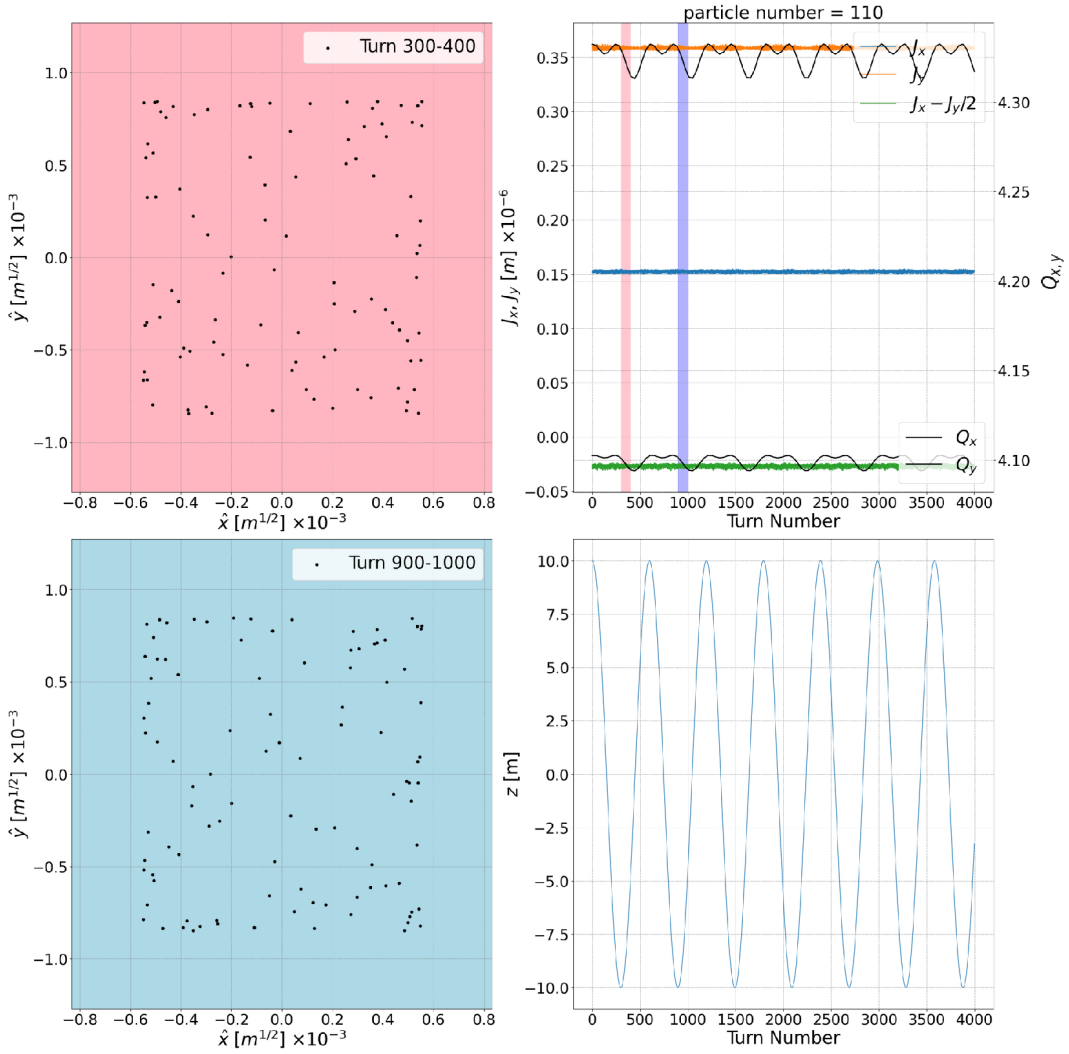

Figure 5.12: Projections on the $\hat{x} - \hat{y}$ plane (top left, bottom left) for the turn numbers 300-400 and 900-1000 out of 4000 for a non-resonant particle (position 110). The linear combination of the tune $n_x Q_x + n_y Q_y$, calculated over a 40 turn window is shown with the CS invariants and the $J_x/n_x - J_y/n_y$ [15], [61] (top right) for 4000 turns. The synchrotron motion is plotted (bottom right) for the same 4000 turns.

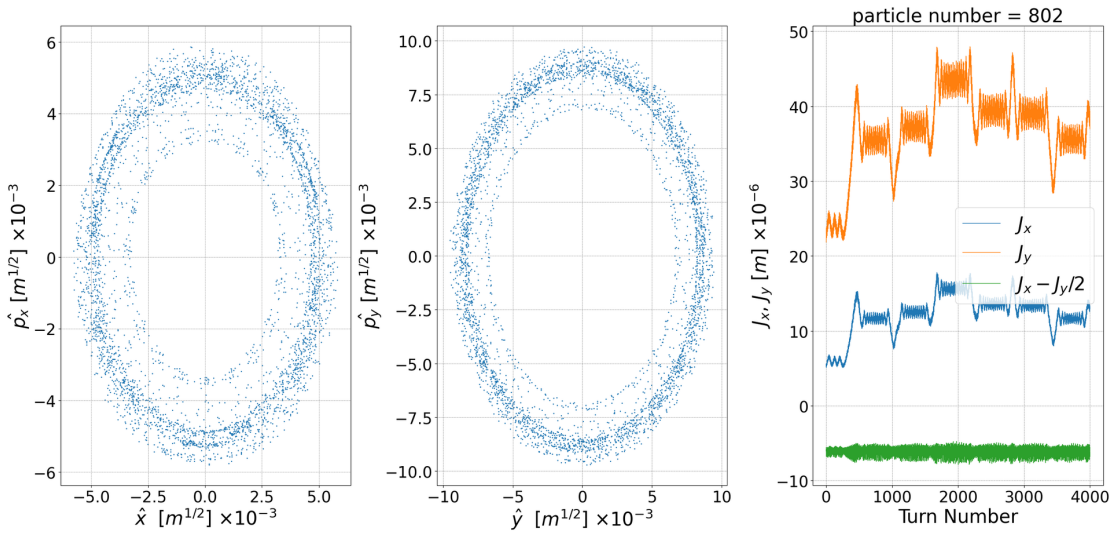

Figure 5.13: A resonant particle (802) and the evolution of the CS invariants (right) and the linearly normalised phase space projections $\hat{x} - \hat{p_x}$ (left), and $y - p_y$ (middle), as the resonance is repeatedly crossed.

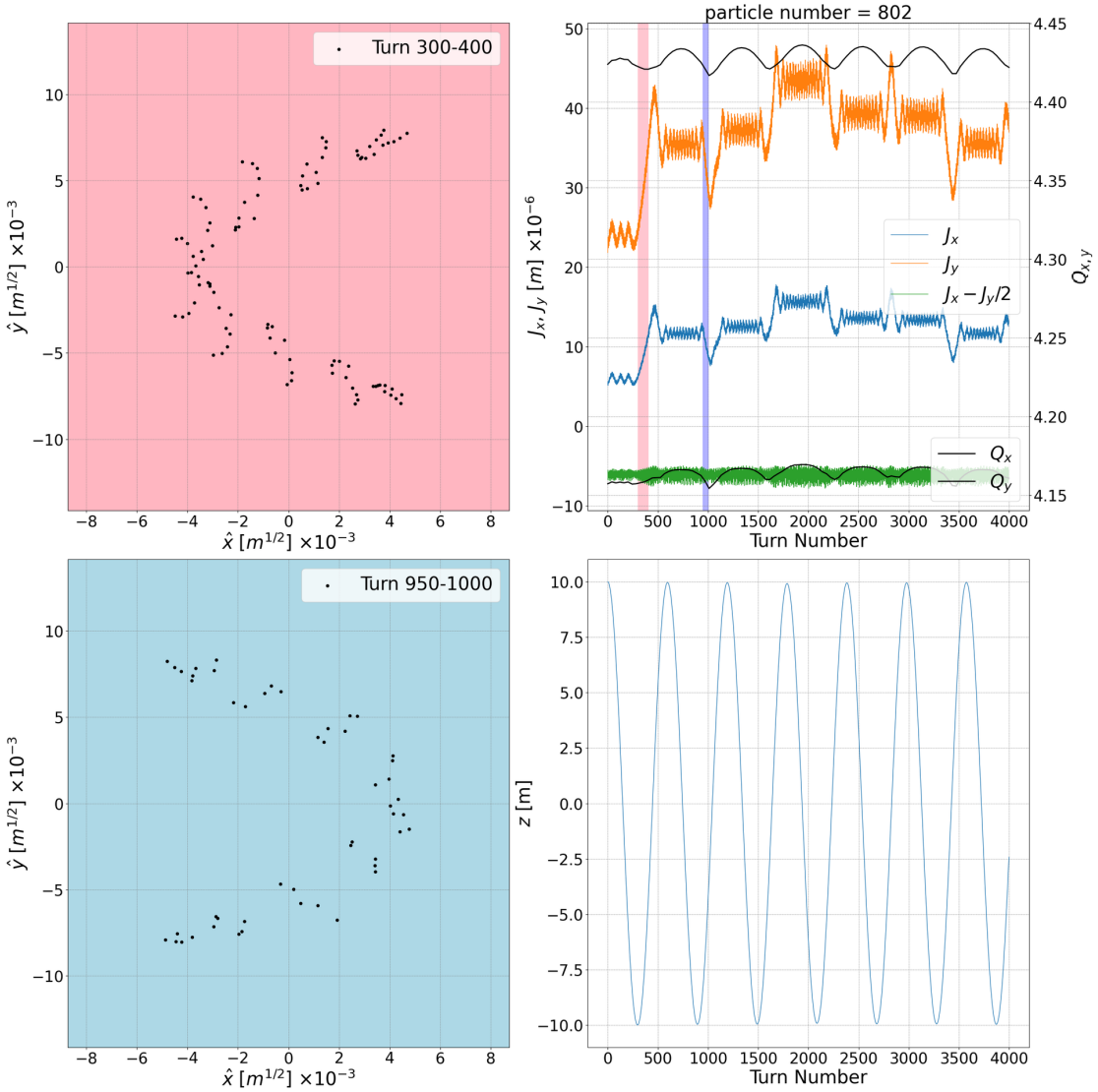

Figure 5.14: Projections on the $\hat{x} - \hat{y}$ plane (top left, bottom left) for the turn numbers 300-400 and 950-1000 out of 4000 for a resonant particle (position 802 in Fig. 5.1). The tune $n_x Q_x + n_y Q_y$ calculated over 40 turn windows is shown with the CS invariants and the $J_x/n_x - J_y/n_y$ [15] (top right) for 4000 turns. The synchrotron motion is plotted (bottom right) for the same 4000 turn period.

5.2.3 Trapping

The simulation was repeated with a lower RF bucket voltage (much lower than in the experiment) to increase the synchrotron period. This slows down the process of resonance crossing. A $z_{\max}$ of 40 m was used to create a larger variation in the longitudinal line density with the synchrotron motion. Figure 5.15 shows the $\hat{x} - \hat{p_x}$ and $\hat{y} - \hat{p_y}$ evolution over 20 000 turns, with a synchrotron period of approximately 18 000 turns. The CS invariants are plotted, and unlike the case of particle 802 from Fig. 5.14, the particle stays on the resonance condition for a longer period. The CS invariants gradually increase and then decrease back to the initial amplitude. The situation is much more nonlinear, and the 'invariant' for the perturbative case $J_x/n_x - J_y/n_y$ is not valid.

In Fig. 5.16, the particle's projection of $\hat{x} - \hat{y}$ phase space is plotted for different periods: turns 3000-6200 (top left) and 13 000-16 000 (bottom left). On the top right, the tunes are plotted with the CS invariants, and the bottom right shows the synchrotron motion and the tunes over 20 000 turns. The synchrotron period is much longer and is therefore almost considered 'frozen.' This allows for a slower crossing of the resonance condition, and the tunes become locked for a certain period (pink and blue sections). The $\hat{x} - \hat{y}$ projections now have a constant 'phase', but a varying amplitude in the structure as the CS invariants increase and then decrease. The reason for the constant phase of the structure, as opposed to the case in Fig. 5.14, could be interpreted as the quasi-freezing of the longitudinal motion. Thus, the 2D projection is a projection of a 4D object rather than a 6D object. By even further reducing the RF voltage, the shape of the fixed line can fully emerge due to a full trapping of the particle on the resonance, as seen in Figs. 5.17 and 5.18.

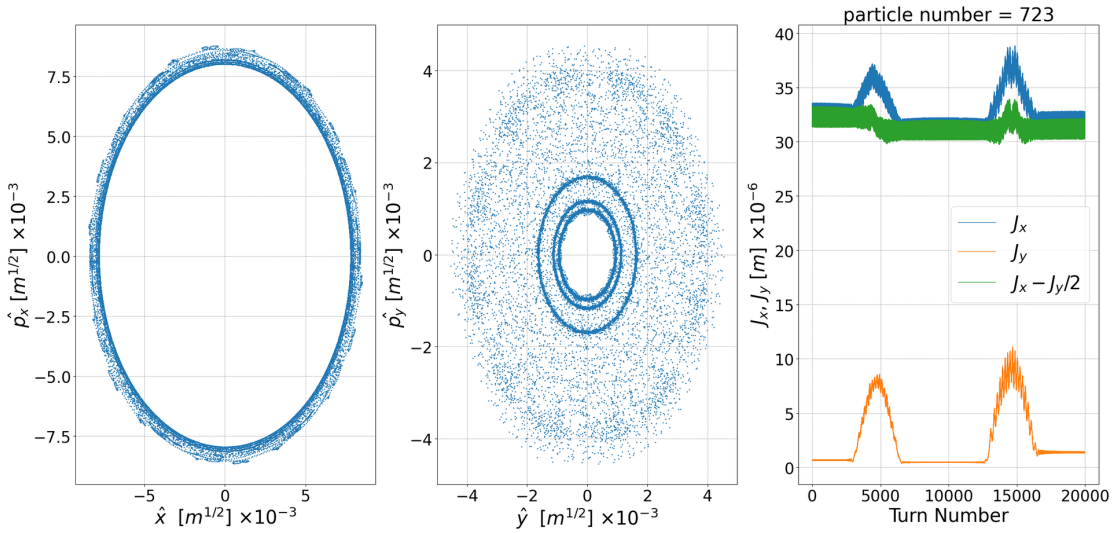

Figure 5.15: A resonant particle for a simulation with a much longer synchrotron period, the CS invariants (right) and the linearly normalised phase space projections $\hat{x} - \hat{p_x}$ (left), and $y - p_y$ (middle).

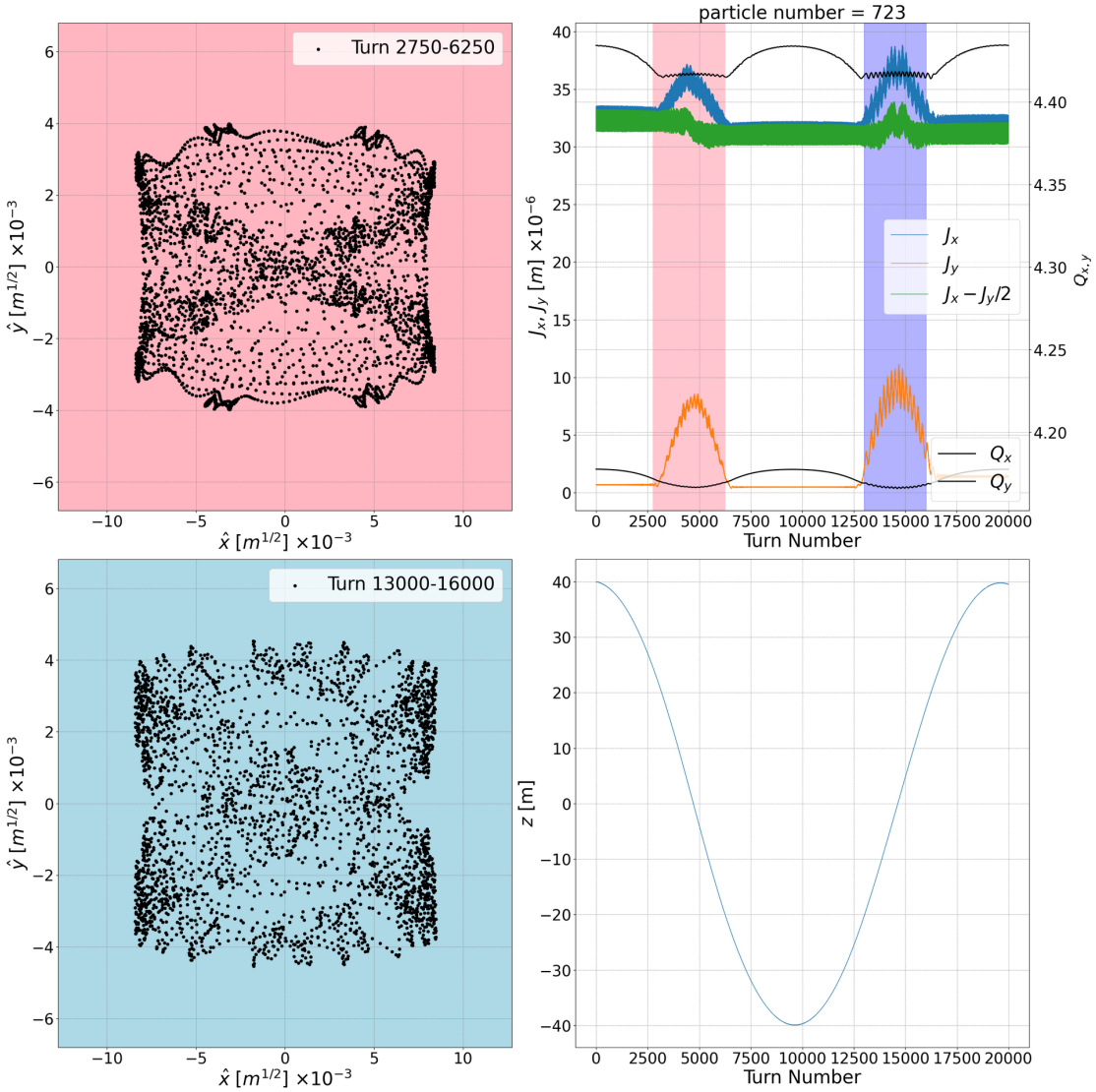

Figure 5.16: Projections on the $\hat{x} - \hat{y}$ plane (top left, bottom left) for the turn numbers 2750-6250 and 13000-16000 out of 20000 of a resonant particle which is trapped due to the longer synchrotron period and thus slower crossing of the resonance condition. The linear combination of the tune $n_x Q_x + n_y Q_y$ is shown with the CS invariants and the $J_x/n_x - J_y/n_y$ [15] (top right) for 20000 turns. The synchrotron motion is plotted (bottom right) for the same 20000 turn period.

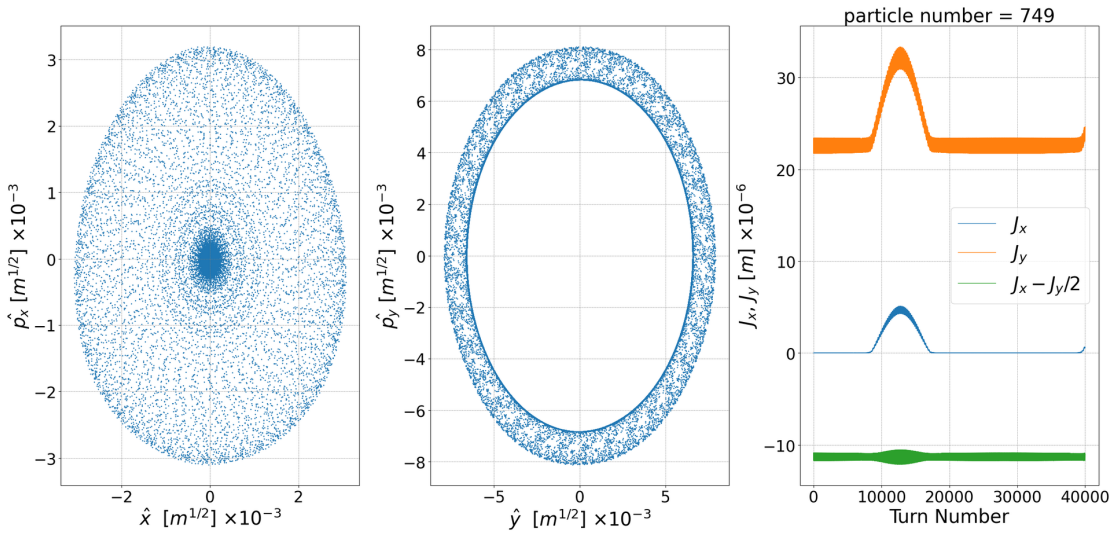

Figure 5.17: A resonant particle for a simulation with a much longer synchrotron period, the CS invariants (right) and the linearly normalised phase space projections $\hat{x} - \hat{p_x}$ (left), and $y - p_y$ (middle).

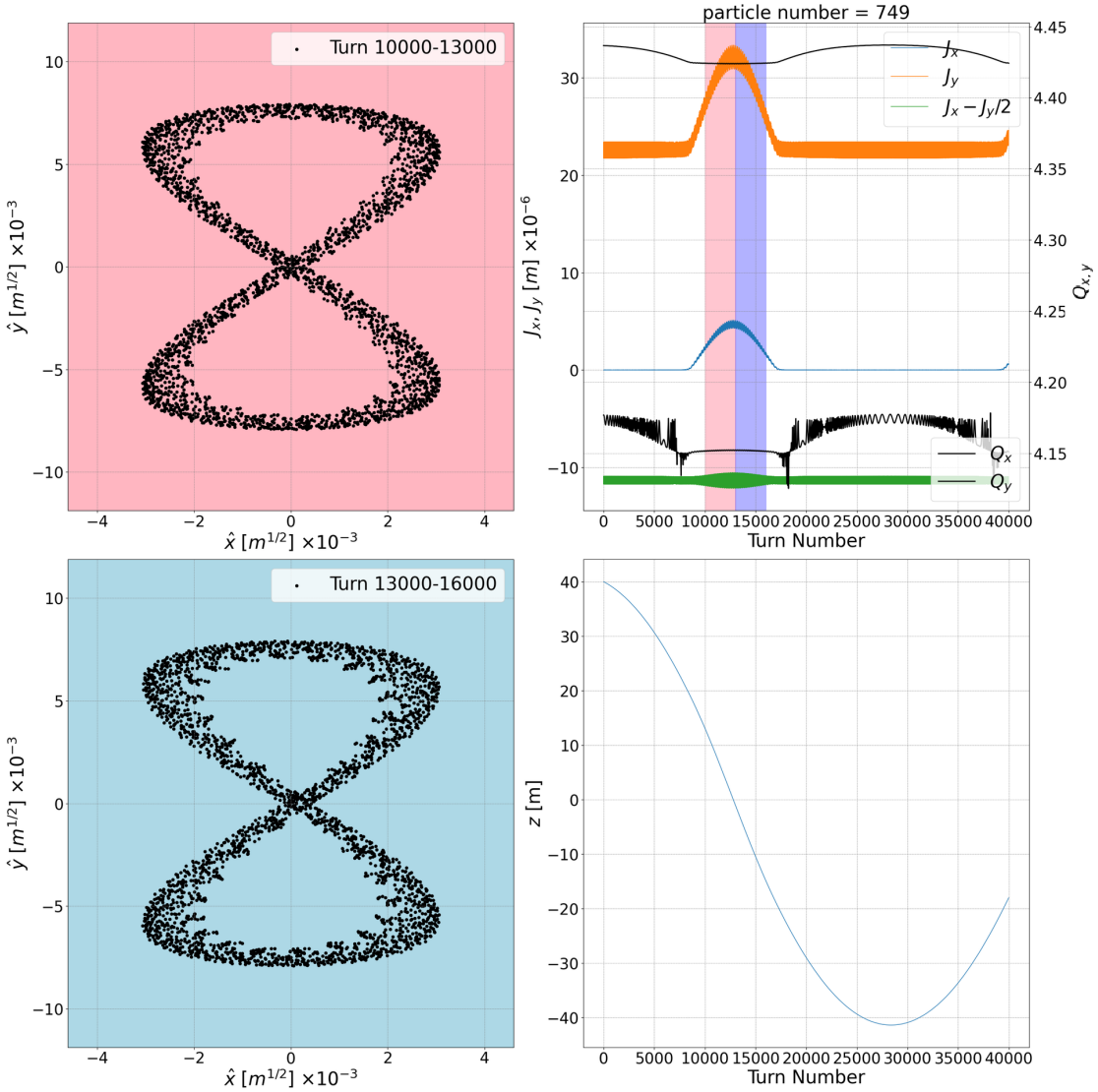

Figure 5.18: Projections on the $\hat{x} - \hat{y}$ plane (top left, bottom left) for the turn numbers 10 000-13 000 and 13 000-16 000 out of 40 000 of a resonant particle which is trapped due to the longer synchrotron period and thus slower crossing of the resonance condition. The linear combination of the tune $n_x Q_x + n_y Q_y$ is shown with the CS invariants and the $J_x/n_x - J_y/n_y$ [15] (top right) for 40 000 turns. The synchrotron motion is plotted (bottom right) for the same 40 000 turn period.

5.3 Multi-particle Tracking

By observing the single particle dynamics, we cannot observe the evolution of the whole distribution and the non-factorization (see Chapter 3). The non-factorization is a statistical property, thus the evolution of many particles is needed.

The PSB lattice is simulated at injection energy with parameters consistent with those in the experiment in Chapter 4 and detailed in Table 5.1. The number of macroparticles required was determined by convergence simulations, as shown in Fig. 5.19. It was found that 500 000 macroparticles were necessary to accurately reproduce the correct behaviour with space charge, as the profile distribution at 200 000 turns converged after this number of macroparticles.

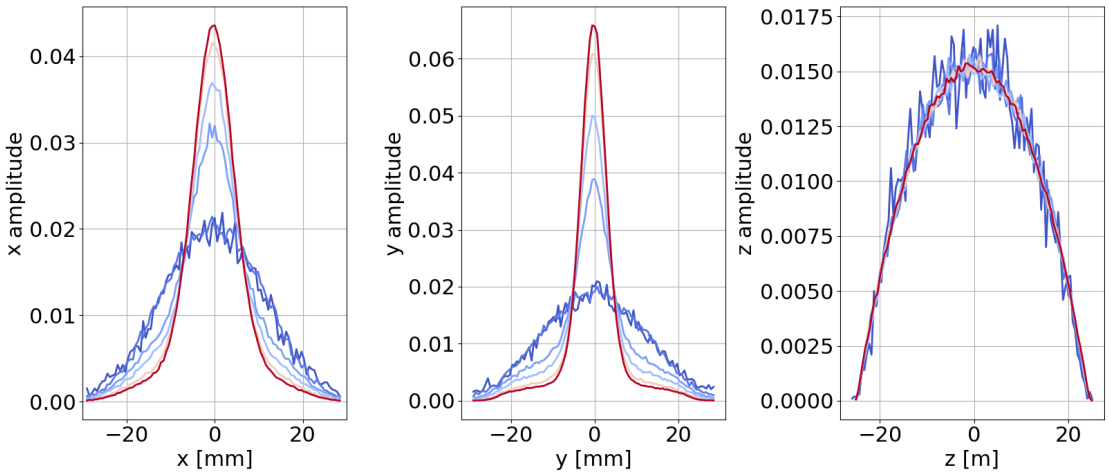

Figure 5.19: Convergence study for different macroparticle numbers. The beam profile is plotted after 2×10^5 turns in simulation, with PIC 2.5D space charge.

The initial transverse distribution used is a Gaussian distribution with the measured normalized emittances of, $\epsilon_x = 2.1\,\mu$mrad, $\epsilon_y = 1.4\,\mu$mrad. The longitudinal distribution is parabolic. The distribution is injected and matched to the lattice. The working point, or tune, is set to be the same as the experiment. The excitation of the resonance is with a normal sextupole set to a current of $I_{SX} = 40$ A. The distribution is tracked using the symplectic tracking code Xtrack, part of Xsuite, which includes a 2.5D FFT particle-in-cell solver to calculate the space charge. The space charge forces and kicks are calculated by solving the Poisson equation. The '2.5D' refers to the fact that the longitudinal distribution is sliced, and space charge is then solved using a 2D model. The distribution is tracked for 230 000 turns, consistent with the resonance excitation period of the experiment. The simulation is based on code from [62].

5.3.1 Tune dependence

Initial simulations found a small discrepancy between the simulated halo growth and the halo observed in the experiment at 230 000 turns. Tune scans around the machine's set tune showed better agreement, which could be due to a coherent tune shift caused by the impedance of the ring [63], which is neglected in the simulation.

The long-term tracking simulations, with an offset tune compared to the experiment, reproduce the general behaviour of the beam distribution very well. Figure 5.20 shows the final profile from simulations after 230 000 turns, (red) compared with the profiles measured with the wire scanner and tomograph in the longitudinal plane (blue). The simulation results include an aperture in the y plane, consistent with the aperture caused by the scraper in the experiment. When the simulation tunes are set at $Q_x = 4.18$, $Q_y = 4.435$, with a ΔQ_y of -0.005 compared to the experimental tune, the final profiles in y are closest to the observed experimental profile, Fig. 5.20. Figure 5.21 is from a simulation with a slightly lower vertical tune, $Q_y = 4.430$, and it can be seen the profile in y does not agree as well.

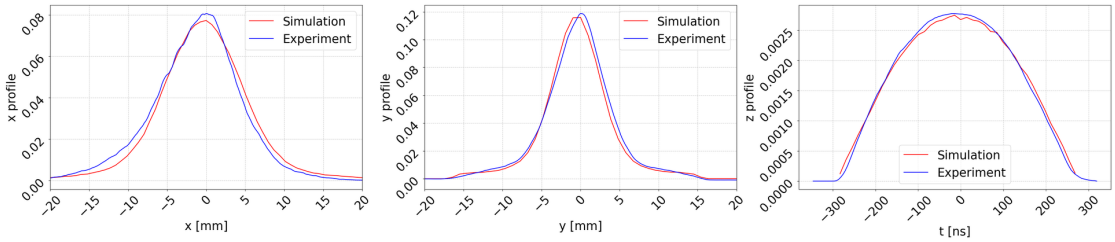

Figure 5.20: Comparison of the simulated and measured distribution after the resonance excitation for 230k turns. The set tune was $Q_x = 4.18$, $Q_y = 4.435$.

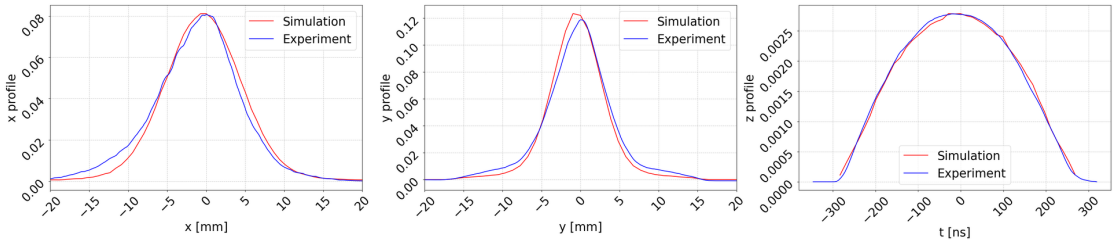

Figure 5.21: Comparison of the simulated and measured distribution after the resonance excitation for 230k turns. The set tune was $Q_x = 4.18$, $Q_y = 4.43$.

5.3.2 Non-Factorization in Simulation

To determine if non-factorization is present in the distribution, a series of simulated vertical apertures are used to remove the tail part of the distribution, and the change in the profile in the horizontal plane is observed, as was done in experiment. Figure 5.22 shows the profiles in the three planes, for different y apertures, given by the colour code. The y-aperture is introduced by a condition on y and p_y. As the aperture moves towards the centre of the bunch, the y plane shows the tails removed, and in the x plane the tails are also reduced, however less than in the experiment. The longitudinal plane is also changing, consistent with the experimental results.

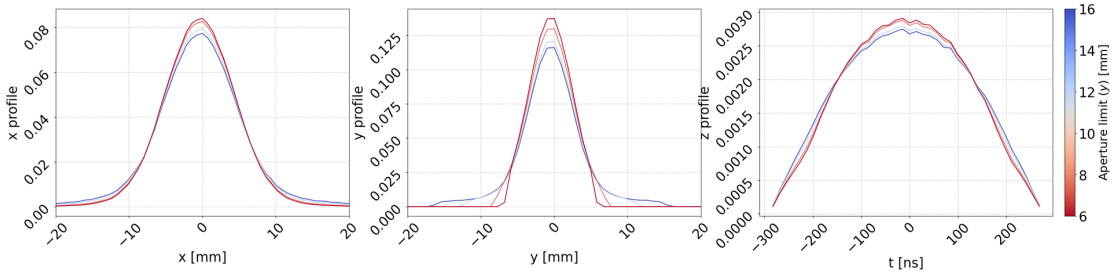

Figure 5.22: Change in profile in x, y, z for different y apertures given by the colour code. A change in profile in the other planes apart from y demonstrates a non-factorization in the distribution. The tune was set at $Q_x = 4.18$, $Q_y = 4.435$ and the emittance the nominal.

5.3.3 Dependence on Initial Emittance

Depending on the initial emittance of the x and y planes, the halo evolution differs. The results of a simulation with a horizontal normalized emittance of 2 μmrad and a vertical normalized emittance of 3 μmrad are shown in Fig.5.23. All other parameters are kept the same as in the previous simulation, shown in Fig.5.22 which matches the experimental data. The final profile is shown with different y apertures and how the profile changes in the other planes. The change in the x plane is stronger than for the experiment in chapter 4. By changing the emittances, the non-factorization can be increased with the excitation of the coupled resonance.

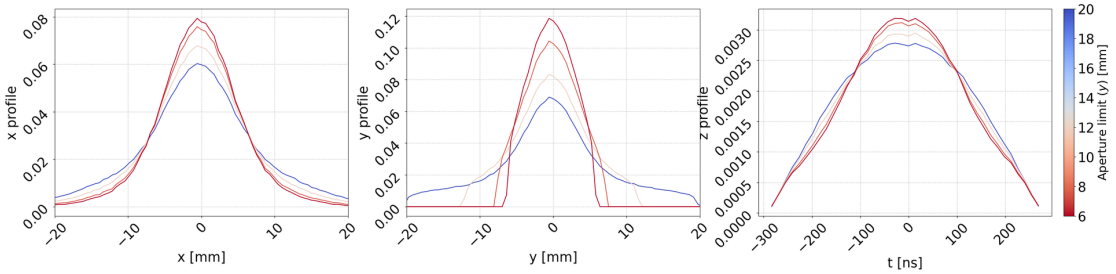

Figure 5.23: Change in profile in x, y, z for different y apertures given by the colour code. A change in profile in the other planes apart from y demonstrates a non-factorization in the distribution. The tune was set at $Q_x = 4.18$, $Q_y = 4.435$ and the emittances $2\,\mu$mrad (x) and $3\,\mu$mrad (y).

5.4 Summary

Through simulation of the single particle dynamics, it has been shown that crossing of a resonance condition periodically can lead to a change in the CS invariant in both the x and y plane if the resonance is a coupling one. Particular longitudinal slices are likely to have more particles which cross the resonance condition. Simulating a much longer synchrotron period than the experiment, leads to a full trapping of the particle, with the tune constant. The 'fixed-line' structures emerge in the $x-y$ plane.

Long term tracking simulations with many macroparticles and PIC space charge agree well with the experiment in Chapter 4, taking into account a small set tune offset. The non-factorization is introduced via the periodic crossing, as the initial distribution is a transverse factorizable Gaussian.

Exploring the parameter space, shows that changing the emittances in the two transverse planes changes the dynamics and affects the level of non-factorization when subject to the same resonance and lattice. This experience was used in another experiment to maximise the non-factorization present in a distribution in order to measure how it is transferred from one accelerator to another in a chain, as discussed in Chapter 6.

6 Non-Factorization Transport along the CERN Accelerator Complex

6.1 Introduction

The Chapters 4 and 5 demonstrate how non-factorization (NF) can be introduced into the $x-y$ beam distribution through the periodic crossing of coupled resonances, and that this non-factorization can be observed in experiments through beam scraping (collimation), and profile measurements.

At the Large Hadron Collider (LHC), NF has been observed in the beam distribution through van der Meer scans (vdM). Moreover, the NF of the transverse distribution was the largest uncertainty in the luminosity calibration, as cited by CMS in the analysis of the 2023 van der Meer run [32]. An experiment was proposed to determine if NF from periodic resonance crossing is transferred from a lower energy accelerator in the chain up to the LHC. This proposal was partly motivated by the observation that the NF correction exhibited a particular pattern where every 4th bunch in the filling scheme (pattern of bunches injected to the LHC) had a lower NF correction, which could point to a source from the Proton Synchrotron Booster (PSB), which has 4 rings [33]. Magnet imperfections (driving coupled resonances), which differ from ring to ring, could be a possible explanation for this observation, as the intensity is uniform in each ring (space charge driven). This observation coincided with the PSB experiments on NF introduced by coupled resonance crossing, leading to the idea that this phenomenon (not artificially excited) could contribute to the NF observed during the vdM scans.

In previous years, schemes for the van der Meer bunches did not avoid coupled resonances. Van der Meer bunches are the bunches used in van der Meer scans, which have a special configuration in order to produce the desired emittance and intensity at the LHC. A previous vdM scheme made use of integer resonances to blow up the bunch emittance, and then exchange the emittance to both transverse planes using the 4th order Montague resonance [64], [65] until the required parameters were reached [66]. The 4th order Montague resonance is a coupling resonance, $2Q_x - 2Q_y = 0$, and is known to cause emittance exchange [64]. Dynamics due to this resonance could also cause non-factorizable distributions, as shown by

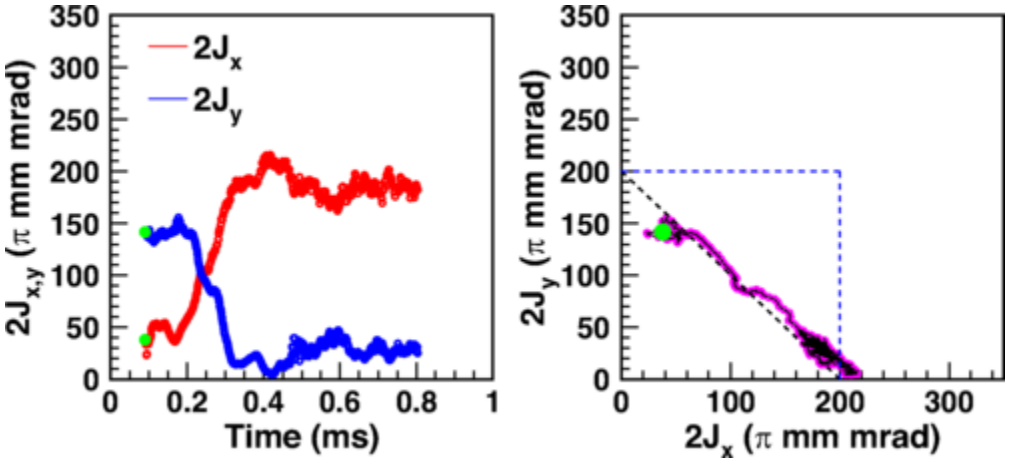

Figure 6.1: Single particle invariants can be anti-correlated through the dynamics of the Montague resonance $2Q_x - 2Q_y = 0$ [65].

the anti-correlated J_x, J_y for a single particle in [65], shown in Fig. 6.1.

An experimental campaign was proposed, to see how non-factorization from lower energy machines (purposefully introduced into the bunch), is transported to higher energy machines. The goals of the experimental campaign were as follows:

- Is NF or factorization of bunches preserved along the CERN injector chain?
- Is NF observable with scraping measurements in the SPS and LHC?
- Could contributions from the CERN injectors be important for the NF observed in van der Meer scans?

6.2 Experiments in the SPS

The CERN proton accelerator chain consists of the LINAC4, Proton Synchrotron Booster (PSB), Proton Synchrotron (PS), Super Proton Synchrotron (SPS), and the Large Hadron Collider (LHC), with increasing momentum for the proton bunches at each stage. To determine if the non-factorization (NF) introduced into the bunch is transferred from the PSB downstream to the LHC, the bunch was first measured in the SPS using scraping. The SPS is the next machine equipped with a scraping or collimation system after the PSB.

6.2.1 Beam Variants

Different bunches with varying degrees of non-factorizability were tested. There were requirements on the emittance and intensity of the bunches in order for their use in van der Meer scans in subsequent experiments. The required intensity was $\sim 1 \times 10^{11}$ ppb and the required

emittances were 2.5-3.5 μmrad. The bunches differed in their preparation schemes within the PSB. The two main types are detailed below:

Type A: Coupled Resonance (Non-Factorizable)

A higher-than-desired intensity is injected from LINAC4. Beam tails are removed by initial scraping upon injection into the PSB from LINAC4. The 3rd order coupling resonance $Q_x + 2Q_y = 13$ is excited using a normal sextupole during the ramping (accelerating) part of the cycle. The space charge tune spread is getting smaller as the energy is increased with the ramp. Thus, the tunes of the PSB must be set sufficiently close to the resonance such that during the tune spread evolution the distribution continues to be affected. The bunch is then transferred to the PS and SPS, with efforts made to minimize injection oscillations.

Type B: Van der Meer missteer (Factorizable)

To avoid resonances, the set tune in the PSB and amplitude dependent tune spread due to space charge were in a resonance free region of the working point diagram, up to 4th order, as shown in Fig. 6.2. Upon injection to the PSB, approximately 30% of the total intensity was removed in the to eliminate higher amplitude particles coming from the LINAC4 (linear accelerator). On injection to the PSB, the required emittance was achieved with missteering and blow up through a foil. Injection missteering is the process of injecting the beam with an error in position with respect to the design orbit, resulting in a filamentation which causes emittance growth [67], [68].

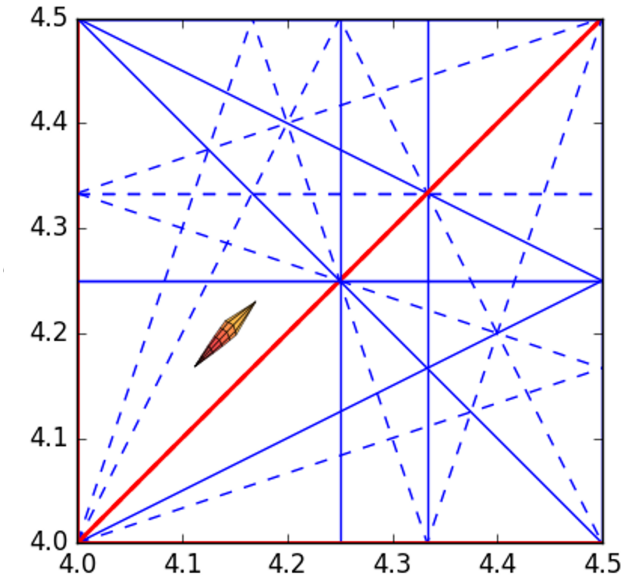

Figure 6.2: Working point diagram with the estimation of the tune spread from space charge for the A, 'vdM missteer' bunch in the PSB at injection energy (160 Mev). The tune spread was calculated with [54].

6.2.2 Observations

The extended flat bottom period—prolonged to accommodate multiple injections from the PS modified the beam distribution as detected by the SPS scraper. The extended flat bottom appeared to couple the two planes, resulting in the exchange of emittances. To mitigate these effects, the following measures were implemented:

1. Adjusting the tune away from the coupling resonance in both the horizontal and vertical planes.
2. Reducing the flat bottom duration by using cycles designed for single injections rather than multiple.

6.2.3 Results of Scraping in the SPS

The results of vertical scraping for two different bunch types, type A, 'coupled resonance' and type B, 'vdM missteer', are shown in Figs. 6.3 and 6.4. The figures illustrate how the fitted q-parameter of a q-Gaussian of the beam profile, after increasing removal of intensity by vertical scraping, changes in both the vertical and horizontal planes. For the 'coupled resonance' bunch, which in the PSB was subjected to strong excitation of a resonance leading to a distribution where high-amplitude particles in x are more likely to also have high amplitudes in y, we observe that the non-factorization is at least partially maintained. At the point of scraping in the SPS, the beam encounters an almost linear lattice, with the absence of significant coupling. However, the removal of high-amplitude particles in the y plane leads to a change in the distribution in x, specifically a decreasing q-parameter in x.

For the B type bunch, which is optimized to be as factorizable as possible, the q-parameter remains stable in the horizontal plane as the vertical plane is scraped, while the vertical q-parameter decreases. The only difference between the two distributions is their preparation in the PSB, demonstrating how non-factorization from a source, such as periodic resonance crossing, can be transferred along the machine and is a property of the beam distribution, rather than the lattice.

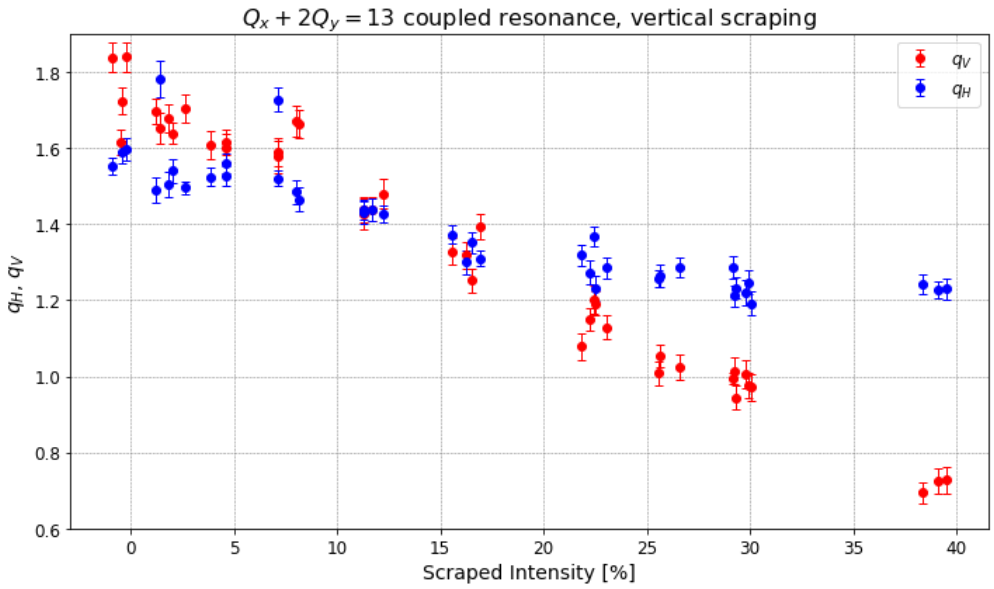

Figure 6.3: Change in vertical and horizontal beam profile, shown as a fit of the q-Gaussian q-parameter due to a vertical scraping in the SPS for the bunch type A 'coupled resonance'.

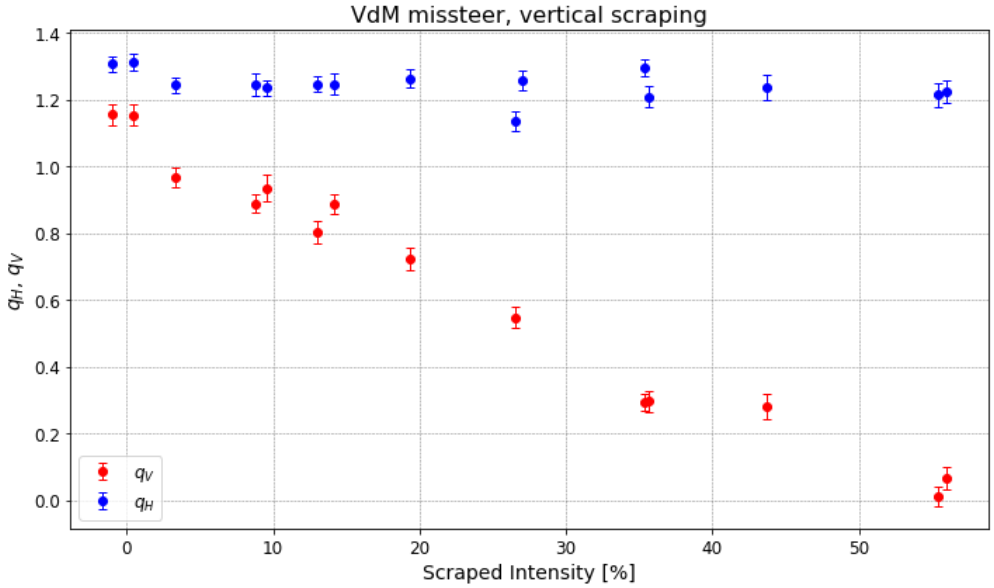

Figure 6.4: Change in vertical and horizontal beam profile, shown as a fit of the q-Gaussian q-parameter due to a vertical scraping in the SPS for the bunch type B 'van der Meer missteer'.

6.3 Non-Factorization Experiment at LHC Injection Energy

6.3.1 Experimental Configuration

The scraping experiments in the SPS demonstrated that non-factorization can be transferred to higher energy machines in the CERN accelerator complex. For the van der Meer calibration scans, non-factorization is observed at the LHC flat top, when the beams are colliding. To test whether a source of non-factorization originating from lower energy machines could contribute to the non-factorization of the bunch distribution during collisions (at top energy), we can first measure the NF at LHC injection, and then at top energy. Different bunch types, with different PSB configurations, were tested at LHC injection for their NF properties via beam scraping (collimation) and profile measurements. These bunch types included the 'coupled resonance', 'van der Meer missteer', and two additional van der Meer-style factorizable bunches, each with slightly different preparations in the PSB.

As per the filling scheme shown in Fig. 6.5, a total of 8 bunches were in the machine, with 4 in Beam 1 and 4 in Beam 2. Some key parameters of the different bunch types tested are listed in Tables 6.1 and 6.2. The LHC machine parameters at injection are detailed in Table 6.3.

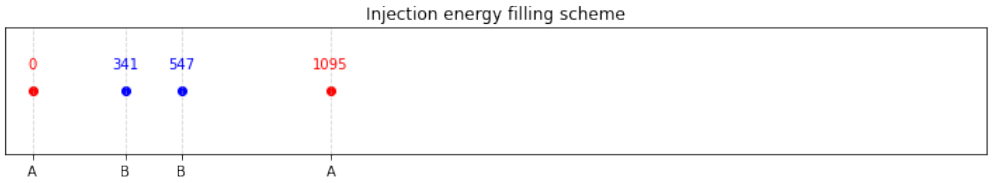

Figure 6.5: Filling scheme for experiment at injection energy, shown for one circulating beam. A, B, refer to two different bunch types with different preparations in lower energy injectors.

Table 6.1: Bunch types and their parameters (Part 1)

Bunch Type	**Scraping**	**PSB Missteering**
A: Coupled resonance	PSB injection	No
B: vdM missteer	PSB injection, SPS extraction	Yes
C: vdM integer	PSB injection, SPS extraction	No
D: vdM integer + missteer	PSB injection, SPS extraction	Yes

Table 6.2: Bunch types and their parameters (Part 2)

Bunch Type	**Resonance Correction**	**Predicted Non-Factorization**
A: Coupled Resonance	Corrected	High, horizontal-vertical
B: vdM missteer	Partially corrected	Low
C: vdM integer	Corrected	Low
D: vdM integer + missteer	Partially corrected	Low

Table 6.3: Beam and machine parameters for experiment at injection energy.

Parameter	**Injection MD**
Beam energy [GeV]	450
Optics	van der Meer
Crossing angle [μrad]	0
Emittance [μmrad]	2.5–3.5
Intensity [ppb]	$\sim 1 \times 10^{11}$

The essential protocol for the experiment to test the NF of each bunch is detailed as follows:

1. Inject different bunch types (4) into each circulating beam (1 or 2).
2. Move the collimators into the beam in steps of 5 μm until the loss level indicates that there has been an interception with the beam, and continue moving the collimator until the total lost intensity is approximately 2%.
3. After each collimation step, take profile measurements in the horizontal and vertical planes.
4. Repeat by moving the collimators further into the beam for another 2% intensity loss.
5. When the intensity is below a threshold (approximately 40%), dump the beam and refill the machine with the new bunch variants.

6.3.2 Results at LHC Injection Energy

The bunch by bunch losses are plotted for an injection fill with the A, 'coupled resonance' and B, 'vdM missteer' type bunches in Fig. 6.6. The losses are plotted as a function of the vertical collimator gap, and for each bunch and beam (1 or 2). The two bunch types are in different slots. Slot 0 is an A bunch, and slot 547 is a B bunch. The losses for both bunch types associated with collimator adjustments are significant when compared to the slower losses caused by diffusion. The loss patterns differ between the two bunch variants, due to differences in the tail extent and distribution. Notably, losses for the B begin when the vertical collimator gap is smaller, and the loss gradient differs from that of the A bunch. The losses alone cannot tell us about the non-factorization of the distribution, but can give information on the tail content. Slow losses (between collimation steps) are higher for the type A bunches.

To examine the NF, the bunch profiles from wire scanner measurements are plotted as a function of the vertical collimator gap (colour-coded) and are normalized to have an area of 1. Additionally, there is further normalization such that the collimator gap is expressed in units of collimator σ. This convention assumes that 1σ corresponds to the σ of a bunch with an emittance of 3.5 μmrad. To apply this normalization, the optics at the position of the collimator must be known, and these are provided in Table 6.4. The first normalization allows us to visualize the probability density function (PDF) rather than the profile. For fully factorizable bunches, the horizontal PDF would remain unchanged during vertical scraping.

Vertical collimator	β_x **[m]**	β_y **[m]**
Vertical collimator Beam 1	150.4	69.1
Vertical collimator Beam 2	146.1	70.3

Table 6.4: The β functions at the location of the vertical collimators.

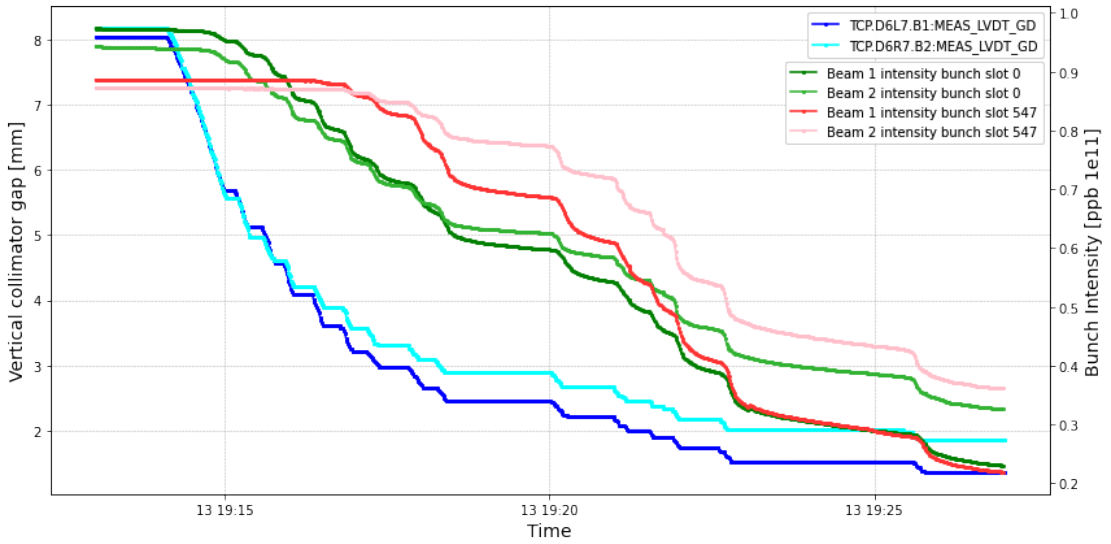

Figure 6.6: The vertical collimator gap for Beam 1 and Beam 2 against the intensity of an A type (bunch slot 0) and the B type (bunch slot 547).

Figure 6.7 shows the changing PDF in the horizontal and vertical planes as a function of vertical collimator position, for Beam 2. The data is presented on a logarithmic scale, with the normalizations described earlier to reveal the PDF. The A, 'coupled resonance' bunch (top), and the B, 'vdM missteer' bunch (bottom), are plotted with the same scale for the collimator position.

For the A bunch, with the vertical collimator at a large gap, there are large tails (relative to a Gaussian distribution) in both the horizontal and vertical planes. As the vertical collimator gap narrows, the tails in the vertical plane are reduced, and the horizontal PDF also changes, with the tails being reduced in the horizontal plane due to scraping in V. This behaviour indicates NF for the transverse planes in the distribution, showing that some of the NF is preserved from the PSB.

For the B bunch (bottom), the initial tails are smaller. As the collimator gap decreases, the vertical PDF changes, but the horizontal PDF remains almost constant, indicating a more factorizable bunch. Although the bunches are in the same machine, experience the same nonlinearities, and have the same linear coupling, their NF differs due to differences in their production schemes earlier in the accelerator chain.

Figure 6.8 shows the results for another fill with two bunches of the A and two of type B. Compared to Fig. 6.7, a higher sextupole current was used to excite the coupled resonance in the PSB. As a result, the tails are visibly larger when the collimator gap is large, and the NF becomes more apparent with scraping and profile measurements (top). The result for the B (bottom) is shown to be reproducible.

Figures 6.9, 6.10, 6.11 and show the results of collimator and profile measurements, for three

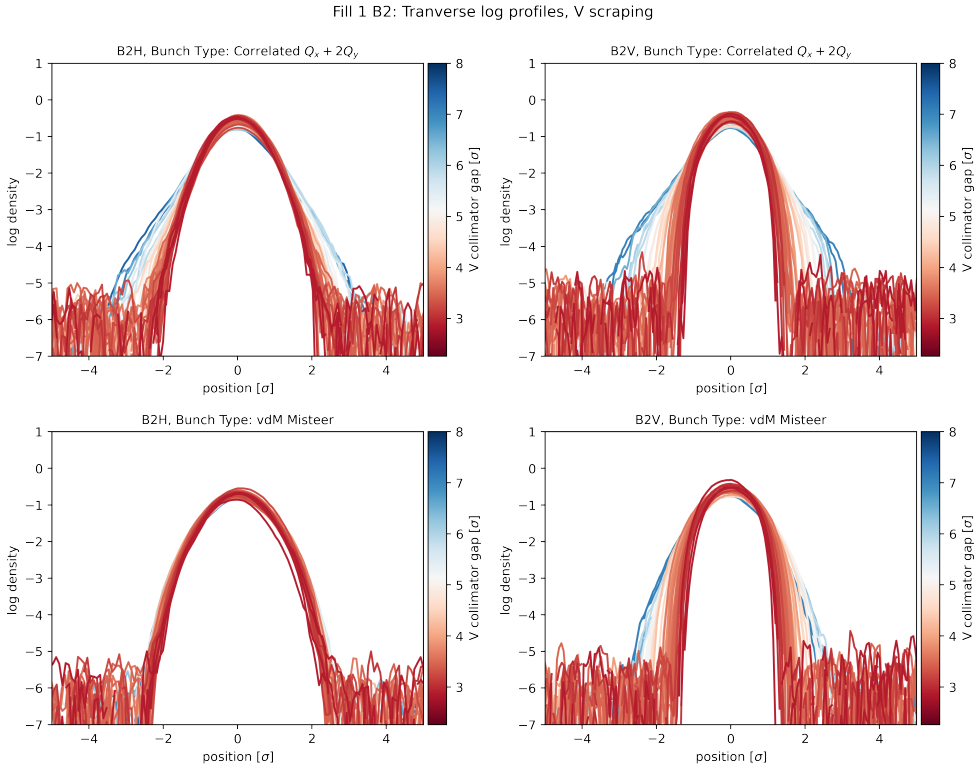

Figure 6.7: Wire scanner measurements during LHC scraping at injection for bunch type A ‘Coupled Resonance’ and B ‘vdM Missteer’, LHC Beam 2.

slightly different vdM bunches, which all aim to be factorizable. The scale of the vertical collimator is set to be the same for all bunches, and is finer than when comparing with the ‘coupled resonance’ type. On the finer scale, differences in the factorization can be seen for the different vdM bunches. The B ‘vdM missteer’ bunch, Fig. 6.9 performs best at LHC injection compared with the C ‘vdm injection’ and the D ‘vdm missteer + injection’ types. For the B, ‘vdM missteer’ the interactions with resonances are minimised in the PSB. The vdM run (yearly luminosity calibration run) was the day after this experiment, and based on the results, the B ‘vdM missteer’ variant was used. Measuring the NF with collimation and wire scanner measurements is an independent way for the to determine the level of NF in a bunch and doesn’t require the complicated analysis of the van der Meer scans.

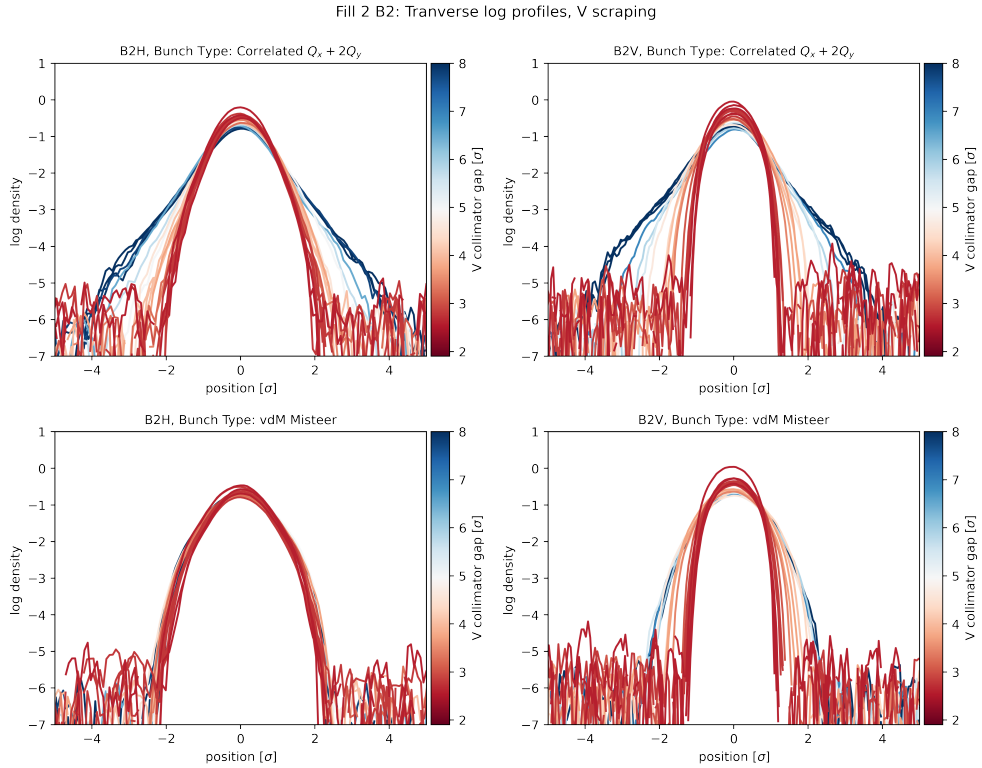

Figure 6.8: Wire scanner measurements during LHC scraping at injection for bunch type A, 'Coupled Resonance' and B, 'vdM missteer', LHC Beam 2. The sextupole current in the PSB for the 'coupled resonance' type was increased with respect to fill 1.

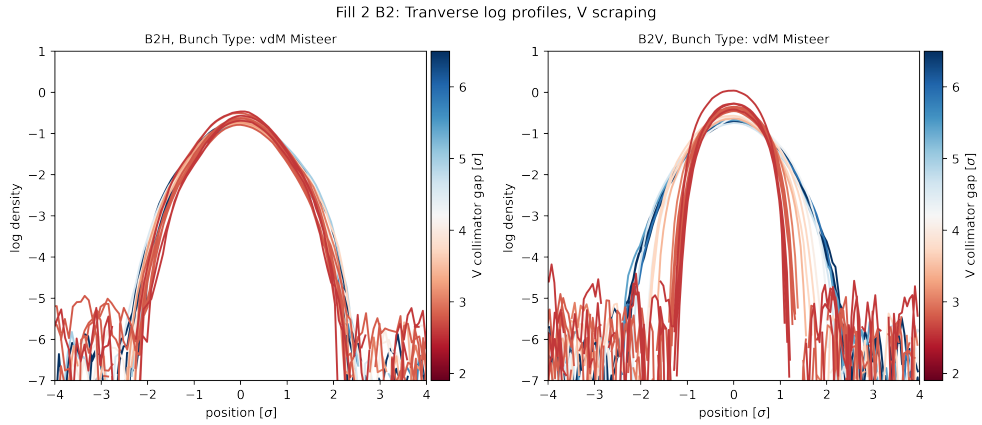

Figure 6.9: B: vdM bunch made with injection missteering in the PSB. Vertical scraping at LHC injection

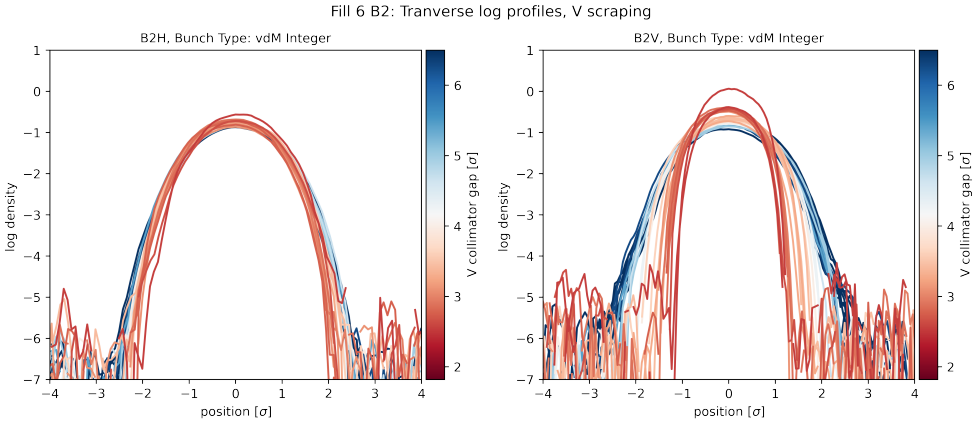

Figure 6.10: C: vdM bunch made via method of blow up on integer resonances in the PSB. Vertical scraping at LHC injection.

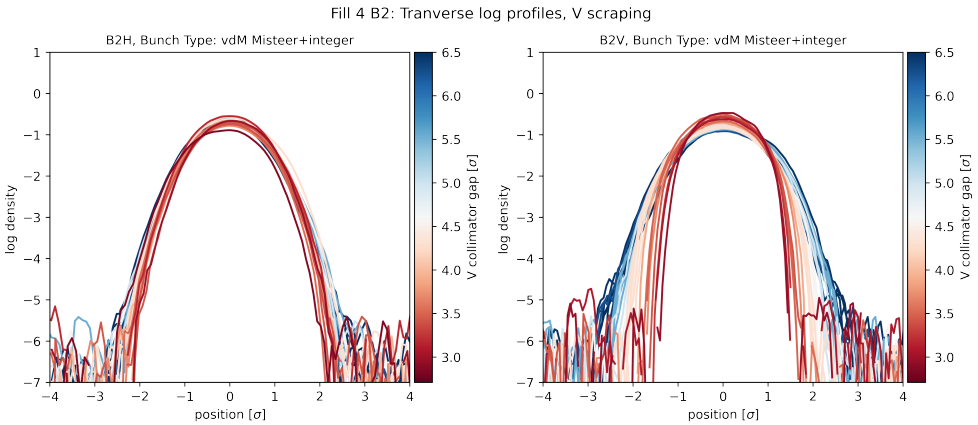

Figure 6.11: D: vdM bunch made with injection missteering and blow up on the integer resonances. Vertical scraping at LHC injection.

6.4 Non-Factorization Experiment at LHC Top Energy

To determine whether NF created in the injectors is observable at top energy in the LHC, an experiment was conducted in collaboration with the high energy physics experiments. The aim was to see if the bunch non-factorization properties would be preserved up to top energy (6.8 TeV), and if a difference could be noticed between the two (A,B) during the van der Meer scans.

The flat top experiment was during one single fill, and there were 12 injected bunches, 6 type A and 6 type B per circulating beam, as per the filling scheme in Fig. 6.12. The experiment had two separate parts (one with CMS, ATLAS and LHCb, and the other with scraping and wire scanner measurements). The protocol is described:

1. Inject different bunch types, 6 per type, into each circulating beam (12 total per beam).
2. Ramp in energy from 450 GeV to 6.8 TeV.
3. Put the beams into collision.
4. Experiments, CMS, ATLAS perform van der Meer scans, 2 hours for ATLAS followed by 2 hours for CMS.
5. After the van der Meer scans, scraping with the vertical collimators for both Beam 1 and 2. Periodic wire scanner measurements for the profiles after each movement of the vertical collimators.
6. The beams are dumped when the intensity goes below a threshold.

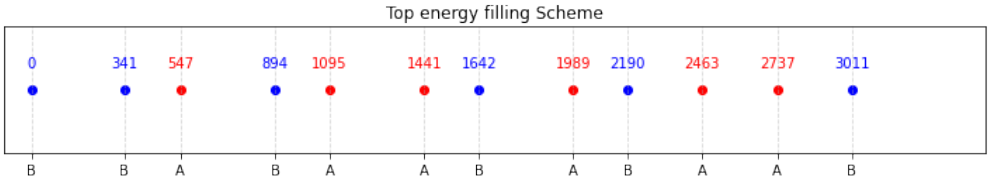

Figure 6.12: Filling scheme for experiment going to top energy and collision (6.8 TeV).

As of writing, the results from the van der Meer scans of ATLAS and CMS during the flat top experiment (**not the normal calibration run**) have not been published. During the vdM scans in CMS and ATLAS, type A bunches 'coupled resonance' are collided with type A, and type B bunches 'vdM missteer' with type B, after the energy ramp. The visible cross-section, σ_{vis}, relates the observed rate to the luminosity. Ideally, σ_{vis} should be a constant and independent of the beam profile. However, in the presence of non-factorization, σ_{vis} is reduced. Private

communication with CMS told us that preliminary results reveal the σ_{vis} was smaller for the type A bunches compared to type B by 3 standard deviations, which is significant. This provides evidence that some of the differences in NF due to the different PSB schemes are preserved up to top energy.

Between the start of collisions at top energy, and the scraping measurements, approximately 6 hours elapsed. During this time, there were significant losses, especially for the 'coupled resonance' bunches, resulting in changes to the bunch distributions. Figure 6.4 shows the effective cross-section, which is the losses (from the diamond beam loss monitors, DBLMs), divided by the luminosity for the period of collisions (sometimes referred to as 'stable beams') [69]. Two families are visible, the A 'coupled resonance' in red, and the B 'vdM missteer' in blue. The B bunches are much closer to the burn-off limit (losses due to collisions only), while for the 'coupled resonance' type there are extra losses.

Effective cross-section during period of collisions for two different bunch types

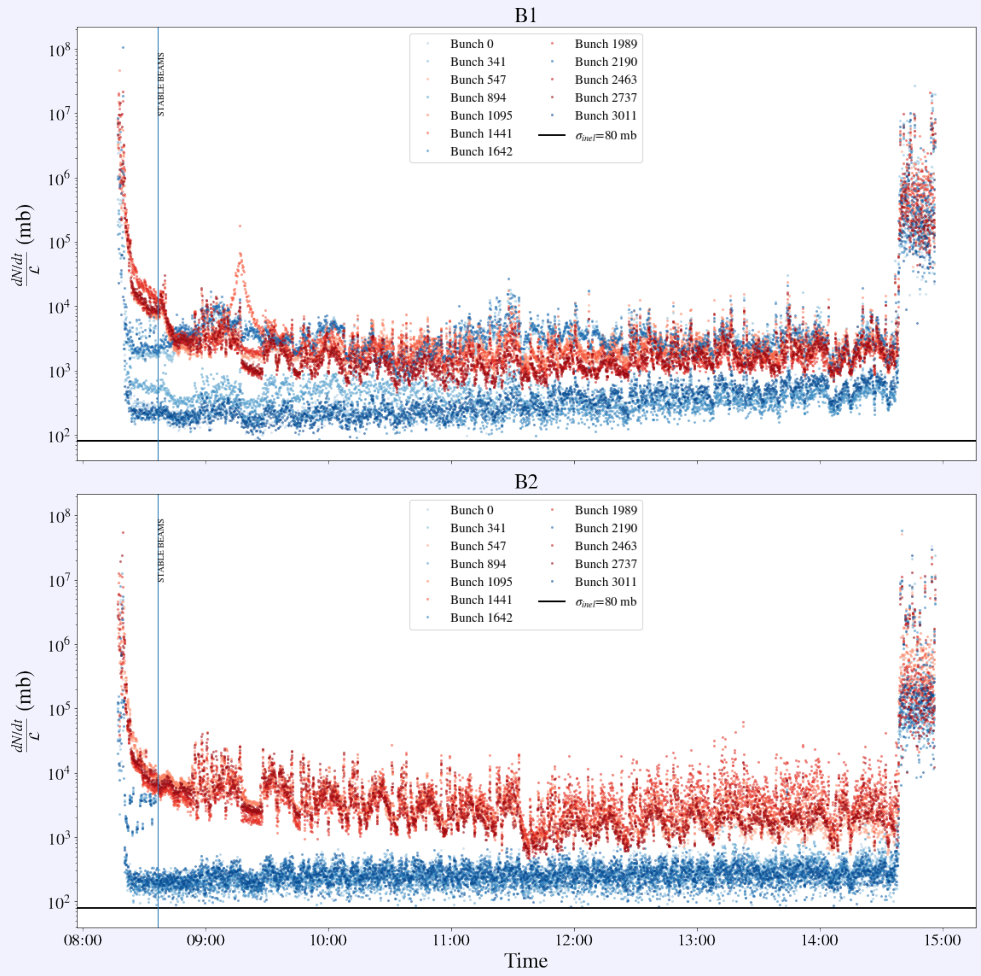

Figure 6.4: The effective cross-section (relates luminosity to the loss rate) during the collision period, during which there were van der Meer scans in ATLAS and CMS. Courtesy of S. Kostoglou [69]. The burn-off limit is plotted by the black line, and is calculated from the predicted proton-proton inelastic cross-section [70]. Any losses above the burn-off limit are not from luminosity production. After around 14:40 stable beams has ended.

Figures 6.14 and 6.13 show the PDF as the vertical collimator gap reduces at top energy in the LHC after 6 hours of collisions. The non-factorization for the A 'coupled resonance' bunch is reduced in comparison with injection energy, but there is still some evidence of non-factorization in the tail of the distribution. For the B bunch, it looks fully factorizable on the scale given. These results show that a non-factorization from a source in the CERN injectors can be preserved up to top energy. Losses change the distribution and hence the non-factorization is reduced.

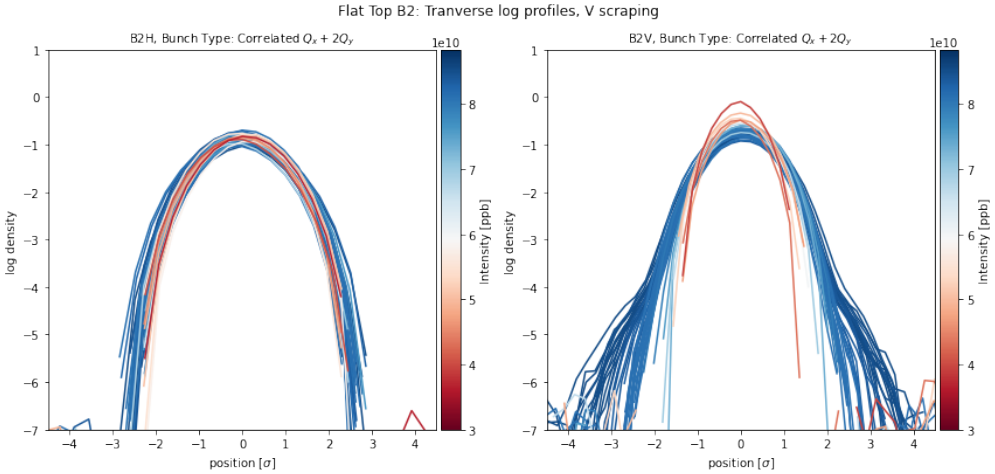

Figure 6.13: Scraping and wire scanner profiles at top energy in the LHC for the 'coupled resonance' bunch.

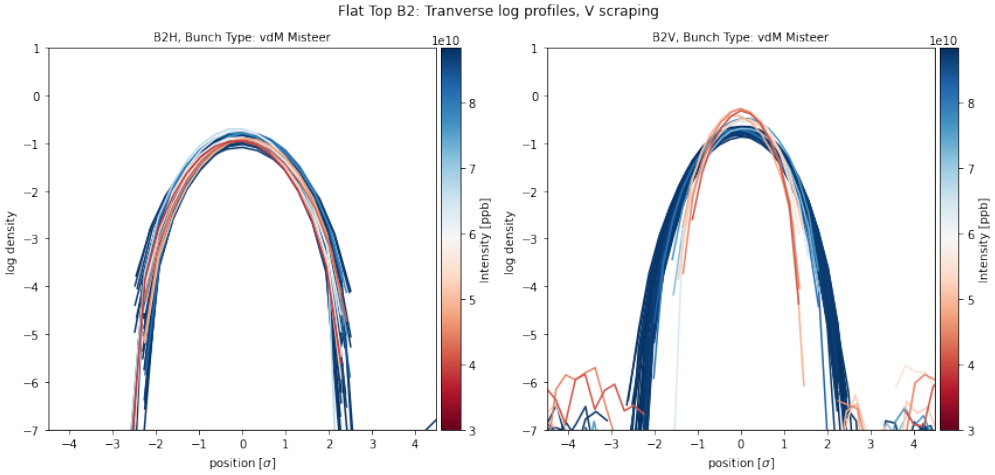

Figure 6.14: Scraping and wire scanner profiles at top energy in the LHC for the B 'van der Meer missteer' bunch.

6.4.1 Lifetime Observations for Bunches with Different Tails

Partially due to the observed difference in the bunches with respect to their tail content and resultant loss rate from this experiment, there were efforts to create a bunch variant for operation in the LHC with lower tails, 'BCMS low tail', (Beam Compression, Merging and Splitting). The bunch has various beam-dynamics optimisations and scraping of the beam tail. After some initial operational experience, this variant has an improved lifetime in the LHC compared to the nominal 'BCMS' [71]. This variant has now been the one used in physics (luminosity production), fills since July 2024 up to the time of submission of this thesis, September 2024.

6.4.2 VdM 2024 calibration run

The two LHC experiments described in this chapter took place one day before the **usual vdM calibration run of 2024**. Based on the results of the injection experiment and the scraping measurements, it was decided that the bunch type to be used in the vdM run would be the 'vdM missteer'. This bunch is created in the free space of the tune diagram, away from resonances, and thus, intuitively, would have less NF based on the evidence seen that periodic resonance crossing of coupled resonances leads to NF. However, it was also observed during the injection MD that it had the least observable NF in scraping measurements of all the vdM bunches tested. The high amplitude particles were also removed at the SPS via scraping, as it is shown that the NF observed is at high amplitudes. As of writing, the results of the vdM 2024 run and the size of the NF correction have not been published.

6.5 Summary

The results presented show that to improve the non-factorization at collisions in the LHC, it is necessary to remove any non-factorization source from the injectors. NF could be introduced by other mechanisms and also in high energy machines, however in low energy machines, the space charge is strongest, and thus the tune spread is largest, leaving the distribution more susceptible to resonances. At higher energies, in addition to the space charge tune spread being smaller, the beam is more rigid. Given the online analysis possible with scraping and wire scanner measurements, the bunches can be tuned according to the observed non-factorization before injection in the LHC (at the SPS energy ramp). The observation of the relaxation over the fill of the non-factorization is consistent with the larger losses (and lower lifetime) of the bunch with larger, non-factorizable tails. The non-factorization is nonlinear in the sense it is present for higher-amplitude particles, consistent with prior observations in the lower energy machines (SPS, PSB).

The results of the 2024 van der Meer calibration run will not be published for some time. We will then see if the improvements made in the injector machines have had a direct impact on the size of the uncertainty from the NF source.

Note: The method detailed in Chapter 3 to reconstruct the full transverse distribution could be applied with these measurements. However, the method was realised after these measurements were taken, and the scraping steps are too large to justify the assumption of a continuous distribution. Furthermore, the time between measurements was too large, and the diffusion rate is not negligible. This could be investigated in further detail.

7 Conclusions

The present dissertation has focused on the transverse beam distribution, and how it is not unique given the observation of a beam profile. Depending on the constraints on the free parameters, it has been shown that there are consequences for loss behaviour in a synchrotron. Furthermore, the luminosity, the figure of merit for a collider, depends on the full transverse distribution. In the LHC, where transverse beam profiles are observed that have heavy tails with a q-parameter up to 1.4, the difference in instantaneous luminosity can be on the order of 5%.

It has been demonstrated how space charge and periodic crossing of coupling resonances can lead to a change in the beam distribution in terms of its non-factorization. This has been done in an experimental campaign in the CERN Proton Synchrotron Booster. Beam scraping and profile measurements were used in the absence of other methods to characterize the NF. A period of artificial excitation of a third order coupling resonance, followed by a nearly 'linear' machine beyond the space charge, show that NF was introduced to the bunch and it remains.

These results have been benchmarked with multi-particle tracking simulations. The behaviour in terms of the profile evolution and the NF agrees well. Additionally, an understanding of the dynamics is gained with simulation of the single particle. The J_x, J_y amplitudes are changed when the particle crosses the resonance condition in a ratio that is according to the resonance coefficients. The random scattering in both planes gives an ultimate increase in amplitude which, after many turns, changes the overall distribution to have high amplitude particles in one plane which are more likely to have a high amplitude in the other transverse plane. Increasing the synchrotron period artificially in simulation, so that the longitudinal motion is almost frozen, shows how the particle can be trapped in the resonance condition.

Motivated by the non-factorization bias in the luminosity calibration measurement at the LHC, the experiment to show how the NF introduced via excitation of coupling resonances demonstrated that the property was preserved (to some extent) up to LHC injection. This is consistent with results that a non-factorizable distribution can be matched. With the joint experimental campaign between the accelerators and high-energy physics experiment,

preliminary results show a systematic difference in the two bunch types (non-factorizable distributions, A, factorizable distributions, B, in terms of their measured σ_{vis} when the beams are in collisions for van der Meer scans. This is a preliminary indicator in the difference in the non-factorization of the bunches with the same lattice. These results show it is important to remove sources of non-factorization in the LHC injectors, and results of this thesis have improved our ability to do so. Online scraping measurements allow the comparison of non-factorization between bunches, and the avoidance and the correction of resonances has been shown to be paramount. This was done for the first time in 2024. Results of the van der Meer run and the correction due to NF have not been published at the time of writing.

Non-factorization could be introduced also in processes in higher energy machines, however the distribution is particularly sensitive to coupling resonances in lower energy machines as the beam is less rigid. Moreover, the space charge tune spread is large. It is unclear how magnet imperfections scale with energy. Processes that destroy non-factorization could be investigated, for example, Gaussian scattering.

For the operational beams in the CERN accelerator complex, results which were derived from the experiments in the thesis, (namely the difference in losses for beams with low or high tail content), partly motivated the creation of a 'low tail' operational beam variant. This beam variant has been shown to reduce the losses in the LHC and improve the performance. This variant has been the one used in operation since July 2024. Non-factorization has also been observed in operational beams with orthogonal experiments via the scraping and profile measurements. These beams have higher brightness (intensity/emittance), than the van der Meer beams, and the beams used in the PSB experiment to introduce non-factorization. The source could be from resonances driven by machine imperfections or by space charge. This should be taken into account to accurately model the losses in the CERN accelerator complex.

A Inverse Sampling Method

Below details a method adapted from [40], to sample from a particle distribution in 4D with inverse sampling.

Given the definition of the super radius with the canonical variables,

$$m = \sqrt{r_x^2 + r_y^2} = \sqrt{x^2 + p_x^2 + y^2 + p_y^2}, \tag{A.1}$$

we define square of the super radius:

$$F = m^2 = r_x^2 + r_y^2 \tag{A.2}$$

If we want a projection in the x plane fitting a certain known distribution, and we impose hyper-circular symmetry in 4D, then knowing how F, the super radial square, is distributed allows us to sample particles. In chapter 3 we derive 4D distribution functions as functions of m, $f_{4D}(m)$. From this we can find the $f_{4D}(m^2) = f_{4D}(F)$.

Given

$$f_{4D}(x, p_x, y, p_y) = \frac{dN}{dx dp_x dy dp_y} = f_{4D}(F), \tag{A.3}$$

and that the distribution function is normalized under the condition,

$$\int_{-\infty}^{\infty}\int_{-\infty}^{\infty}\int_{-\infty}^{\infty}\int_{-\infty}^{\infty} f_{4D}\left(x, p_x, y, p_y\right) \mathrm{d}x\, \mathrm{d}p_x \mathrm{d}y\, \mathrm{d}p_y = 1. \tag{A.4}$$

To populate the 4D phase space satisfying the distribution $f_{4D}(f)$=

$$f(F)$$

, we define a function $g(F)$, the distribution of the values of F:

$$g(F) = \pi^2 f_{4D}(F) F = \frac{dN(F)}{dF}, \tag{A.5}$$

where $dN(F)$ is the number of particles in the interval $(F + dF)$,

$$dN(F) = f_{4D}(F) F \, \mathrm{d}F \int_0^{2\pi} \mathrm{d}\varphi \int_0^{2\pi} \mathrm{d}\theta \int_0^{\pi/2} \sin 2\psi \mathrm{d}\psi = \pi^2 f_{4D}(F) F \, \mathrm{d}F. \tag{A.6}$$

The distributions are generated with an inverse transverse sampling method and random angle distributions, analogous to a Box-Muller type generation.

The integral distribution of F is generated via,

$$G(F) = \int_0^F g(F') \mathrm{d}F'. \tag{A.7}$$

The inverse function I is generated by mapping $G(F)$ back to F,

$$F = I(G(F)) \tag{A.8}$$

Then, the distributions are generated as follows,

$$\begin{aligned} x &= A_x \cos(\beta_x) \\ p_x &= -A_x \sin(\beta_x) \\ y &= -A_y \cos(\beta_y) \\ p_y &= A_y \sin(\beta_y), \end{aligned} \tag{A.9}$$

where for each value of $I(G)$, A_x and A_y are two random numbers generated such that,

$$m^2 = A_x^2 + A_y^2, \tag{A.10}$$

and β_x, β_y are generated uniformly on $[0, 2\pi]$.

Parallels can be drawn to a Box-Muller transformation, used for normalized distributions to generate two independent random deviates [46],

$$Z_0 = R\cos(\theta) = \sqrt{-2\ln U_1}\cos(2\pi U_2) \tag{A.11}$$

and

$$Z_1 = R\sin(\theta) = \sqrt{-2\ln U_1}\sin(2\pi U_2) \tag{A.12}$$

where Z_0 and Z_1 are independent random deviates from a normal distribution. In the case of 4D, we have 2 angles β_x and β_y generated uniformly (analogous to θ), and 2 random variables A_x and A_y which come from the 4D distribution as described above (analogous to U_1 and U_2).

B Physicality of a beam profile

Given that distributions in linearly normalised phase space, in a linear lattice, should be circular in the Poincaré section $x - p_x$, the single inverse Abel transform to find $f(r_x)$ is a test for physicality of a profile. The $f(r_x)$, must be defined positive. The condition for the $f(r_x)$ to be defined positive, depends on the integral, and it cannot be defined a condition on the $f(x)$.

Figures B.1 and B.2 show examples of unphysical beam profiles, as $f(r_x)$ is negative for certain r_x.

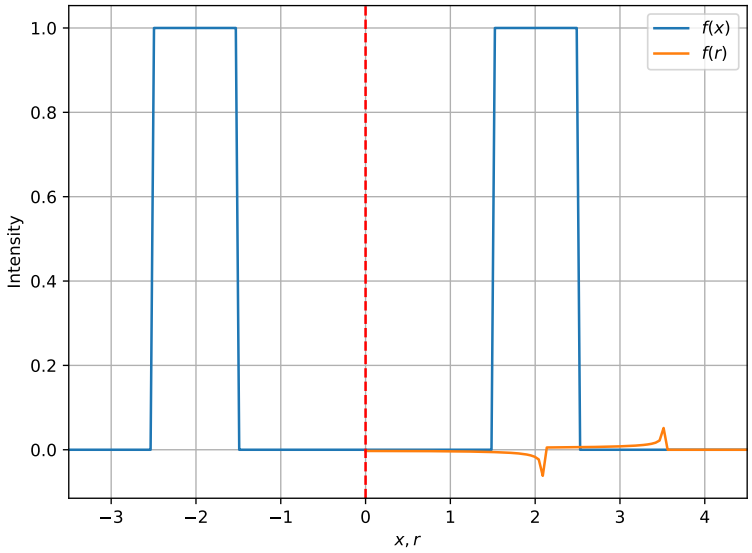

Figure B.1: Example of 'hollow' rectangular beam profile, projected on x in blue. The inverse Abel transform of $f(x)$, $\mathscr{A}^{-1}[f(x)]$ is plotted in orange.

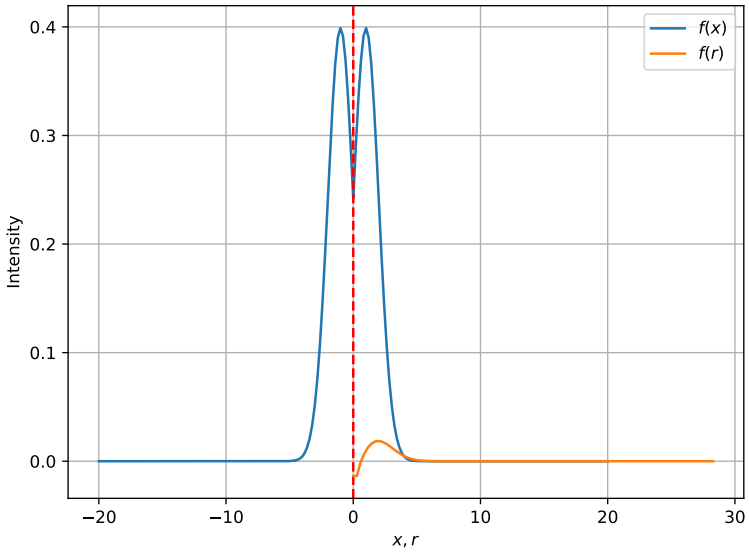

Figure B.2: Example of discontinuous beam profile, projected on x in blue. The inverse Abel transform of $f(x)$, $\mathscr{A}^{-1}[f(x)]$ is plotted in orange.

C The Abel Transform for the Calculation of Collimated Beam Profiles

Given a physical space distribution of a particle beam in y, we can find the percentage of particles in the distribution which is removed by an aperture, or collimation set at a particular amplitude. We can also find the new distribution of particles remaining after the collimation using the Abel transform.

First, it is easier to normalise the distribution using the machine parameters at the measurement point (linear normalisation of phase space). Given the normalised PDF($\hat{y}$), to calculate the cut of a distribution from a scraping or collimation, we need to know the PDF(J_y).

First we can use the inverse Abel transform to go from the $y(\sigma)$ to PDF(r_y), where r_y is defined:

$$r_y = \sqrt{\hat{y} + \hat{p_y}^2}. \tag{C.1}$$

$$\text{PDF}(r_y) = 2\pi r_y \mathscr{A}^{-1}[\text{PDF}(\hat{y})] \tag{C.2}$$

Where $\mathscr{A}^{-1}$ is the inverse Abel transform.

Given a distribution $PDF(r_y)$, we need to find the $PDF(J_y)$ where $J_y = r_y^2/2$. From probability theory:

If $F_X(x)$ is a PDF of a random variable X, and

- $Y = g(X)$
- $g(x)$ is differentiable
- $g(x)$ is a strictly increasing function: $x_1 < x_2$ then $g(x_1) < g(x_2)$

then:

$$F_Y(y) = F_X(x_1)/g'(x_1). \tag{C.3}$$

Where

$$g(x_1) = y. \tag{C.4}$$

Therefore, we can find the PDF of $J_y = r_y^2/2$ from the PDF of r_y,

$$g(r_y) = r_y^2/2, g'(r_y) = r_y, \tag{C.5}$$

therefore,

$$\text{PDF}(J_y) = PDF(r_y)/r_y. \tag{C.6}$$

Then, to find the percentage in the tails, we can remove the distribution beyond an aperture limit, a, $J_y > A$. The probability beyond the aperture limit A gives us the percentage of particles the collimator has removed. To find the new distribution with the removed particles, PDF($J_y|J_y < A$) is transformed back into a PDF($r_y|J_y < A$), and then PDF($\hat{y}|J_y < A$) with a forward Abel transform and a linear manipulation.

D Numerical Example of the Scraping Protocol

A numerical scraping of two distributions which have Gaussian projections, one fully factorizable and one non-factorizable is demonstrated, We will aim to find back their $f(J_x, J_y)$ given access to information on only one transverse plane. The derivation of the two different distributions with Gaussian projections (A1, A2) is given in Chapter 3.

Working in J_x, J_y space, the A1. distribution is plotted in Fig. D.1.

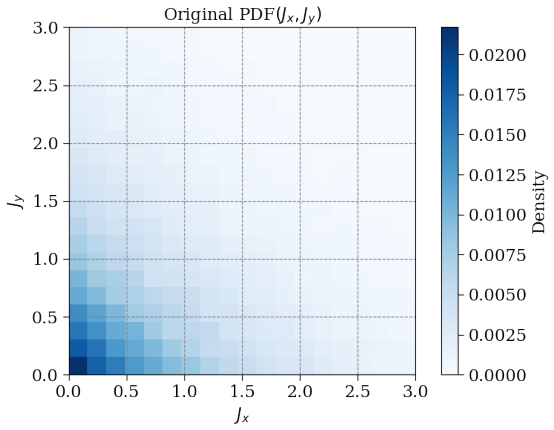

Figure D.1: True joint PDF(J_x, J_y) (A1.) for a factorizable 4D Gaussian.

In J_x, J_y, a scraping or collimation is removing parts of the distribution which have a $J_y > A_i$, as explained above. The distributions $f(J_x|0 < J_y < A_{i+1..n})$, from subsequent y apertures, A_i, are plotted in Fig. D.2. Due to the fact the distribution is factorizable, the normalised PDFs $f(J_x|0 < J_y < A_{i+1..n})$ are the same (beyond numerical errors).

Then, the PDFs for the intervals between successive A_i are calculated, PDF($J_y|A_{i+1} < J_y < A_i$), by finding the difference between non-normalised scraping measurements. These functions are plotted in Fig. D.3.

With the approximation to a continuous distribution and multiplication of the marginal PDF,

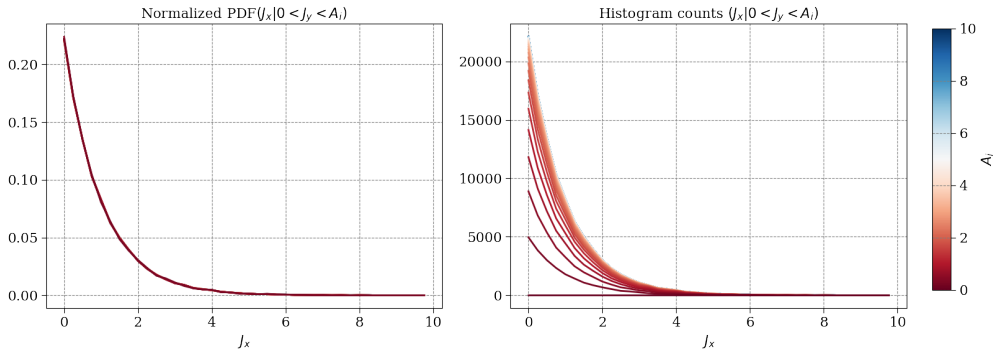

Figure D.2: Left: Normalized conditional PDFs PDF($J_x|0 < J_y < A_i$) Right: Histograms of ($J_x|0 < J_y < A_i$) for a particle distribution taken from the initial joint PDF(J_x, J_y) of the factorizable 4D Gaussian.

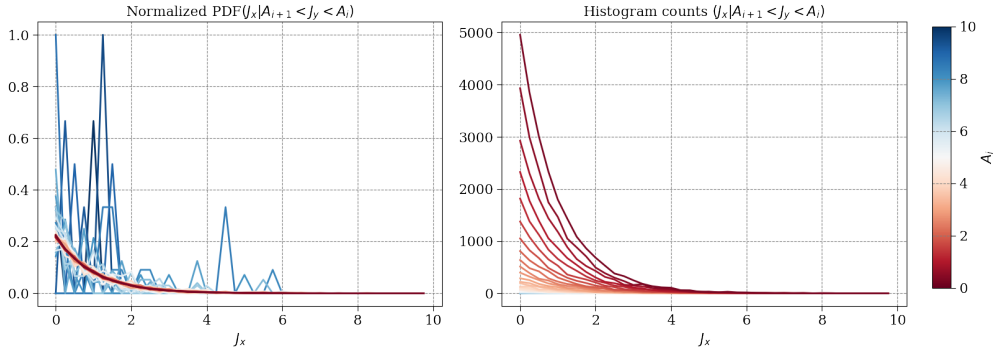

Figure D.3: Left: Normalized conditional PDFs PDF($J_x|A_{i+1} < J_y < A_i$) Right: Histograms of ($J_x|A_{i+1} < J_y < A_i$) for a particle distribution taken from the initial joint PDF(J_x, J_y) of the factorizable 4D Gaussian.

PDF(J_y), we find back the joint distribution, PDF(J_x, J_y), plotted in Fig. D.4.

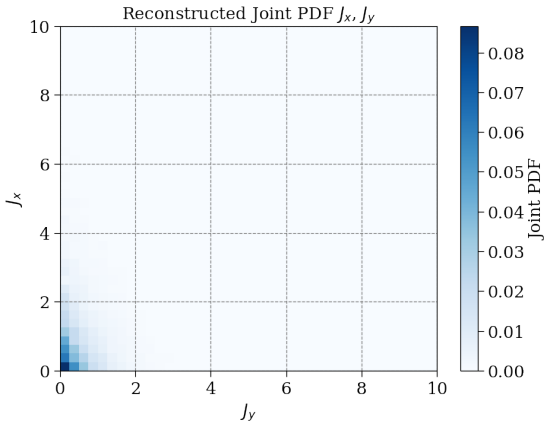

Figure D.4: Joint PDF(J_x, J_y) reconstructed from successive PDF$(J_x|A_{i+1} < J_y < A_i)$ for different numerical scraping.

Repeating the same with the A2. distribution, plotted in J_x, J_y in Fig. D.5.

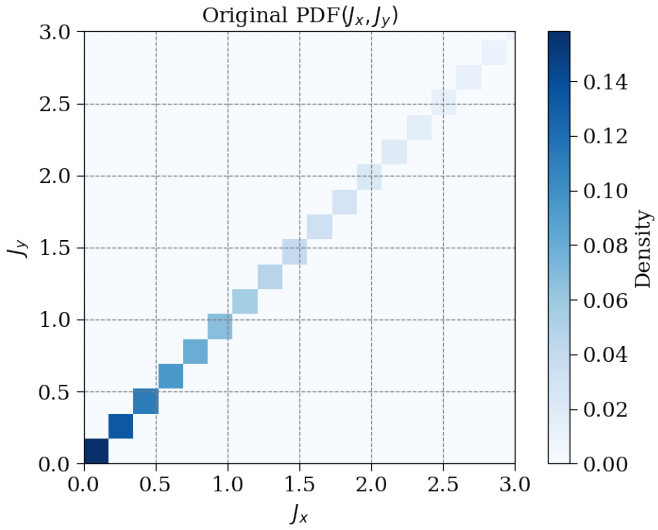

Figure D.5: True joint PDF(J_x, J_y) (A2.) for a non-factorizable 4D Gaussian.

The PDFs for each successive scraping aperture, are plotted in Fig.D.6. Since the distribution is non-factorizable the normalised conditional PDFs are not the same.

Then, the difference between the PDFs to calculate $f(J_y|A_{i+1} < J_y < A_i)$ is found, plotted in Fig.D.7.

Then, using the marginal PDF(J_y) the original distribution is estimated with Bayes' theorem, plotted in Fig. D.8.

We have shown numerically how it is possible to reconstruct the PDF(J_x, J_y) of an unknown beam distribution through scraping measurements. This method is not well-developed for

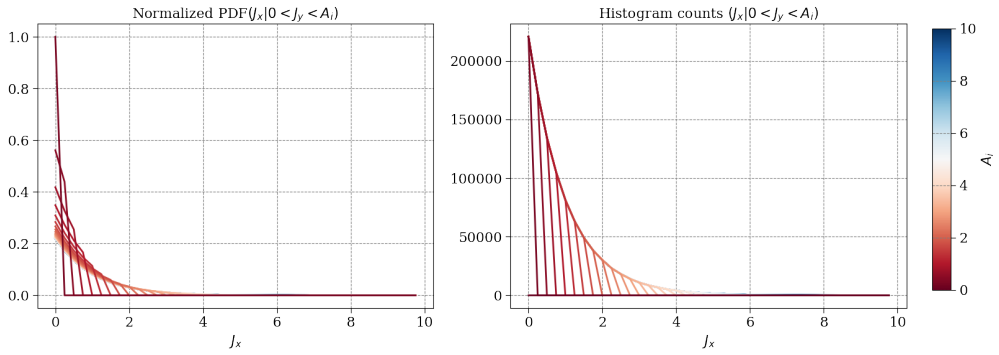

Figure D.6: Left: Normalized conditional PDFs PDF($J_x|0 < J_y < A_i$) Right: Histograms of ($J_x|0 < J_y < A_i$) for a particle distribution taken from the initial joint PDF(J_x, J_y) of the non-factorizable 4D Gaussian.

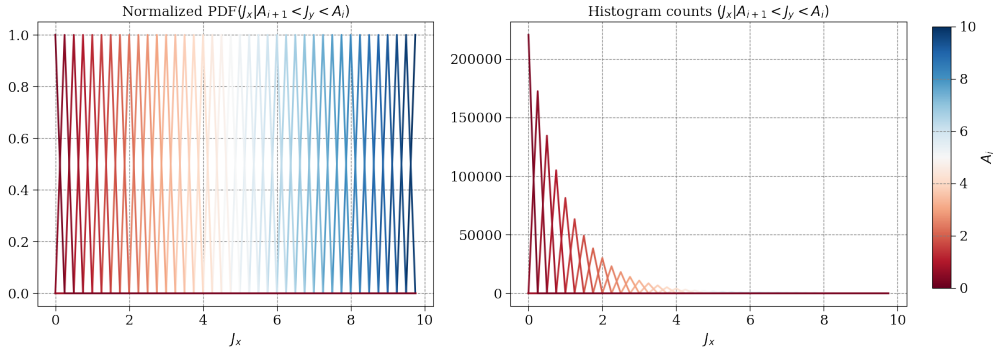

Figure D.7: Left: Normalized conditional PDFs PDF($J_x|A_{i+1} < J_y < A_i$) Right: Histograms of ($J_x|A_{i+1} < J_y < A_i$) for a particle distribution taken from the initial joint PDF(J_x, J_y) of the non-factorizable 4D Gaussian.

experiment as of writing. It depends greatly on the noise of the profile measurement, and the rate of diffusion during the period of the measurement. Scraping and profile measurements in both planes has however been used to determine the relative non-factorization between distributions in Chapters 4 and 6.

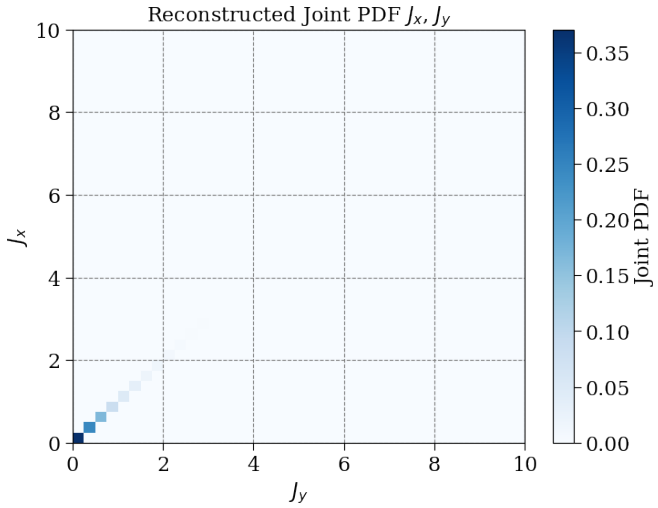

Figure D.8: Joint PDF(J_x, J_y) reconstructed from successive PDF($J_x|A_{i+1} < J_y < A_i$) for different numerical scraping for the A2. distribution.

E Non-Factorizable Gaussians

A Python Jupyter notebook about Gaussian non-factorizable distributions by Guido Sterbini *g.sterbini@cern.ch*.

Connected to base (Python 3.10.12)

Introduction

Let us consider a distribution $\rho(x,y)$ where x, y are horizontal and vertical positions of a 4D **normalized** phase space $\{x, px, y, py\}$ such that

$\int_{-\infty}^{+\infty} \rho(x,y)dy$ = $\frac{1}{\sqrt{2\pi}} e^{-\left(\frac{x}{2}\right)^2}$ (Gaussian x-profile)

and

$\int_{-\infty}^{+\infty} \rho(x,y)dx$ = $\frac{1}{\sqrt{2\pi}} e^{-\left(\frac{y}{2}\right)^2}$ (Gaussian y-profile).

We will show in the following that $\rho(x,y)$ is not uniquely determined and we propose a possible parametrization of $\rho(x,y)$.

We can consider the action (J_x) and angle (θ_x) variables in the plane x-px (similar conclusions hold on the y-py plane). It is well known that if $\{x, px\}$ are normal distributed then $J_x = (x^2 + px^2)/2$ is distributed as

$$pdf(J_x) = \begin{cases} \exp(-J_x) & \text{if } J_x > 0 \\ 0 & \text{otherwise} \end{cases}$$

and

$$pdf(\theta_x) = \begin{cases} \frac{1}{2\pi} & \text{if } 0 < \theta_x < 2\pi \\ 0 & \text{otherwise.} \end{cases}$$

Case A

Assuming that the J_x and J_y are, in general, statistically dependent (we assume for the moment that θ_x and θ_y are independent), the marginal density function $pdf(J_y|J_x)$ should be a solution of these equations:

$\int_0^{+\infty} e^{-J_x} pdf(J_y|J_x) dJ_x = e^{-J_y}$

$\int_0^{+\infty} pdf(J_y|J_x) dJ_y = 1$ for all J_x

There are two possible solutions for $pdf(J_y|J_x)$

A1. $pdf(J_y|J_x) = e^{-J_y}$, that will yield fully xy independence,

A2. $pdf(J_y|J_x) = \delta(J_y - J_x)$, that will yield fully xy dependence.

Case B

Similar considerations hold for the phase.

$\int_0^{2\pi} \frac{1}{2\pi} pdf(\theta_x|\theta_y)d\theta_x = \frac{1}{2\pi}$ for $0 < \theta_y < 2\pi$

$\int_0^{2\pi} pdf(\theta_y|\theta_x)d\theta_y = 1$ for $0 < \theta_x < 2\pi$

There are two possible solutions for $pdf(\theta_x|\theta_y)$

B1. $pdf(\theta_x|\theta_y) = \frac{1}{2\pi}$ in the usual domain, that will yield fully xy independence,

B2. $pdf(\theta_x|\theta_y) = \delta(\theta_y - \theta_x)$ in the usual domain, that will yield fully xy dependence.

We will focus on the case A1/A2/B2.

In [25]:
```
# Case A1 (for simplicity I consider the extraction in x and y, not in actic
from matplotlib import pyplot as plt
import numpy as np
from scipy.stats import shapiro
from matplotlib.gridspec import GridSpec

N = 100000

fig = plt.figure(figsize=(4, 4))
gs = GridSpec(2, 2, width_ratios=[3, 1], height_ratios=[1, 3])  # Adjust rat
x_a1 = np.random.normal(0, 1, N)
px_a1 = np.random.normal(0, 1, N)
y_a1 = np.random.normal(0, 1, N)

# Plot the 2D distribution
ax0 = plt.subplot(gs[1, 0])
ax0.hist2d(x_a1, y_a1, bins=100, cmap='viridis')
ax0.set_xlabel('x [$\sigma_x$]')
ax0.set_ylabel('y [$\sigma_y$]')
ax0.set_xlim(-4,4)
ax0.set_ylim(-4,4)


# Plot the projection onto x-axis
ax1 = plt.subplot(gs[0, 0])
ax1.hist(x_a1, bins=300,  density=True,)
ax1.axis('off')

# Plot the projection onto y-axis
ax2 = plt.subplot(gs[1, 1])
ax2.hist(y_a1, bins=300, density=True, orientation='horizontal')
ax0.set_xlim(-4,4)

# An empty subplot to adjust the layout
ax3 = plt.subplot(gs[1, 1])
ax3.axis('off')
ax0.set_ylim(-4,4)
```

```
plt.tight_layout()
plt.show()
```

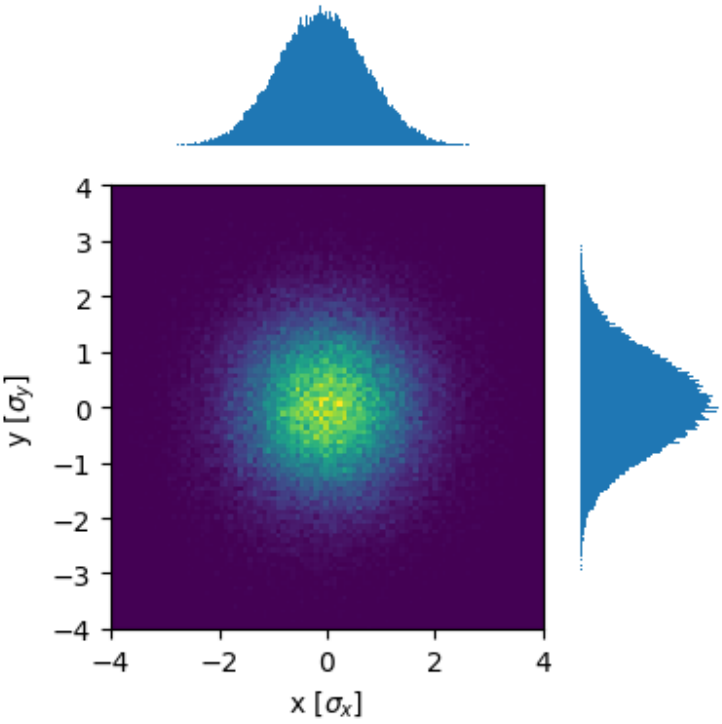

In [26]:

```
# Case A2

# the pdf of Jx for a Gaussian beam


def rho_J(J):
    return (np.exp(-J))

J = np.linspace(0,10,10000)

plt.figure()
plt.title('The pdf(J$_x$) of a Gaussian beam')
plt.plot(J, rho_J(J),'r')
plt.xlabel('J$_x$ [$\sigma_x^2$]')

plt.grid(True)

sigma_x = 1
# extract a N random numbers from the normal distribution
x_a2 = np.random.normal(0, sigma_x, N)
px_a2 = np.random.normal(0, sigma_x, N)
J_a2 = (x_a2**2 + px_a2**2)/2
plt.hist(J_a2, bins=500, density=True)
plt.xlim(0,8)

theta = np.random.uniform(0,2*np.pi, N)
y_a2 = np.sqrt(J_a2*2)*np.cos(theta)
py_a2 = np.sqrt(J_a2*2)*np.sin(theta)
```

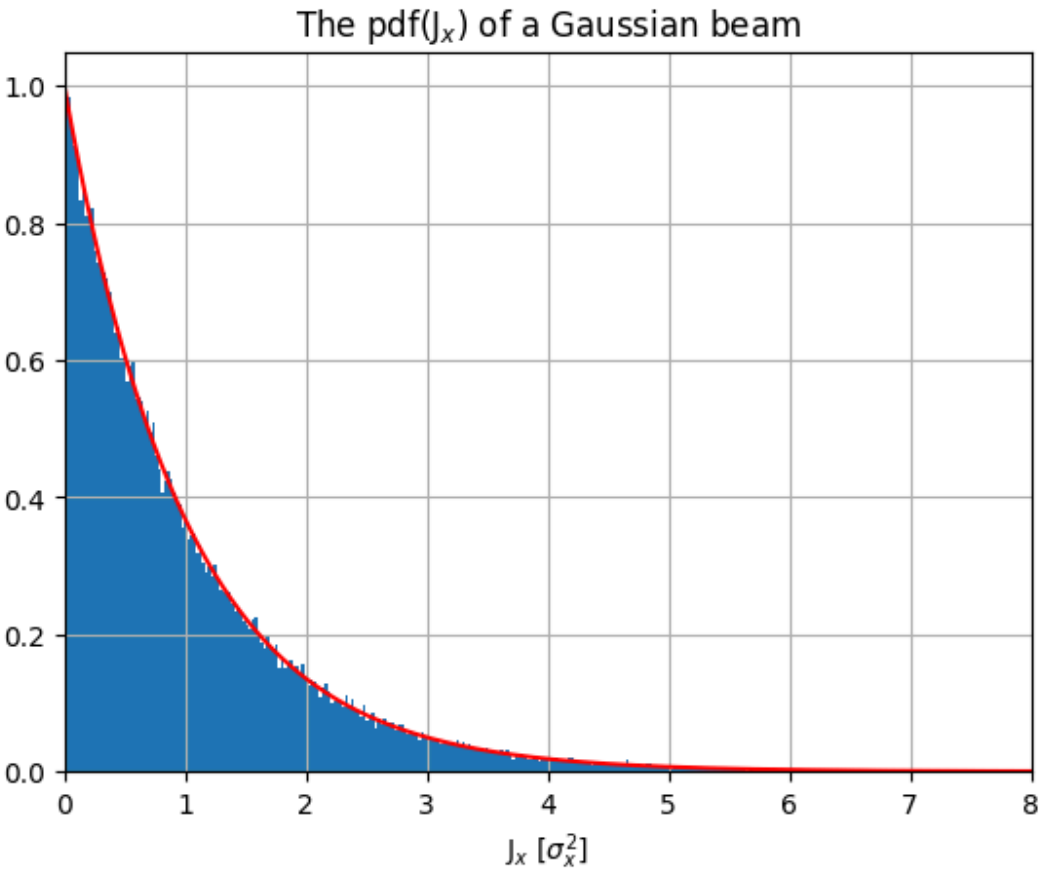

In [27]:
```
assert np.isclose(np.mean(J_a2),1, atol=0.05)
#perform Shapiro-Wilk test for normality
assert np.isclose(shapiro(x_a2).statistic, 1, atol=0.01)
assert np.isclose(shapiro(px_a2).statistic, 1, atol=0.01)
assert np.isclose(shapiro(y_a2).statistic, 1, atol=0.01)
assert np.isclose(shapiro(py_a2).statistic, 1, atol=0.01)
```

```
/Users/guidosterbini/miniforge3/lib/python3.10/site-packages/scipy/stats/_mo
restats.py:1882: UserWarning: p-value may not be accurate for N > 5000.
  warnings.warn("p-value may not be accurate for N > 5000.")
```

In [28]:
```
from matplotlib.gridspec import GridSpec

# Create a figure and a gridspec layout
fig = plt.figure(figsize=(4, 4))
gs = GridSpec(2, 2, width_ratios=[3, 1], height_ratios=[1, 3])  # Adjust rat

# Plot the 2D distribution
ax0 = plt.subplot(gs[1, 0])
ax0.hist2d(x_a2, y_a2, bins=100, cmap='viridis')
ax0.set_xlabel('x [$\sigma_x$]')
ax0.set_ylabel('y [$\sigma_y$]')
ax0.set_xlim(-4,4)
ax0.set_ylim(-4,4)


# Plot the projection onto x-axis
ax1 = plt.subplot(gs[0, 0])
```

```
ax1.hist(x_a2, bins=100,  density=True,)
ax1.axis('off')

# Plot the projection onto y-axis
ax2 = plt.subplot(gs[1, 1])
ax2.hist(y_a2, bins=100, density=True, orientation='horizontal')
ax0.set_ylim(-4,4)

# An empty subplot to adjust the layout
ax3 = plt.subplot(gs[1, 1])
ax3.axis('off')
ax0.set_xlim(-4,4)


plt.tight_layout()
plt.show()
```

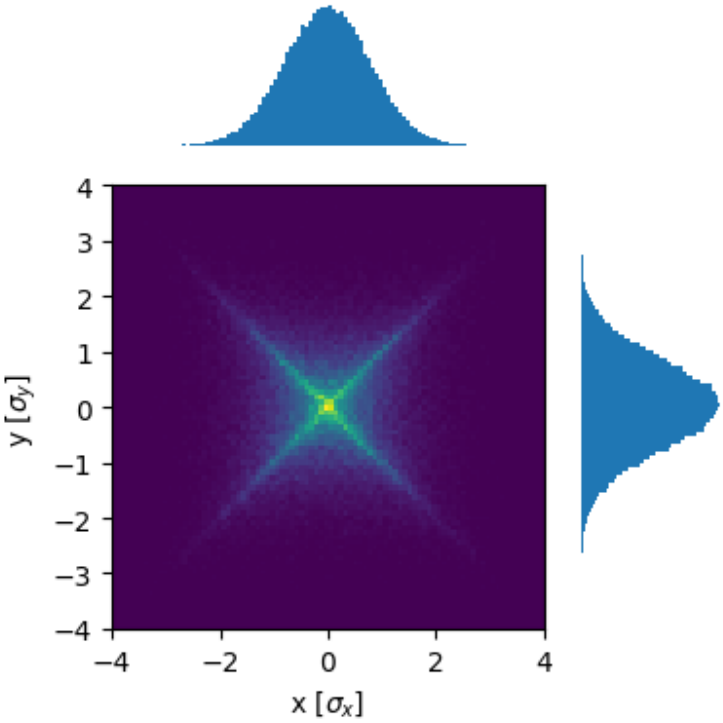

In [29]:

```
# Case B2
# from Jx and theta_y, we can get y and py

x_b2 = x_a1
px_b2 = px_a1
theta = np.arctan2(px_b2,x_b2)
# can you extract Jy from the distribution exp(-Jy) ?
Jy = np.random.exponential(1, N)
aux = np.linspace(0,10,10000)

y_b2 = np.sqrt(Jy*2)*np.cos(theta)
py_b2 = np.sqrt(Jy*2)*np.sin(theta)


fig = plt.figure(figsize=(4, 4))
```

```
gs = GridSpec(2, 2, width_ratios=[3, 1], height_ratios=[1, 3])  # Adjust rat

# Plot the 2D distribution
ax0 = plt.subplot(gs[1, 0])
ax0.hist2d(x_b2, y_b2, bins=100, cmap='viridis')
ax0.set_xlabel('x [$\sigma_x$]')
ax0.set_ylabel('y [$\sigma_y$]')
ax0.set_xlim(-4,4)
ax0.set_ylim(-4,4)


# Plot the projection onto x-axis
ax1 = plt.subplot(gs[0, 0])
ax1.hist(x_b2, bins=100,  density=True,)
ax1.axis('off')

# Plot the projection onto y-axis
ax2 = plt.subplot(gs[1, 1])
ax2.hist(y_b2, bins=100, density=True, orientation='horizontal')
ax0.set_ylim(-4,4)

# An empty subplot to adjust the layout
ax3 = plt.subplot(gs[1, 1])
ax3.axis('off')
ax0.set_xlim(-4,4)


plt.tight_layout()
plt.show()
```

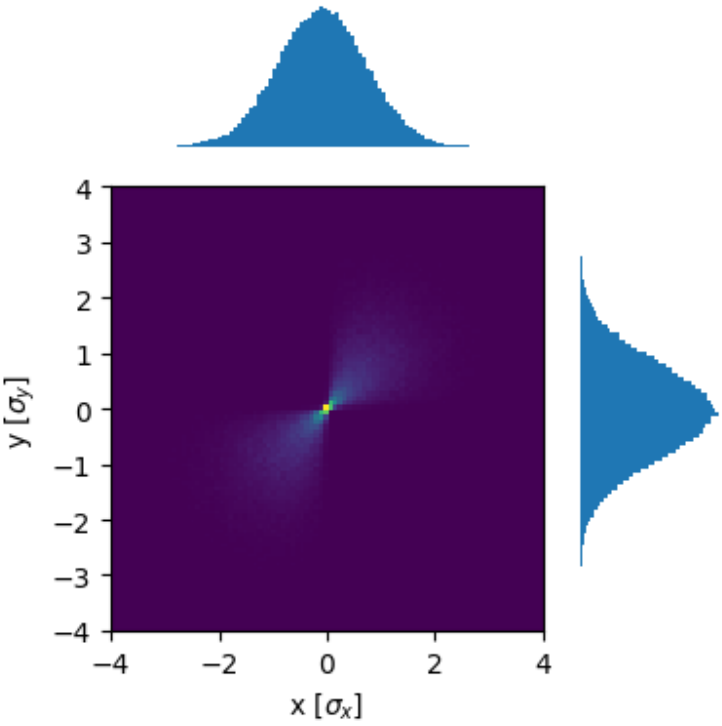

In [31]:
```
# combination of a1 and a2
y_b2 = np.sqrt(Jy*2)*np.cos(theta)
```

```
py_b2 = np.sqrt(Jy*2)*np.sin(theta)

# Create a figure and a gridspec layout
fig = plt.figure(figsize=(4, 4))
gs = GridSpec(2, 2, width_ratios=[3, 1], height_ratios=[1, 3])  # Adjust rat
#concatanate x and xx
new_x  = np.concatenate((x_a1, x_a2))
new_y = np.concatenate((y_a1, y_a2))

# Plot the 2D distribution
ax0 = plt.subplot(gs[1, 0])
ax0.hist2d(new_x, new_y, bins=100, cmap='viridis')
ax0.set_xlabel('x [$\sigma_x$]')
ax0.set_ylabel('y [$\sigma_y$]')


# Plot the projection onto x-axis
ax1 = plt.subplot(gs[0, 0])
ax1.hist(new_x, bins=100,  density=True,)
ax1.axis('off')

# Plot the projection onto y-axis
ax2 = plt.subplot(gs[1, 1])
ax2.hist(new_y, bins=100, density=True, orientation='horizontal')

# An empty subplot to adjust the layout
ax3 = plt.subplot(gs[1, 1])
ax3.axis('off')

plt.tight_layout()
plt.show()
```

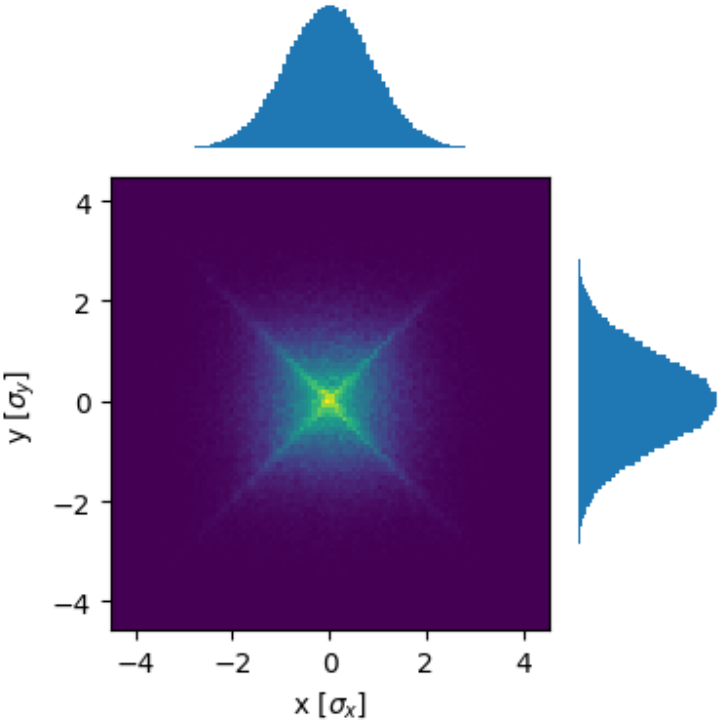

In [33]:
```
# compute KDE of the a2 distribution
from scipy.stats import gaussian_kde
k = gaussian_kde([x_a2,y_a2])
xi, yi = np.mgrid[-3:3:100j, -3:3:100j]
zi = k(np.vstack([xi.flatten(), yi.flatten()]))
plt.pcolormesh(xi, yi, zi.reshape(xi.shape), shading='gouraud', cmap=plt.cm.
plt.axis('equal')
plt.axis('off')
#
```

Out[33]:
```
(-3.0, 3.0, -3.0, 3.0)
```

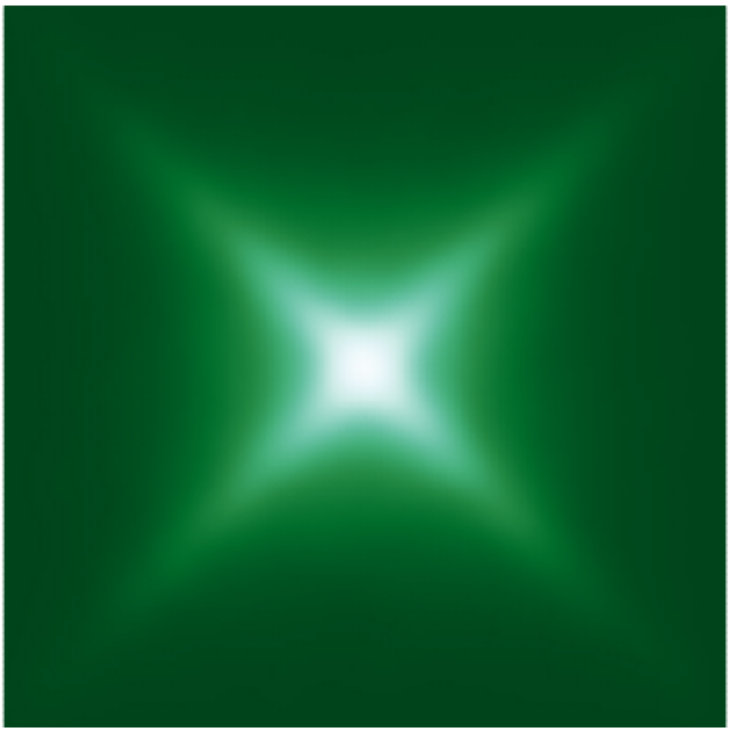

A photo of the BSRT x-y plane during 2023 (MD1 block)

https://codimd.web.cern.ch/uploads/upload_4b1c8e72127d2e2dc56a3bf34eee39d9.png

In [34]:
```
# H cut
r_cut = 2

r = np.sqrt(x_a2**2+px_a2**2)
# find r<r_cut
x_cut = x_a2[r<r_cut]
px_cut = px_a2[r<r_cut]
y_cut = y_a2[r<r_cut]
py_cut = py_a2[r<r_cut]
```

In [80]:
```
plt.plot(x_cut,px_cut,'.', alpha=0.01)
plt.axis('equal')
```

Out[80]: (-2.198072941716593,
2.1959424988666814,
-2.1990696942058476,
2.199443036550486)

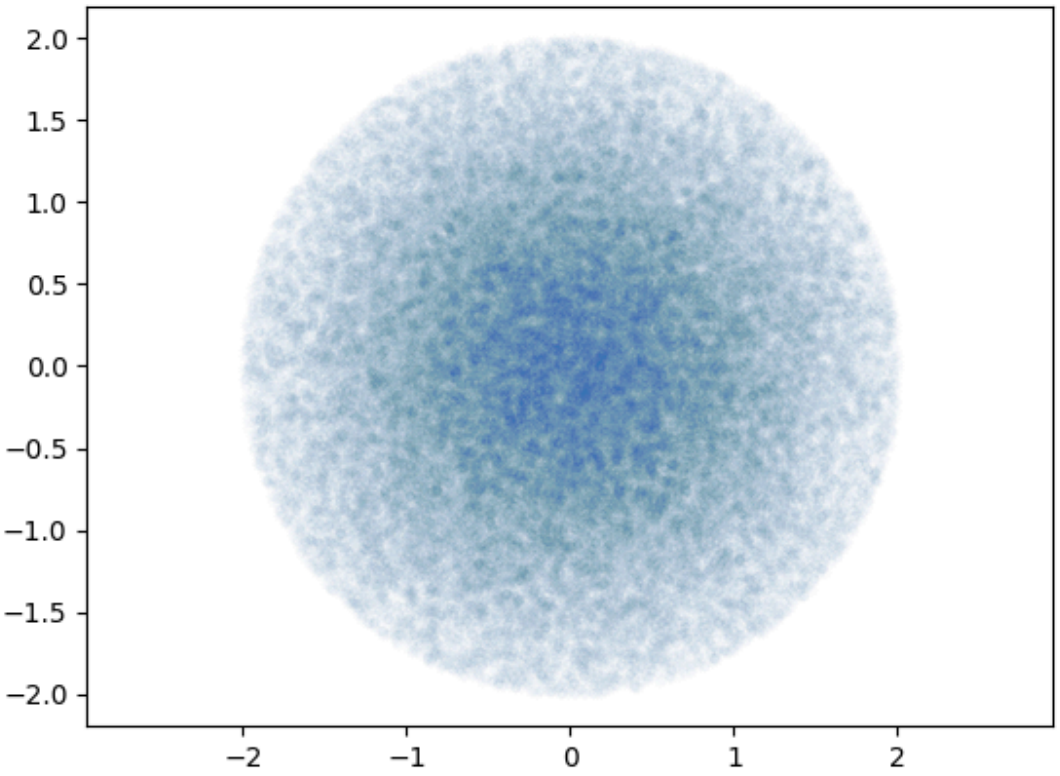

In [17]:
```
plt.plot(y_cut,py_cut,'.', alpha=0.01)
plt.axis('equal')
```

Out[17]: (-2.198064831420603,
2.192833002652979,
-2.1972373516190866,
2.1972431861675874)

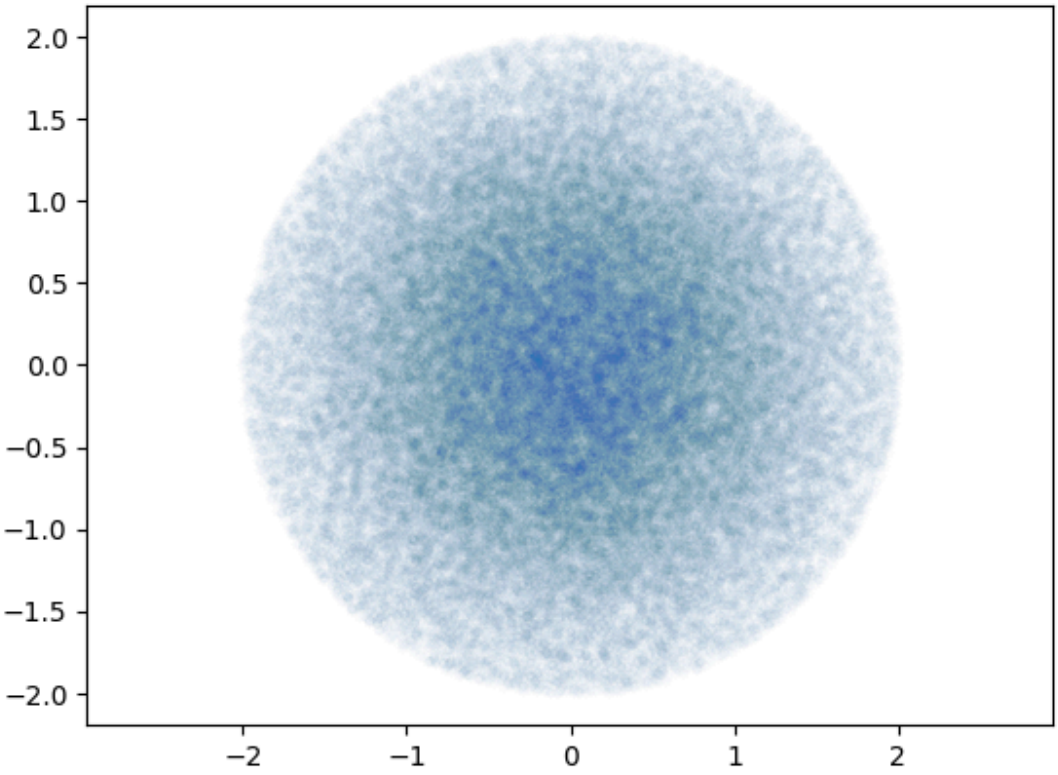

In [81]:
```
plt.hist(x, bins=100, density=True)
```

Bibliography

[1] A. Wolski, *Beam Dynamics in High Energy Particle Accelerators*, 2nd. Imperial College Press, 2014. DOI: 10.1142/p899.

[2] E. Forest, *Beam Dynamics*. Harwood Academic publishers, 1998.

[3] F. Landua, "The CERN accelerator complex layout in 2022. Complexe des accélérateurs du CERN en janvier 2022", 2022, General Photo. [Online]. Available: https://cds.cern.ch/record/2813716.

[4] W. Herr and E. Forest, *Non-linear dynamics in accelerators*, 2016.

[5] J. Liouville, "Sur la Théorie de la Variation des constantes arbitraires", *Journal de mathématiques pures et appliquées*, vol. 3, pp. 342–349, 1838, PDF available online. [Online]. Available: https://gallica.bnf.fr/ark:/12148/bpt6k433672j.

[6] E. Bravin, "Transverse emittance", Tech. Rep., 2020, 14 pages, contribution to the CAS - CERN Accelerator School: Beam Instrumentation, 2-15 June 2018, Tuusula, Finland. arXiv: 2005.05770. [Online]. Available: https://cds.cern.ch/record/2723977.

[7] H. Goldstein, C. Poole, J. Safko, and S. R. Addison, "Classical Mechanics, 3rd ed.", *American Journal of Physics*, vol. 70, no. 7, pp. 782–783, Jul. 2002, ISSN: 0002-9505. DOI: 10.1119/1.1484149. eprint: https://pubs.aip.org/aapt/ajp/article-pdf/70/7/782/7530963/782_1_online.pdf. [Online]. Available: https://doi.org/10.1119/1.1484149.

[8] A. N. Kolmogorov, "On conservation of conditionally periodic motions under small perturbations of the Hamiltonian", *Dokl. Akad. Nauk SSSR*, vol. 98, pp. 527–530, 1954.

[9] V. Arnold, "Small denominators, 1: Mappings of the circumference onto itself", *AMS Translations*, vol. 46, pp. 213–288, 1965, Russian original published in 1961.

[10] J. Moser, "On invariant curves of area-preserving mappings of an annulus", *Nachr. Akad. Wiss., Göttingen, Math. Phys. Kl.*, pp. 1–20, 1962.

[11] A. Franchi, "Studies and measurements of linear coupling and nonlinearities in hadron circular accelerators", Presented 2006, Ph.D. dissertation, Johann Wolfgang Goethe-Universität, 2006. [Online]. Available: https://d-nb.info/981264875/34.

[12] K. Schindl, "Space charge", 2006. DOI: 10.5170/CERN-2006-002.305. [Online]. Available: https://cds.cern.ch/record/941316.

[13] H. Bartosik, "Pushing the Space Charge Limit in the CERN LHC Injectors", in *Second Topical Workshop on Instabilities, Impedance and Collective Effects (TWIICE 2)*, Presented at the Second Topical Workshop on Instabilities, Impedance and Collective Effects (TWIICE 2), 10 February 2016, 2016.

[14] F. Asvesta, H. Bartosik, A. Huschauer, and Y. Papaphilippou, "Space charge driven resonances in the CERN PS", WEPTS047, 2019. DOI: 10.18429/JACoW-IPAC2019-WEPTS047. [Online]. Available: https://cds.cern.ch/record/2693531.

[15] G. Guignard, *The general theory of all sum and difference resonances in a three-dimensional magnetic field in a synchrotron* (CERN Yellow Reports: Monographs). Geneva: CERN, 1976. DOI: 10.5170/CERN-1976-006. [Online]. Available: https://cds.cern.ch/record/185921.

[16] G. Franchetti, O. Chorniy, I. Hofmann, *et al.*, "Experiment on space charge driven nonlinear resonance crossing in an ion synchrotron", *Phys. Rev. ST Accel. Beams*, vol. 13, p. 114 203, 11 Nov. 2010. DOI: 10.1103/PhysRevSTAB.13.114203. [Online]. Available: https://link.aps.org/doi/10.1103/PhysRevSTAB.13.114203.

[17] G. Franchetti, I. Hofmann, M. Giovannozzi, M. Martini, and E. Metral, "Space charge and octupole driven resonance trapping observed at the CERN Proton Synchrotron", *Phys. Rev. ST Accel. Beams*, vol. 6, no. 12, Dec. 2003. [Online]. Available: doi:10.1103/PhysRevSTAB.6.124201.

[18] H. Poincaré, *Les Méthodes Nouvelles de la Mécanique Céleste*. Paris: Gauthier Villars, 1899, vol. 1–3.

[19] H. Bartosik, G. Franchetti, and F. Schmidt, "Observation of fixed lines induced by a nonlinear resonance in the cern super proton synchrotron", *Nature Physics*, vol. 20, pp. 928–933, 2024. DOI: 10.1038/s41567-023-02338-3. [Online]. Available: https://doi.org/10.1038/s41567-023-02338-3.

[20] G. Franchetti and F. Schmidt, "Extending the Nonlinear-Beam-Dynamics Concept of 1D Fixed Points to 2D Fixed Lines.", *Physical review letters*, vol. 114 23, p. 234 801, 2015. [Online]. Available: https://api.semanticscholar.org/CorpusID:34913442.

[21] G. Franchetti, S. Gilardoni, A. Huschauer, F. Schmidt, and R. Wasef, "Space charge effects on the third order coupled resonance", *Phys. Rev. Accel. Beams*, vol. 20, no. 8, p. 081 006, 2017. DOI: 10.1103/PhysRevAccelBeams.20.081006.

[22] W. Herr and B. Muratori, "Concept of luminosity", 2006. DOI: 10.5170/CERN-2006-002.361. [Online]. Available: https://cds.cern.ch/record/941318.

[23] F. Frenet, "Sur les courbes à double courbure", Abstract in Journal de Mathématiques Pures et Appliquées 17, 1852, http://www.sci.brooklyn.cuny.edu/~mate/misc/frenet_serret.pdf, Thèse, Toulouse, 1847.

[24] J. A. Serret, "Sur quelques formules relatives à la théorie des courbes à double courbure", *Journal de Mathématiques Pures et Appliquées*, vol. 16, 1851, http://www.sci.brooklyn.cuny.edu/~mate/misc/frenet_serret.pdf.

[25] CMS collaboration, "Luminosity measurement in proton-proton collisions at 13.6 TeV in 2022 at CMS", CERN, Geneva, Tech. Rep., 2024. [Online]. Available: https://cds.cern.ch/record/2890833.

[26] CMS collaboration, "First measurement of the top quark pair production cross section in proton-proton collisions at $\sqrt{s}$ = 13.6 TeV", *JHEP*, vol. 08, p. 204, 2023. DOI: 10.1007/JHEP08(2023)204. arXiv: 2303.10680 [hep-ex].

[27] CMS collaboration, "Measurement of the mass dependence of the transverse momentum of lepton pairs in Drell–Yan production in proton-proton collisions at $\sqrt{s}$ = 13 TeV", *Eur. Phys. J. C*, vol. 83, p. 628, 2023. DOI: 10.1140/epjc/s10052-023-11631-7. arXiv: 2205.04897 [hep-ex].

[28] CMS collaboration, "Measurement of the inclusive and differential tt cross sections in the dilepton channel and effective field theory interpretation in proton-proton collisions at $\sqrt{s}$ = 13 TeV", *JHEP*, vol. 05, p. 091, 2022. DOI: 10.1007/JHEP05(2022)091. arXiv: 2201.07301 [hep-ex].

[29] A. M. Sirunyan, A. Tumasyan, W. Adam, *et al.*, "Precision luminosity measurement in proton–proton collisions at 13 TeV in 2015 and 2016 at CMS", *Eur. Phys. J. C*, vol. 81, p. 800, 2021. DOI: 10.1140/epjc/s10052-021-09538-2. [Online]. Available: https://doi.org/10.1140/epjc/s10052-021-09538-2.

[30] S. van der Meer, "Calibration of the effective beam height in the ISR", CERN, ISR Report CERN-ISR-PO-68-31, 1968.

[31] C. Rubbia, "Measurement of the luminosity of pp collider with a (generalized) Van der Meer method", CERN, Technical Report CERN-pp-Note-38, 1977.

[32] CMS collaboration, "Measurement of the offline integrated luminosity for the CMS proton-proton collision dataset recorded in 2023", *CMS performance note*, 2024. [Online]. Available: https://cds.cern.ch/record/2904808.

[33] CMS collaboration, "XY-factorization correction for luminosity calibration using off-axis scans for 2022 pp data at 13.6 TeV", *CMS Performance Note*, 2023. [Online]. Available: https://cds.cern.ch/record/2887411.

[34] ATLAS collaboration, "Preliminary analysis of the luminosity calibration for the ATLAS 13.6 TeV data recorded in 2023", CERN, Geneva, Tech. Rep., 2024, All figures including auxiliary figures are available at https://atlas.web.cern.ch/Atlas/GROUPS/PHYSICS/PUBNOTES/ATL-DAPR-PUB-2024-001. [Online]. Available: https://cds.cern.ch/record/2900949.

[35] ATLAS collaboration, "Preliminary analysis of the luminosity calibration of the ATLAS 13.6 TeV data recorded in 2022", CERN, Geneva, Tech. Rep., 2023, All figures including auxiliary figures are available at https://atlas.web.cern.ch/Atlas/GROUPS/PHYSICS/PUBNOTES/ATL-DAPR-PUB-2023-001. [Online]. Available: https://cds.cern.ch/record/2853525.

[36] W. R. Hamilton, *On a General Method of Expressing the Paths of Light, & of the Planets, by the Coefficients of a Characteristic Function*. Printed by P.D. Hardy, 1833, OCLC 68159539.

[37] E. Noether, “Invariante Variationsprobleme”, *Nachrichten von der Gesellschaft der Wissenschaften zu Göttingen, Mathematisch-Physikalische Klasse*, pp. 235–257, 1918, Translated as "Invariant Variation Problems" in Transport Theory and Statistical Physics, 1 (3): 186-207 (1971). [Online]. Available: https://doi.org/10.1007/978-3-662-02781-3_7.

[38] N. H. Abel, *Oeuvres complètes*. 1881.

[39] R. Bracewell, *The Fourier transform and its applications, 3rd ed.* 1999.

[40] Y. Batygin, “Particle-in-cell code beampath for beam dynamics simulations in linear accelerators and beamlines”, *Nuclear Instruments and Methods in Physics Research Section A: Accelerators, Spectrometers, Detectors and Associated Equipment*, vol. 539, pp. 455–489, Mar. 2005. [Online]. Available: doi:10.1016/j.nima.2004.10.029.

[41] F. Asvesta, “Characterization of transverse profiles along the LHC injector chain at CERN”, in *Proc. 14th International Particle Accelerator Conference*, (Venezia), ser. IPAC’23 - 14th International Particle Accelerator Conference, JACoW Publishing, Geneva, Switzerland, May 2023, pp. 3443–3446, ISBN: 978-3-95450-231-8. DOI: doi:10.18429/jacow-ipac2023-wepl158. [Online]. Available: https://indico.jacow.org/event/41/contributions/2319.

[42] S. Papadopoulou, F. Antoniou, T. Argyropoulos, M. Fitterer, M. Hostettler, and Y. Papaphilippou, “Modelling and measurements of bunch profiles at the LHC ”, *Journal of Physics: Conference Series*, vol. 874, no. 1, p. 012 008, Jul. 2017. DOI: 10.1088/1742-6596/874/1/012008. [Online]. Available: https://dx.doi.org/10.1088/1742-6596/874/1/012008.

[43] E. M. F. Curado and C. Tsallis, “Generalized statistical mechanics: connection with thermodynamics”, *Journal of Physics A: Mathematical and General*, vol. 24, no. 2, p. L69, Jan. 1991. [Online]. Available: doi:10.1088/0305-4470/24/2/004.

[44] C. Tsallis, “Possible generalization of Boltzmann–Gibbs statistics.”, *J Stat Phys 52:479–487;*, 1988.

[45] Wolfram Research, Inc., *Mathematica, version 13.2*, Champaign, IL, 2022. [Online]. Available: https://www.wolfram.com/mathematica.

[46] G. Box and M. Muller, “A Note on the Generation of Random Normal Deviates”, *The Annals of Mathematical Statistics*, 1958. DOI: doi:10.1214/aoms/1177706645.

[47] T. Mitsuhashi, E. Bravin, O. R. Jones, F. Roncarolo, H. Schmickler, and G. Trad, “Design of Coronagraph for the Observation of Beam Halo at LHC”, TUCLA03, 2016. DOI: 10.18429/JACoW-IBIC2015-TUCLA03. [Online]. Available: https://cds.cern.ch/record/2263473.

[48] M. Fitterer, G. Stancari, S. Papadopoulou, Y. Papaphilippou, and S. Redaelli, “Analysis of BSRT Profiles in the LHC at Injection”, Dec. 2017. DOI: 10.2172/1438589. [Online]. Available: https://www.osti.gov/biblio/1438589.

[49] A. Gorzawski, R. B. Appleby, M. Giovannozzi, *et al.*, "Probing LHC halo dynamics using collimator loss rates at 6.5 TeV", *Phys. Rev. Accel. Beams*, vol. 23, p. 044 802, 4 Apr. 2020. DOI: 10.1103/PhysRevAccelBeams.23.044802. [Online]. Available: https://link.aps.org/doi/10.1103/PhysRevAccelBeams.23.044802.

[50] C. E. Montanari, A. Bazzani, and M. Giovannozzi, *Probing the diffusive behaviour of beam-halo dynamics in circular accelerators*, 2022. arXiv: 2202.10050 [physics.acc-ph]. [Online]. Available: https://arxiv.org/abs/2202.10050.

[51] E. Courant and H. Snyder, "Theory of the alternating gradient synchrotron", *Annals of Physics*, vol. 3, no. 1, pp. 1–48, 1958. [Online]. Available: doi:10.1016/0003-4916(58)90012-5.

[52] G. Franchetti and I. Hofmann, "Particle trapping by nonlinear resonances and space charge", *Nuclear Instruments and Methods in Physics Research Section A: Accelerators, Spectrometers, Detectors and Associated Equipment*, vol. 561, no. 2, pp. 195–202, 2006, Proceedings of the Workshop on High Intensity Beam Dynamics, ISSN: 0168-9002. [Online]. Available: doi:10.1016/j.nima.2006.01.031.

[53] F. Asvesta, H. Barosik, D. Cotte, *et al.*, "Resonance Compensation for High Intensity and High Brightness Beams in the CERN PSB", in *Proc. ICFA ABDW on High-Intensity and High-Brightness Hadron Beams (HB'21)*, ser. ICFA ABDW on High-Intensity and High-Brightness Hadron Beams, paper MOP06, Batavia, IL, USA: JACoW Publishing, Apr. 2022, pp. 40–45, ISBN: 978-3-95450-225-7. [Online]. Available: doi:10.18429/JACoW-HB2021-MOP06.

[54] F. Asvesta and H. Bartosik, "Resonance Driving Terms From Space Charge Potential", 2019. [Online]. Available: http://cds.cern.ch/record/2696190.

[55] S. Hancock, M. Lindroos, and S. Koscielniak, "Longitudinal phase space tomography with space charge", *Phys. Rev. ST Accel. Beams*, vol. 3, p. 124 202, 12 Dec. 2000. DOI: 10.1103/PhysRevSTAB.3.124202. [Online]. Available: https://link.aps.org/doi/10.1103/PhysRevSTAB.3.124202.

[56] G. Iadarola *et al.*, "Xsuite: An Integrated Beam Physics Simulation Framework", *JACoW*, vol. HB2023, TUA2I1, 2024. DOI: 10.18429/JACoW-HB2023-TUA2I1. arXiv: 2310.00317 [physics.acc-ph].

[57] F. Asvesta, *Psb_fma_flat_bottom*, https://github.com/fasvesta/psb_fma_flat_bottom, GitHub repository, 2024.

[58] S. Guiducci, "Chromaticity; rev. version", 1994. DOI: 10.5170/CERN-1994-001.191. [Online]. Available: https://cds.cern.ch/record/398300.

[59] J. Laskar, "The chaotic motion of the solar system: a numerical estimate of the size of the chaotic zones", *Icarus*, vol. 88, no. 2, pp. 266–291, 1990, ISSN: 0019-1035. DOI: https://doi.org/10.1016/0019-1035(90)90084-M. [Online]. Available: https://www.sciencedirect.com/science/article/pii/001910359090084M.

[60] S. Kostoglou, N. Karastathis, Y. Papaphilippou, D. Pellegrini, and P. Zisopoulos, "Development of Computational Tools for Noise Studies in the LHC", in *Proc. of International Particle Accelerator Conference (IPAC'17), Copenhagen, Denmark, 14-19 May, 2017*, ser. International Particle Accelerator Conference, Geneva, Switzerland: JACoW, May 2017, pp. 3807–3810, ISBN: 978-3-95450-182-3. DOI: https://doi.org/10.18429/JACoW-IPAC2017-THPAB044. [Online]. Available: http://jacow.org/ipac2017/papers/thpab044.pdf.

[61] A. Schoch, "Theory of linear and non-linear perturbations of betatron oscillations in alternating gradient synchrotrons", CERN, Proton Synchrotron Division, Tech. Rep. CERN 57-21, Feb. 1958.

[62] T. Prebibaj, *PSB xSuite Examples*, 2024. [Online]. Available: https://gitlab.cern.ch/tprebiba/psb-xsuite-examples.

[63] D. Quatraro, G. Rumolo, A. Blas, M. Chanel, A. Findlay, and B. Mikulec, "Coherent tune shift and instabilities measurements at the CERN Proton Synchrotron Booster", 2010. [Online]. Available: https://cds.cern.ch/record/1208696.

[64] B. W. S. L. Montague, *Fourth-order coupling resonance excited by space-charge forces in a synchrotron* (CERN Yellow Reports: Monographs). Geneva: CERN, 1968. DOI: 10.5170/CERN-1968-038. [Online]. Available: https://cds.cern.ch/record/275769.

[65] H. Hotchi, "Effects of the Montague resonance on the formation of the beam distribution during multiturn injection painting in a high-intensity proton ring", *Phys. Rev. Accel. Beams*, vol. 23, p. 050 401, 5 May 2020. DOI: 10.1103/PhysRevAccelBeams.23.050401. [Online]. Available: https://link.aps.org/doi/10.1103/PhysRevAccelBeams.23.050401.

[66] H. Bartosik and G. Rumolo, "Production of single Gaussian bunches for Van der Meer scans in the LHC injector chain", *CERN Note*, 2013. [Online]. Available: https://cds.cern.ch/record/1590405.

[67] A. Edwards and M. J. Syphers, "Emittance preservation", in *An Introduction to the Physics of High Energy Accelerators*. John Wiley Sons, Ltd, 1993, ch. 7, pp. 221–268, ISBN: 9783527617272. DOI: https://doi.org/10.1002/9783527617272.ch7. eprint: https://onlinelibrary.wiley.com/doi/pdf/10.1002/9783527617272.ch7. [Online]. Available: https://onlinelibrary.wiley.com/doi/abs/10.1002/9783527617272.ch7.

[68] D. Möhl, "Sources of emittance growth", 2006. DOI: 10.5170/CERN-2006-012.45. [Online]. Available: https://cds.cern.ch/record/1005037.

[69] S. Kostoglou, G. Sterbini, H. Bartosik, and I. Efthymiopoulos, "Profile Measurements & Tails: From the SPS to the LHC", Presented at LBOC meeting 167, 4th June 2024. https://indico.cern.ch/event/1420698/, Jun. 2024.

[70] N. Karastathis, F. Antoniou, I. Efthymiopoulos, *et al.*, "Monitoring and Modeling of the LHC Luminosity Evolution in 2017", *J. Phys.: Conf. Ser.*, vol. 1067, no. 2, MOPMF052, 2018. DOI: 10.18429/JACoW-IPAC2018-MOPMF052. [Online]. Available: https://cds.cern.ch/record/2648702.

[71] S. Kostoglou and F. Asvesta, *2024 Experience with BCMS Beam*, Presentation at Injectors Performance Panel, CERN, Presented on 2 August 2024, Aug. 2024. [Online]. Available: https://indico.cern.ch/event/1441128/#sc-30-14-lhc-10-10.

ELLEANOR LAMB

10 Chemin de Noyères, 1217 Meyrin, Geneva CH
+41791997851, elleanor.lamb@epfl.ch, elamb@cern.ch

EDUCATION

CERN/EPFL - Ph.D. in Accelerator Physics (Switzerland) *2021 -September 2024*
Ph.D student working on non-linear dynamics for proton beams in the LHC and CERN injector complex under Dr. G. Sterbini.

Imperial College London - Integrated Master in Physics, MSci (UK) *2016 - 2020*
Master's thesis: Numerical ocean modelling. Graduated with Upper Second-Class Honours.

Ripon Grammar School (UK) *2009 - 2016*
A-level - Maths [A*], Further Maths [A*], Physics [A*]. AS Level - Economics [A].

EXPERIENCE

Doctoral Student in Accelerator Physics, EPFL / CERN BE-ABP-INC *2021-Present*

- Simulation with numerical tracking codes, experimental campaigns and analytical work on correlations induced into particle bunches via non-linear mechanisms. Analytical work on machine performance related to beam distributions.
- Invited oral presentations at conferences and conference proceedings, plan to publish results in a journal.
- **Courses**: USPAS grade - outstanding, CAS accelerator schools, EPFL advanced concepts in accelerator physics grade - 6/6.

Carbon Cycle Research, Imperial College London *2018 and 2020*

- 2020 - Master thesis research on ocean models of C-13 distribution, running simulations and analysis of large data sets resulting in a journal publication.
- 2018 - Summer research project using MATLAB to analyse ocean circulation models.

Software Engineering Internship, J.P. Morgan Geneva *June 2019–August 2019*

- Team project using Python to develop 'full stack' applications.
- Weekly presentations and collaboration with stakeholders to produce desired applications.

SKILLS

Computer languages	Python, MATLAB, Assembly, MAD-X.
Soft skills / interests	Fluent English, B2/C1 French. Love to windsurf and cycle.

PUBLICATIONS AND TALKS

- **E. Lamb**, G. Sterbini and H. Bartosik, "Luminosity effects due to dependent heavy-tailed beams", in Proc. IPAC'24, Nashville, TN, May 2024, pp. 55-58. doi:10.18429/JACoW-IPAC2024-MOPC09
- **E. Lamb** et al., "Measurements of beam correlations induced via coupled resonance crossing in the CERN PSB", in Proc. IPAC'24, Nashville, TN, May 2024, pp. 1006-1009. doi:10.18429/JACoW-IPAC2024-TUPC07
- M. Rufolo et al., "Numerical methods for emittance computation from luminosity", in Proc. IPAC'24, Nashville, TN, May 2024, pp. 95-98. doi:10.18429/JACoW-IPAC2024-MOPC19

- (Talk) **E. Lamb** et al., "Transverse beam quality along the chain for LHC beams", Joint Accelerator Performance Workshop 2023, Montreux, Switzerland. https://indico.cern.ch/event/1337597/contributions/5634046/
- **E.R. Lamb**, F. Asvesta, H. Bartosik, and G. Sterbini, "Measurement of Transverse Statistical Dependence for Non-Gaussian Beam Distributions via Resonances in the CERN PSB", in Proc. 68th Adv. Beam Dyn. Workshop High-Intensity High-Brightness Hadron Beams (HB'23), Geneva, Switzerland, Oct. 2023, pp. 231-235. doi:10.18429/JACoW-HB2023-WEA2C2
- H. Graven, **E. Lamb**, D. Blake, and S. Khatiwala, (2021). Future changes in δ13C of dissolved inorganic carbon in the ocean. Earth's Future, https://doi.org/10.1029/2021EF002173